DEVELOPMENT AND EXPERIMENTAL TESTING OF PRESS-BRAKE-FORMED STEEL TUB GIRDERS FOR SHORT SPAN BRIDGE APPLICATIONS

Karl E. Barth, Ph.D.
Gregory K. Michaelson, Ph.D.
Madison Lynn Morgan

VOLUME IX: THE IMPACT OF SKEW ON THE ULTIMATE CAPACITY OF PRESS-BRAKE-FORMED TUB GIRDERS

Submitted to the AISI Steel Market
Development Institute Short Span
Steel Bridge Alliance

ABSTRACT

THE IMPACT OF SKEW ON THE ULTIMATE CAPACITY OF PRESS-BRAKE-FORMED TUB GIRDERS

The development of press-brake-formed tub girders (PBFTGs) has offered innovative solutions for short-span steel bridge applications and helps meet the demand for rapid infrastructure replacement solutions. The Short Span Steel Bridge Alliance (SSSBA) comprises bridge and buried soil structure industry leaders who aim to provide essential educational information to bridge and highway professionals on the design and construction of short-span steel bridge installations (SSSBA, 2020). The American Association of State and Highway Transportation Officials (AASHTO) provides design standards, specifications, and guidance for the analysis and construction of PBFTGs. Currently, the AASHTO Load Resistance and Factor Design Bridge Design Specifications (AASHTO LRFD BDS) classifies PBFTGs as non-compact sections under any skew angle, which limits the flexural capacity to the yield moment (M_y). This specification greatly limits the applicability of PBFTGs in bridge design, as the plastic moment capacity (M_p) cannot be achieved when designing a PBFTG bridge using the current AASHTO LRFD BDS.

The scope of this research project was to better understand and characterize the flexural behavior of PBFTGs under low-skew angles to expand the applicability of the PBFTG system. This project was performed in four stages. Experimental pseudo-static flexural testing was first performed on two composite 15-degree PBFTGs to collect data and observe the ultimate capacity of each system. A rational methodology based on previous PBFTG research at West Virginia University (WVU) was used to build analytical three-dimensional finite element analysis (FEA) models to benchmark against the experimental test data. The employed FEA techniques were verified by comparing the model's data to the collected experimental data. A sensitivity study was developed by modeling a matrix of 3,509 PBFTG bridges using the three-dimensional finite element modeling software Abaqus. These girders were modeled with varied parameters before being analyzed for their ultimate flexural capacities. From this analysis result, statistical models were developed to verify further that skewness does not impact the ultimate flexural capacity of PBFTGs up to 20 degrees.

Results of this research project show that low-skewed PBFTGs perform with an ultimate flexural capacity exceeding M_y. This study demonstrates that PBFTGs have a more comprehensive range of applicability and can be a strong competitor in the bridge market if the AASHTO LRFD BDS adopts the recommendation to classify PBFTGs with skews up to 20 degrees as compact sections. Integrating this concept will broaden the applicability of PBFTGs and benefit the design process of shallow steel tub girder bridges

TABLE OF CONTENTS

LIST OF TABLES

LIST OF FIGURES

CHAPTER 1: INTRODUCTION

1.1 Background and Overview

The Short Span Steel Bridge Alliance (SSSBA) is a group of bridge and buried soil steel structure industry leaders who provide educational information on the design and construction of short-span steel bridges in installations up to 140 feet in length. The SSSBA technical working group developed a modular shallow press-brake-formed tub girder (PBFTG) as an innovative solution to meet the demand for rapid infrastructure replacements for short-span-steel bridge applications. PBFTGs are fabricated from a cold-bent structural steel plate and are bent into a shallow, trapezoidal box before shear studs are welded to the flanges, as seen in Figure 1.1. These tub girders (closed-box-section members) can be formed from weathering or galvanized steel. A concrete deck or other deck options, such as steel sandwich plate systems, may be placed on the girder on-site or cast at the fabrication site before the composite modular unit is shipped by truck to the bridge site, offering accelerated construction solutions (SSSBA, 2022).

Figure 1.1: PBFTG after Cold Bending (Valmont, 2023)

Note. The figure was provided by the manufacturer. Reprinted with permission.

PBFTGs have upheld economic and structural competitiveness through extensive research, including laboratory experiments, field demonstrations, and analytical modeling. The American

Association of State Highway and Transportation Officials (AASHTO) Innovation Initiative (AII) works "to identify and champion the implementation or deployment of a select few proven technologies, products, or processes" likely to yield significant economic or qualitative benefits (*AASHTO - AASHTO Innovation Initiative,* n.d.). AII selected the PBFTG bridge system as a 2021 Focus Technology and has invested considerable time and resources to encourage the system's adoption. The PBFTG bridge system was recognized for its scheduling and economic efficiency as a technology that could assist with the growing issue of rapid deterioration rates in bridges across the United States that outpace available funding for replacements. While this bridge system has proven its efficiency and competitiveness, its applicability is greatly limited by the AASHTO Load Resistance and Factor Design Bridge Design Specifications (AASHTO LRFD BDS), which implement many specifications that govern design specifications for capacity and analysis and restrict the efficiency and applicability of this modular bridge system.

1.2 PROJECT SCOPE AND OBJECTIVES

The scope of this research project was to better understand and characterize the flexural behavior of PBFTGs under low-skew angles to expand the applicability of the PBFTG system. AASHTO LRFD BDS limits the flexural capacity of PBFTGs to the yield moment (M_y) under any skew angle during design and analysis. This project aims to determine whether the ultimate capacity is reduced for PBFTGs with skew angles up to 20 degrees. These objectives will be achieved through the following:

- Examining literature relating to PBFTGs and the effect of skew angles on compactness classification and flexural capacity of sections.
- Performing destructive flexural testing and analytical modeling to assess the behavior and capacity of representative skewed reinforced concrete decks.
- Performing destructive flexural testing of representative specimens.
- Developing analytical techniques and verifying the finite element models against the experimental results.
- Developing analytical tools to assess the behavior and capacity of a matrix of PBFTGs with varying dimensions and properties.

- Conducting behavioral and parametric studies to assess the effect of skew on the computation of ultimate capacity for PBFTGs.
- Comparison to current AASHTO specifications to determine their applicability to low-skewed PBFTGs in determining compact classification.

1.3 REPORT ORGANIZATION

An overview of the organization of this report is as follows:

- Chapter 2:
  - This chapter presents a thorough literature review of previous research on cold-bent PBFTGs at West Virginia University (WVU). It also provides a brief background on the implementations of various other tub girder fabrication systems, including welded plate tub girders.
- Chapter 3:
  - This chapter provides an in-depth review of the current provisions for box-section flexural members detailed in the AASHTO LRFD BDS.
- Chapter 4:
  - This chapter summarizes previous laboratory and analytical research on skewed reinforced concrete bridge deck slabs to determine flexural capacity. This chapter focuses explicitly on test specimen descriptions, specimen assembly designs and assembly, testing program, testing instrumentation, and the analyzed results.
- Chapter 5:
  - This chapter summarizes the experimental research techniques and methodology used for the study. Two 15° skewed press-brake-formed tub girder specimens underwent destructive flexural testing after a composite concrete deck was cast on top of each girder. This chapter also describes the specimen details, testing program, testing instrumentation, and a discussion of the test results and data.

- Chapter 6:
    - This chapter describes the three-dimensional finite element modeling techniques employed, as well as adaptations to the model from previous research studies.
- Chapter 7:
    - This chapter describes the sensitivity study of a matrix of three-dimensional, finite element modeled composite tub girders with varied skew angles and parameters. Specifically, it focuses on analysis to determine each parameter's impact on the matrix's flexural capacity of all girders. It also discusses the research results in comparison to current AASHTO provisions to determine the compactness classification of skewed PBFTGs.
- Chapter 8:
    - This chapter offers a summary of the project, concludes the research results and key findings, and specifies recommendations for design expansion and future research efforts.

CHAPTER 2: LITERATURE REVIEW

2.1 INTRODUCTION

This chapter synthesizes prior research on PBFTGs and examines the literature on various cold-bent tub girders. The chapter delves into the research practicum conducted by West Virginia University and Marshall University, covering the design and implementation of PBFTGs. Commencing in 2011, the research at WVU, in collaboration with the SSSBA, aimed to establish PBFTGs as a cost-effective steel alternative for short-span bridges. Through experimental and analytical endeavors, the development and long-term performance behaviors of PBFTGs are discussed while also considering alternative tub girder bridge solutions, such as bolted and welded fabrication systems.

2.2 DEVELOPMENT AND EVALUATION OF PRESS-BRAKE-FORMED TUB GIRDERS

For decades, researchers have delved into the field of prefabricated steel tub girder systems, though their recent surge in adoption, considerably after being named an AII Focus Technology in 2021, particularly notable within the short-span bridge market. With accelerated bridge construction (ABC) methodologies gaining traction in design and erection practices, press-brake-formed tub girders have emerged as cost-effective and competitive solutions, particularly viable for spans up to 85 feet. Across numerous studies and initiatives, various researchers and organizations have studied the efficiency of systems incorporating different types of cold-bent steel tub girders.

2.2.1 Development and Feasibility Assessment of Shallow Press-Brake-Formed Steel Tub Girders for Short-Span Bridge Applications (Michaelson, 2014)

Michaelson's (2014) innovative research conducted a modular design concept for PBFTGs in collaboration with the SSSBA, offering a novel alternative to traditional concrete box beams for short-span bridges, accommodating spans up to 90 feet. This innovative approach entails cold-bending a standard mill plate to fashion trapezoidal box girders. Girders can utilize uncoated weathering or galvanized steel of various plate widths and thicknesses. Post-press-brake forming,

shear studs are welded onto the top flanges followed by the casting of a reinforced concrete deck onto the girder within the fabrication shop or in cast in place on the job site. Once cured, the composite modular unit is ready for transportation to the bridge construction site, expediting assembly and minimizing traffic disruptions. Figure 2.1 visually depicts a modular PBFTGs with a concrete deck, highlighting the effectiveness of this composite tub girder system in expediting construction timelines.

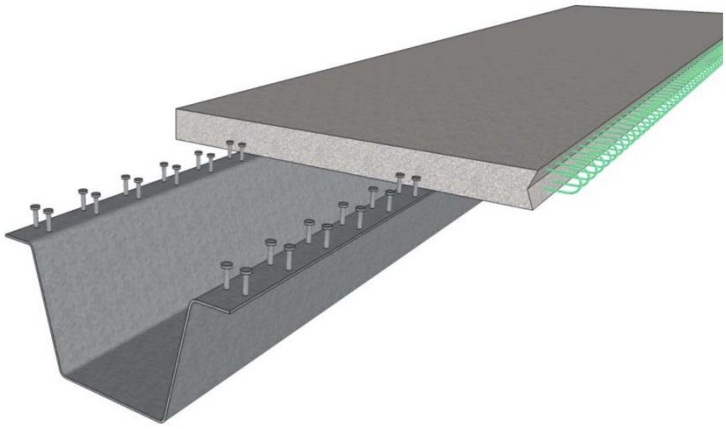

Figure 2.1: Proposed Modular PBFTGs System (Michaelson, 2014)

The design methodolgy for the press-brake-formed tub girder system tailored for short-span bridges underwent meticulous development, involving iterative designs employing standard mill plates. Various commerically available plate thicknesses and widths were analyzed while maintaining specific design constants such as a 1:4 web slope and predetermined bend radii (Michaelson, 2014) to ensure consistency. A comprehensive tool was devised to calculate section properties for a matrix of tub girder configurations and plate sizes, followed by a parametric study of design iterations to determine the optimal depth for each plate. For the 120-inch plate size, the optimal depth was approximately 34 inches. Each girder's non-composite and composite section properties were also computed as part of the parametric study. Figure 2.2 offers insight into a sample from the parametric study, revealing the intricate process of determining optimal configurations for PBFTGs.

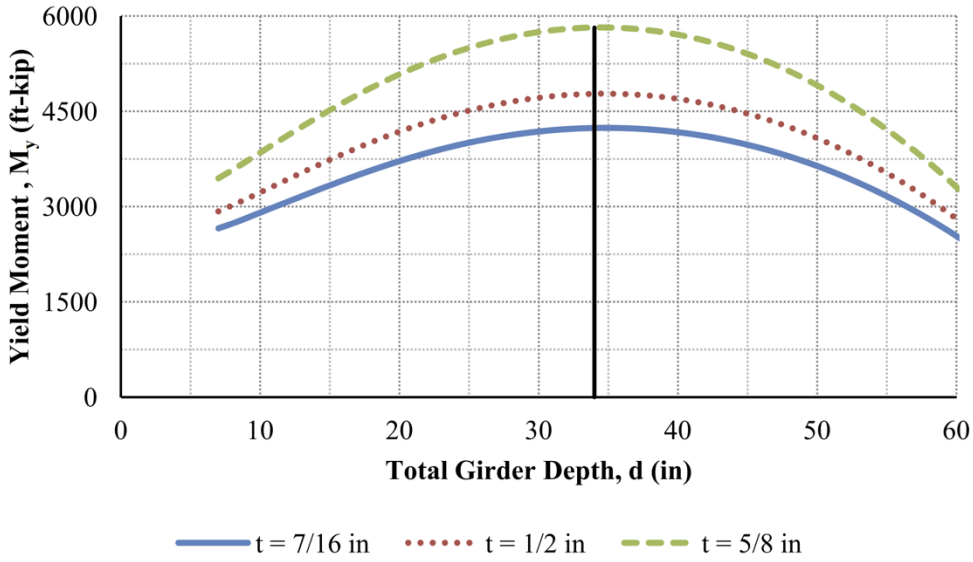

***Figure 2.2**: 120" Wide Standard Mill Plate Design Comparisons (Michaelson, 2014)*

Following the design phase, Michaelson conducted extensive destructive physical testing on composite and non-composite PBFTGs, employing standardized dimensions formed from an 84-inch wide, 7/16-inch thick, and 35-foot-long plate. This plate size was specifically chosen as it was necessary to ensure an MTS 330-kip servo-hydraulic actuator could cause the specimen to reach failure. Each girder underwent three-point bending tests, with composite modules demonstrating failure at approximately 300 kips, leading to concrete deck damage and loss of composite action, as shown in Figure 2.3. The data gathered from these experiments validated finite element analytical studies, with a three-dimensional nonlinear finite element model effectively capturing the behavior of both composite and non-composite PBFTGs. This comprehensive study not only affirmed the system's efficiency and applicability but also evaluated its compatibility with the AASHTO LRFD BDS, as it accurately illustrated the composite girder's behavior up to their failure (which is also modeled in Figure 2.3).

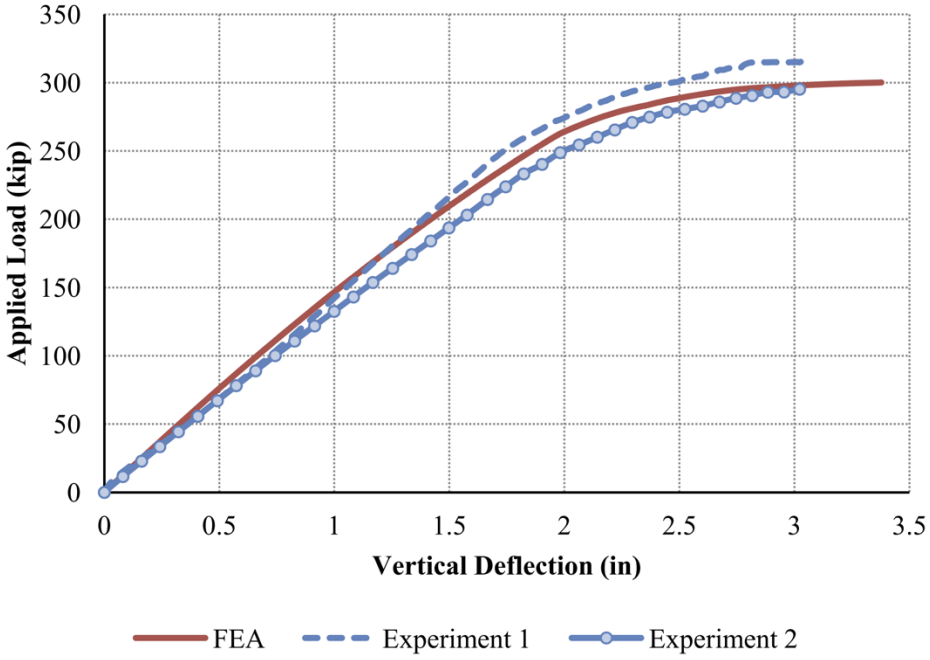

Figure 2.3: Comparison of Experimental and Analytical Results for the Composite Tests (Michaelson, 2014)

Post-behavioral studies, Michaelson explored the system's applicability in the short-span bridge sector through a feasibility study, assessing maximum span lengths for each plate dimension while considering Strength I and Service II limit states, along with live load deflection. After careful evaluation of various plate dimensions, three plate sizes were identified as suitable for widespread application, with the largest system proposed utilizing a 120-inch wide by 5/8-inch-thick plate capable of accommodating spans up to 80 feet.

2.2.2 Experimental Evaluation of Non-Composite Shallow Press-Brake-Formed Steel Tub Girders (Kelly, 2014)

Kelly's (2014) extensive study delved into the structural behavior of non-composite PBFTGs, explicitly focusing on their stability and torsional characteristics. The research centered on experimental tests conducted on two full-scale PBFTG specimens, depicted in Figure 2.4. To replicate real-world bridge conditions, the girders underwent rigorous three-point bending tests.

Methodologically, parameters such as deflection, strain, and rotations were meticulously recorded using a combination of precision level strain gauges and linear variable differential transformers (LVDTs). Unlike Michaelson's (2014) proposal for a pre-cast concrete deck, this study examined a cast-in-place deck. The critical phase of the cast-in-place deck lies during construction, as the non-composite section must withstand construction loads. The initial experiment revealed a linear load deflection curve reaching approximately 94 kips, corresponding to a midspan vertical deflection of 2.25 inches, culminating in abrupt failure due to lateral torsional buckling. A subsequent test on a galvanized sample exhibited similarities to the first. However, it terminated prematurely at around 33 kips due to excessive lateral deflections, attributed to initial imperfections and their second-order effects.

Figure 2.4: Non-composite test specimen Setup (Kelly, 2014)

Kelly employed Finite Element Analysis (FEA) to validate the experimental results, similar to (Michaelson, 2014). This technique played a pivotal role in predicting the structural behavior of PBFTGs under various load conditions. The FEA models were meticulously calibrated based on the physical properties and dimensions of the tested specimens. By replicating the same three-point bending tests in the analytical environment, Kelly could closely examine the girders' stress distribution, deformation patterns, and potential buckling zones. Comparisons between the experimental results and FEA predictions revealed a significant correlation, affirming the accuracy of the modeling process. As depicted in Figure 2.5, this alignment not only validated the

experimental findings but also emphasized the potential of FEA as a dependable tool for forecasting the performance of PBFTGs in practical scenarios.

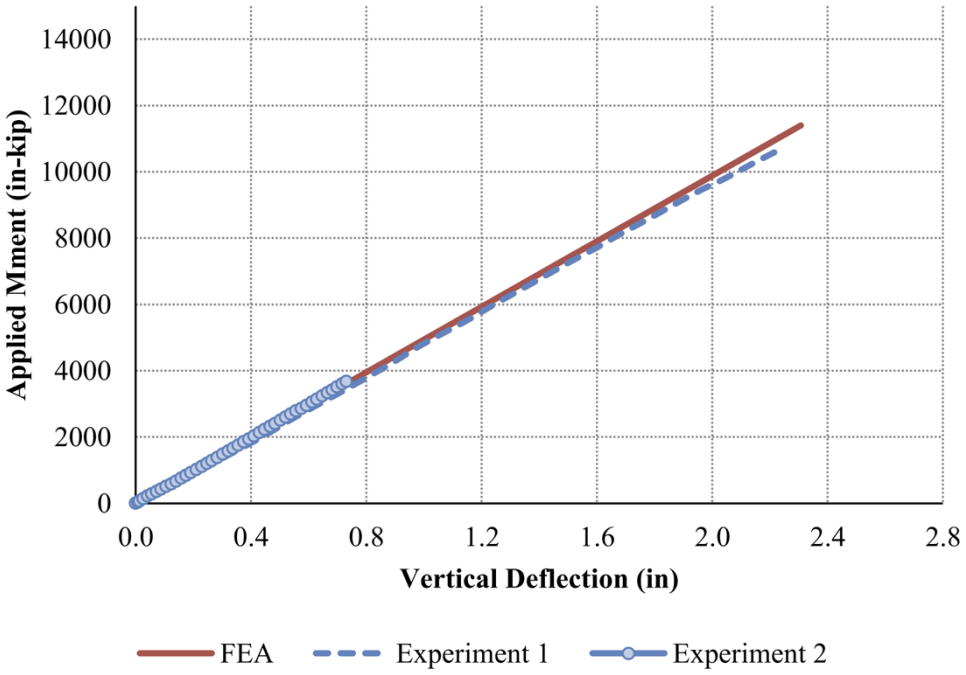

Figure 2.5: Mid-span Moment Comparison (Kelly, 2014)

2.2.3 Field Performance of Press-Brake-Formed Tub Girder Superstructures (Gibbs, 2017)

Gibbs conducted an in-depth examination of the inaugural on-field performance of a bridge constructed with PBFTGs. The subject under scrutiny, the Amish Sawmill Bridge in Buchanan County, Iowa (as depicted in Figure 2.6), comprises a PBFTG system featuring four galvanized tub girders, each forged from a 96-inch wide by ½-inch-thick plate. The study's primary objective was to assess and validate live load field test results, complemented by finite element modeling to decipher the live load distribution mechanism. Bridge Diagnostics, Inc's strain gauges were strategically positioned on the bottom flange of each tub girder, ensuring redundancy and precision, with three gauges affixed to each girder's midspan.

Figure 2.6: Amish Sawmill Bridge (Gibbs, 2017)

Recording the axle weights and loading vehicle positioning facilitated their accurate replication in the FEA. As delineated, the bridge's symmetrical, non-skewed design streamlined the testing regimen, requiring only five truck runs shown in Figure 2.7. These runs were meticulously charted to optimize load placements on interior and exterior girders under varied scenarios. The LLDFs were derived by normalizing the strain in a specific girder against the cumulative strain across all girders. For multi-lane scenarios, strain values from two truck runs were overlaid to generate the LLDFs.

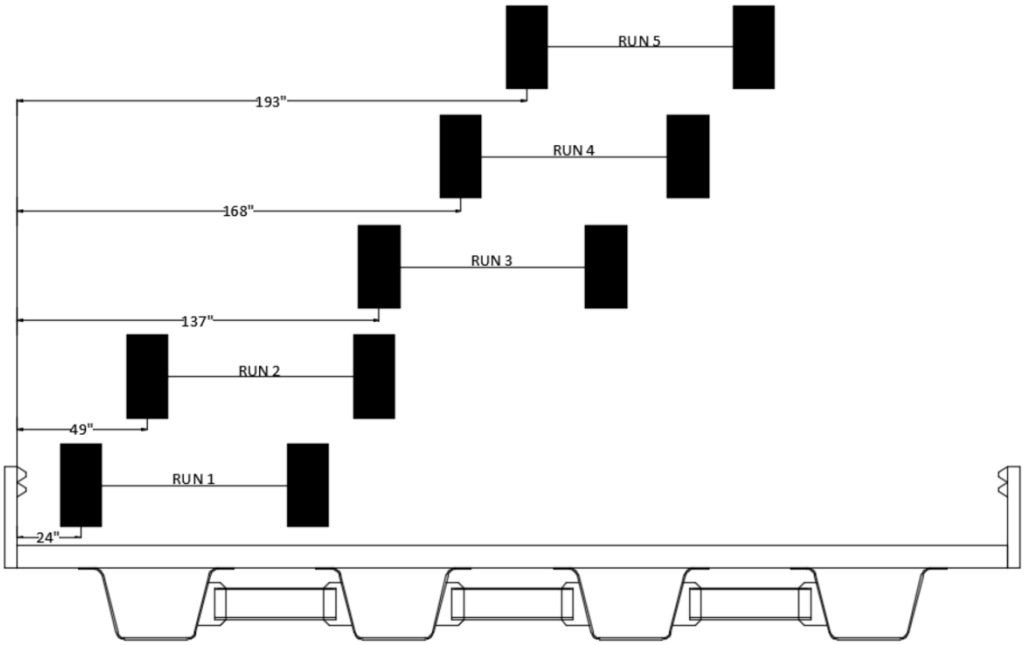

Figure 2.7: Live Load Truck Placements (Gibbs, 2017)

While the analytical and experimental values aligned remarkably well, FEA-calculated bottom flange strains marginally exceeded those from on-site tests. This discrepancy was attributed to the unique boundary conditions of the Amish Sawmill Bridge, which, unlike traditional 'hinge-roller' supports, employed integral abutments, enveloping each girder's ends in concrete and imparting stiffer support. However, the finite element model refrained from incorporating these integral abutments due to the complications and uncertainties associated with their modeling. A view of the Abaqus strain distribution is provided in Figure 2.8. Further analytical investigation culminated in a comparative analysis of the derived LLDFs relating those prescribed by the AASHTO LRFD BDS. Figure 2.8 also delineates the alignment between analytical and experimental LLDFS, compared with the considerably overestimated LLDFs obtained from the AASHTO LRFD BDS for single-lane scenarios.

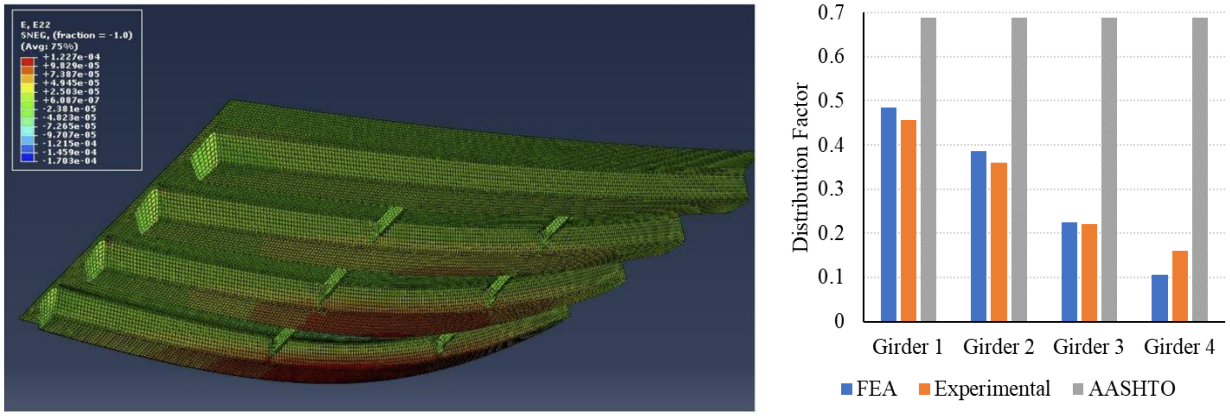

Figure 2.8: Deflected Shape of an Abaqus Model and LLDF Comparison for Truck Run 2 (Gibbs, 2017)

Gibbs' exhaustive investigation emphasized the consistent independent performance of PBFTGS. It also suggested that while the AASHTO LRFD BDS's LLDFs adopt a conservative stance, their exists possibility for refinement. Gibbs advocated for further research endeavors aimed at modifying the AASHTO LRFD BDS equations to reflect actual load distribution dynamics of PBFTGs more accurately.

2.2.4 Fatigue Performance of Uncoated and Galvanized Composite Press-Break-Formed Tub Girders (Tennant, 2018)

Galvanic surface treatments, effectively provide corrosion resistance to steal members, but industry concern has arisen with the fatigue performance over the reheating of cold-formed members. Tennant (2018) examined the fatigue performance of two specimens with varying surface treatments. Both girders were produced using ASTM A709 Grade 50 steel; one was left uncoated, and the other was hot-dipped galvanized, as shown in Figure 2.9. The composite system was fatigue-loaded to simulate a 75-year life in a non-interstate rural environment with an ADT of 800 vehicles, 15% of which were assumed to be truck traffic. At a predetermined number of load cycles, a Service II moment was induced in the system to observe the performance of the specimen. A combination of LVDTs and strain gauges were used to measure deflections that could be compared for each service loading interval.

Figure 2.9: Uncoated and Galvanized Steel Girder Under Fatigue Loading (Tennant, 2018)

A 6-inch-thick concrete deck was cast in place for each character to become a composite specimen. Compressive testing of cylinder samples taken from the casting revealed that the deck on the galvanized girder had a significantly lower compressive strength than the deck on the uncoated girder. To confirm precision, loads applied by the servo-hydraulic actuator were compared to loads calculated from the measured strain data, and the differences were minor. The project concluded that the heat of the galvanization process had no adverse effect on the performance of a press break formed steel tub girder.

2.2.5 Field Performance and Rating Evaluation of a Modular Press-Brake-Formed Tub Girder with a Steel Sandwich Plate Deck (Underwood, 2019)

The Cannelville Road Bridge in Muskingum County, Ohio, was the first bridge built in the United States that utilized modular units of its type. The bridge was composed of two modular units; each made up of two press-break-formed tub girders attached to a sandwich plate steel (SPS®) deck with bolts. An SPS® deck system is a thin, lightweight, innovative solution particularly useful in areas with limited hydraulic openings and those with a need for rapid construction methods. The tub girders were fabricated from a 5/8-inch-thick plate and braced at various locations internally and externally. The entire unit was hot-dipped galvanized to provide

corrosion resistance. Figure 2.10 shows one of the modular units on site. Erection of most of the superstructure was placed in under 30 minutes, and the entire project used less than the 30 allotted days from demolition of the old bridge to carrying traffic on the new bridge.

Figure 2.10: Cannelville Road Bridge Modular Unit (Underwood, 2019)

Underwood (2019) Worked to perform live load testing of the bridge to assess the applicability of AASHTO LRFD BDS for press-brake-formed tub girders topped with an SPS® deck. The structure was instrumented with Bridge Diagnostics, Inc. equipment, and a tandem axle load truck was placed at predetermined to grid points. Five runs were performed to collect data to determine a baseline measurement. The bottom flange strains of each girder and the weight of each wheel on the load truck were recorded using strain gauges that were adhered to the bottom of each for further analysis.

A finite element model that replicated the field model was produced to compare the data collected in the field. LLDFs were calculated for both the finite element model and the experimental data, and the results were then compared to LLDFs calculated per the AASHTO LRFD BDS. Inventory and operating load ratings for interior and exterior gutters were computed from field data and the analytical model. Live load ratings obtained from field and finite element

models were compared to AASHTO serviceability and strength requirements. Both showed themselves to be comparable and met AASHTO requirements. This test also assessed the validity of the current AASHTO LRFD BDS requirements for bridges of this type. The data displayed that the AASHTO LRFD BDS provisions tend to be conservative and underpredict the performance of the press-brake-formed tub girder system against both the field assessments and the final element analysis. It was confirmed that the standard provisions safely model press-break-formed tub girders.

2.2.6 Field Evaluation of a Modular Press-Brake-Formed Steel Tub Girder in an Application that Includes Skew and Superelevation (Roh, 2020)

Roh (2020) undertook a comprehensive endeavor focusing on the Fourteen Mile Bridge in Lincoln County, West Virginia, encompassing design, construction, and elevation. This 58-foot single-span bridge, traversing the Fourteen Mile Creek on State Route Number 37, boasts a distinctive design incorporating a 10° skew angle and an 8% superelevation. Comprising five modular composite units of PBFTGs, pre-assembled offsite, the bridge integrates 96-inch wide, 1/2-inch thick AASHTO M270 steel plates. Plates were meticulously fabricated to include sheer studs, end-bearing diaphragms, and mounting angles for internal formwork. Galvanized for corrosion resistance, these units underwent subsequent procedures, including internal and external formwork creation, rebar placement, and concrete casting in a controlled environment.

The construction methodology, underscore by Accelerated Bridge Construction (ABC) strategies, prioritized efficiency and quality enhancement. Leveraging the advantages of offsite fabrication, the research emphasized the controlled environment's benefits, ensuring consistent concrete application and optimal curing conditions to uphold structural integrity. On-site, the precast modular units were seamlessly lifted from transport trucks onto the bridge's abutments, eliminating the need for additional staging yards. Notably, ultra-high-performance concrete (UHPC) for closure pours further improved the bridge's resilience due to its exceptional compressive strength and rapid curing properties. Remarkably, the composite PBFTG modules' high torsional stiffness obviated the necessity for additional exterior or interior bracing, epitomizing a harmonious blend of efficiency and structural robustness. The comprehensive effort also involved the deployment of the BDI STS Wi-Fi Data Acquisition System for meticulous

testing and instrumentation, complemented by nineteen strategically positioned strain gauges. Additionally, the bridges layout was meticulously delineated with a grid of panel points, serving as reference markers for precise truck placements during live load testing, a vital aspect captured in Figure 2.11.

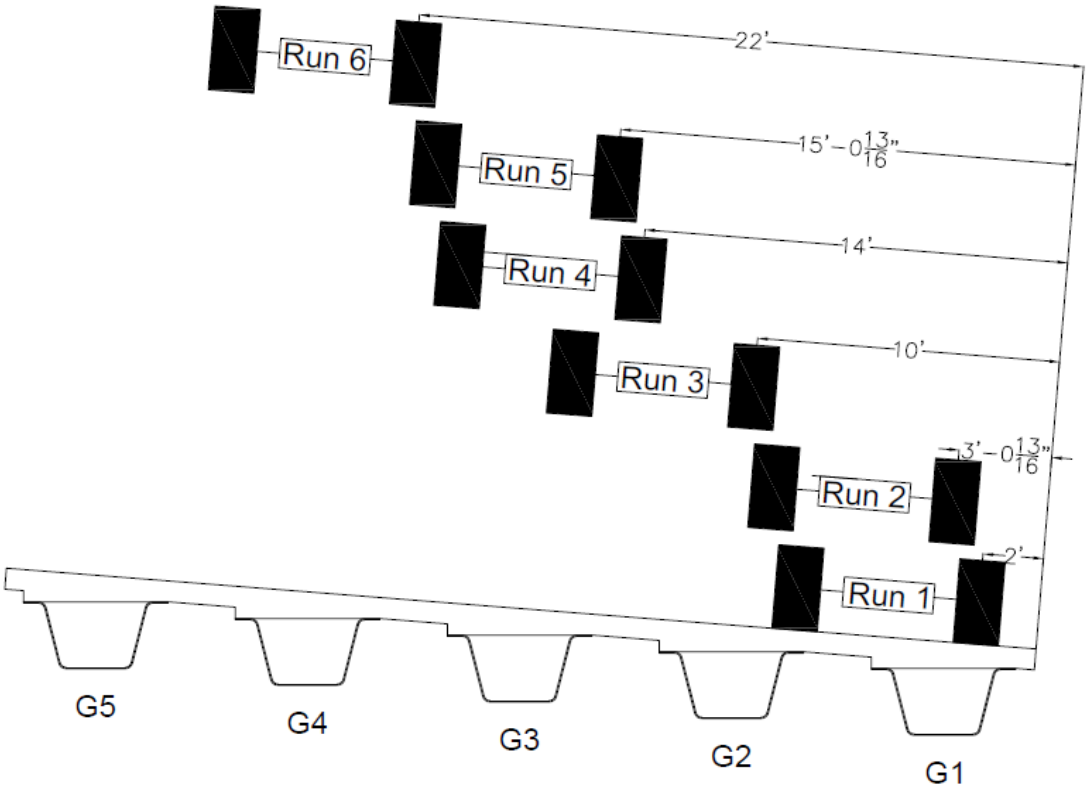

Figure 2.11: Live Load Truck Placement (Roh, 2020)

During live load field testing, a tandem axle truck was utilized to mimic the HS-20 design load truck outlined in the AASHTO LRFD BDS. The organization of the truck's positioning across the bridge was particularly planned, ensuring perfect alignment with the designated grid to maximize strain on targeted girders. Notably, detailed documentation of each wheel's weight and axle geometries was precisely recorded during this on-site testing endeavor, offering invaluable insights to the bridge's performance under live loading conditions when combined with analytical data.

Averaged strains from the bottom flange in multiple presence factors were employed to calculate Live Load Distribution Factors (LLDFs) using the same methodology espoused by Gibbs (2017). Specifically, the truck's placement at midspan was deliberately chosen for evaluation, given its maximum impact on the girders. To facilitate a comprehensive comparative analysis, these field test results were contrasted against readings derived from finite element models and the established standard defined by the AASHTO LRFD BDS, as explained in Figure 2.12. Remarkably, the analytical modeling results closely mirrored the outcomes of the field test, ball strain confidence in the precision of both methodologies.

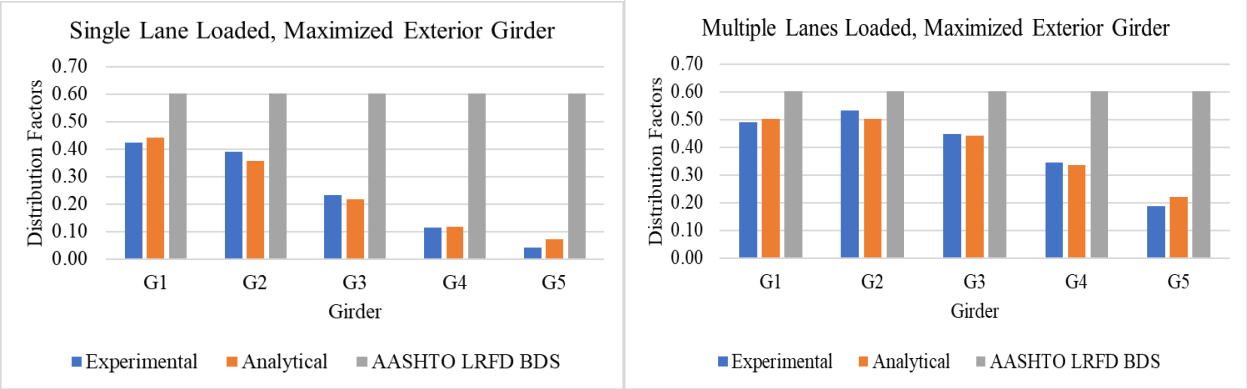

Figure 2.12: Comparison of Analytical, Experimental, and AASHTO Results (Roh, 2020)

As highlighted by Gibbs (2017) and reaffirmed by Roh (2020), the congruence between experimental findings and finite element model results was prominent. However, the standards outlined in the AASHTO LRFD BDS were observed to adopt a more conservative approach. Notably, the AASHTO equations projected significantly higher distribution factors, particularly in scenarios with single-lane loading conditions. Despite the conservative nature of the AASHTO standards, the study underscored the safety and reliability inherent in the performance of PBFTGs.

2.2.7 Expanding the Applicability of Press-Brake-Formed Tub Girders Through the Extension of the Maximum Span Length and the Evaluation of Pier Continuity (Tennant, 2022)

Tennant (2022) delved into expanding the scope of PBFTGs' applicability through a meticulous blend of analytical examination and laboratory experimentation. Central to the

investigation was integrating link slabs with modular PBFTGs in continuous span configurations and thoroughly exploring the constraints applied to box-section flexural members concerning PBFTGs. The research journey commenced within an exhaustive literature review spanning PBFTGs, link slab details, live load distribution, and the consequential impact of compactness on flexural capacity for skewed PBFTGs. Subsequently, bespoke analytical tools were crafted to analyze the behavior and capacity of PBFTGs, accommodating varying dimensions, properties, and parameters. This analytical groundwork was further developed by behavioral and parametric studies aimed at analytical, critical parameters dictating the computation of live load distribution factors for PBFTGs, alongside behavioral inquiries to gauge the skew's influence on PBFTGs' ultimate capacity. Practical insights and supporting data for the analytical work were gathered through flexural testing on modular units joined transversely by a link slab, culminating in a comprehensive understanding and assessment of PBFTGs across diverse applications, thus validating or refining existing constraints as warranted.

In crafting the analytical framework, Tennant (2022) meticulously calibrated various laboratory experiments and two live-load field tests, including one orchestrated by Roh (2020). The study harnessed both the Stallings/Yoo and Tarhini/Frederick (1992) methodologies to compute Live Load Distribution Factors (LLDFs), with the latter method introduced specifically for this research endeavor. The ensuing comparative analysis between field data and the analytical model, with a spotlight on Girder 1 under one design lane load, showcased negligible discrepancies between the two LLDF calculation methods and the live load field test. This resounding alignment underscores the reliability of the analytical modeling techniques leveraged for LLDF determination in PBFTG bridges.

The literature review is intricately intertwined with examining a matrix of bridge models, precisely generated and studied via finite element software, with the overarching aim of unraveling the sensitivity of various parameters concerning live load distribution. A tailored modified matrix was conceived, zeroing in on parameters of paramount significance. Four standard PBFTG bridge scenarios were generated and analyzed, focusing on understanding how specific parameters influence live load distribution in PBFTG bridges. This is achieved through a detailed analysis of a matrix of bridges using Abaqus/CAE, where parameters are either held constant or varied to observe their impacts. The dimensions of the standard bridges are given below in Table 2.1.

Table 2.1: Standard Bridge Dimensions Used for Sensitivity Study (Tennant, 2022)

Bridge Number	Plate Size (in)	Span Length (ft)	Number of Girders	Girder Spacing (ft)	Deck Thickness (in)	Overhang Width (ft)
1	72 x 1/2	30	3	6	8	2.22
2	84 x 1/2	40	4	8	8	2.11
3	96 x 1/2	60	5	8	8	1.8
4	120 x 5/8	80	6	10	8	1.29

The constant parameters include dimensions related to the bridge's structural elements, material properties of concrete and steel, and specific boundary conditions. The varied parameters, encompass various possibilities, including different span lengths, number of girders, individual PBFTG cross-sections, girder spacings, deck thicknesses, overhang ratios, and load placements. These varied parameters provide a comprehensive view of how different aspects of bridge design can influence live load distribution. Figure 2.13 shows the cross-section of the standard bridge.

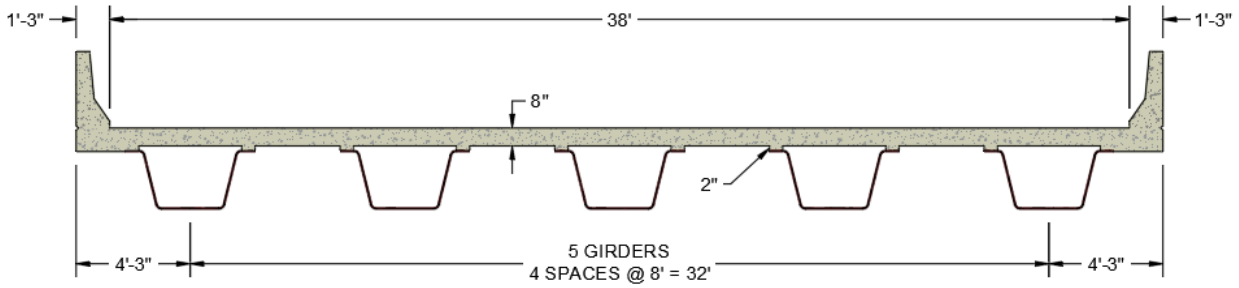

Figure 2.13: Sensitivity Bridge Cross-Section (Tennant, 2022)

The sensitivity study yielded extensive results, showcasing the influence of each varied parameter on live load distribution. It is observed that the LLDFs derived from analytical modeling generally tend to be lower than those calculated using empirical equations from the AASHTO LRFD BDS, with specific trends noted for one-lane and two-lane loaded scenarios. The study provides a granular view of how parameters such a span length, number of beams, PBFTG size, girder spacing, deck thickness, and overhang ratio impact LLDFs. For instance, span length and girder spacing have a significant effect on LLDFs, whereas deck thickness has a negligible impact.

The overhang ratio, while having a minimal effect on interior girder LLDFs, shows a noticeable influence on exterior girder LLDFs. Figure 2.14 presents a sample of graphs used in the sensitivity study.

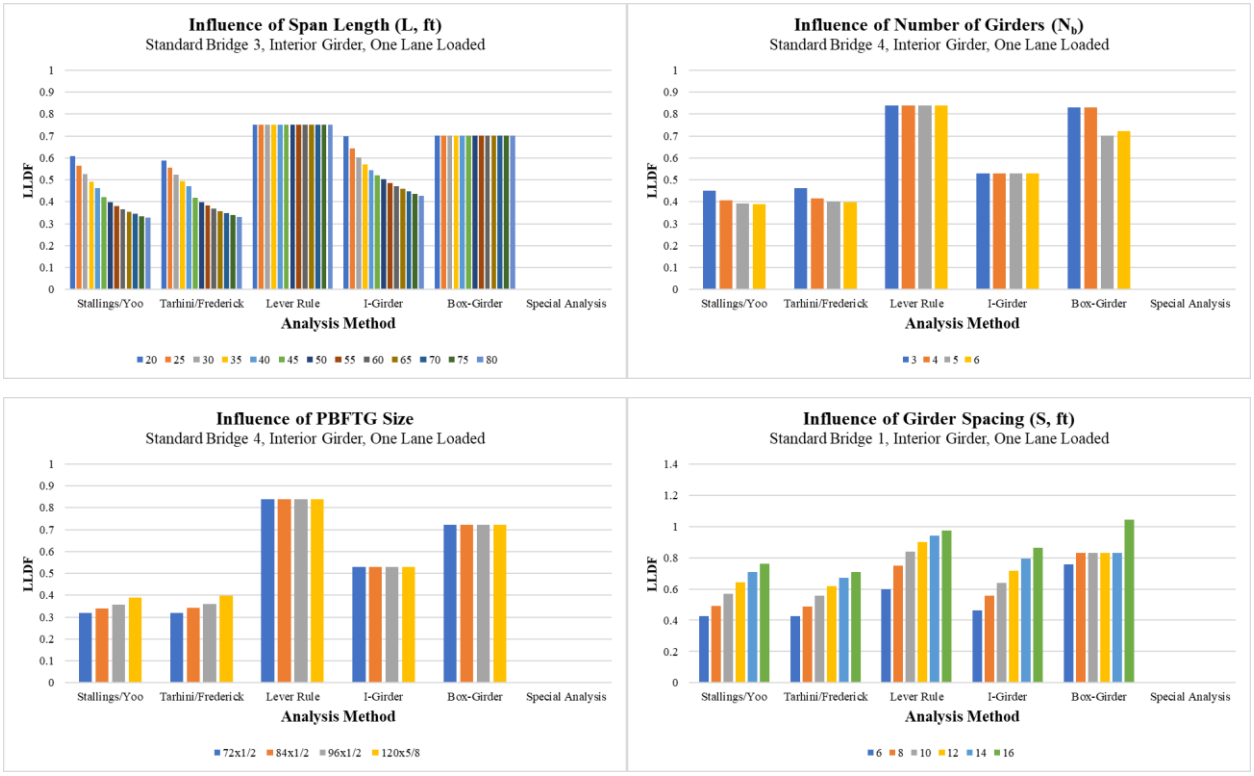

Figure 2.14: Results of the Sensitivity-Study Analysis Performed to Assess the Influence of Numerous Parameters (Tennant, 2022)

The exhaustive sensitivity study and ensuing analysis furnished a robust toolkit for further exploration of LLDF for PBFTGs, laying the groundwork for future inquiries into PBFTG dynamics. While results of the behavioral study on skewed PBFTGs showed that the flexural capacity of girders with skews up to 20° is consistent with those with 0° of skew, as seen when compared to data collected from Michaelson's (2014) experimental study. The flexural capacity for girders with skew angles greater than 20° was abruptly terminated in their respective analytical models.

2.2.8 Development and Validation of Improved Live Load Distribution Factors for Moment in Press-Brake-Formed Steel Tub Girder Bridges (Woldegabriel, 2023)

Woldegabriel (2023) explored the live load distribution factors (LLDFs) for a matrix of analytical bridge models with varied parameters to develop an improved set of empirical equations, through the assistance of statistical modeling, that can effortlessly and accurately predict LLDFs for PBFTGs. Multiple field experiments helped determine that the empirical equations to predict LLDFs for PBFTGs in AASHTO LRFD BDS are highly conservative. Woldegabriel employed many finite-element modeling techniques that were previously determined by other researchers at WVU. The FEA modeling techniques in this study were benchmarked against three field experiments to validate the techniques employed prior to matrix modeling. An analytical model was run for each field experiment bridge, before undergoing statistical analysis for validation. The experimental and FEA LLDFs were compared using a matched pair t-test. Results of these statistical tests concluded to have mean differences as low as 2.5e-10, suggesting the FEA modeling techniques used were accurate to produce negligible differences in results.

Woldegabriel's research efforts aimed to determine improved, simplified, empirical equations to determine LLDFs for interior and exterior girders. An extensive matrix of PBFTG bridges, with varying parameters, was modeled using three-dimensional finite-element modeling software Abaqus. The varying parameters assessed in the parametric study included plate size, number of girders, girder spacing, deck thickness, overhang ratios, and one-lane or two-lane loading scenarios. Simplified equations were then developed through the use of JMP statistical modeling software. A thorough evaluation of the predictive accuracy of these proposed equations reveals their markedly superior performance compared to existing AASHTO prediction equations. By employing these proposed equations, bridge engineers can streamline the design process when utilizing PBFTGs with line girder analysis.

The current provisions of AASHTO LRFD BDS for multiple box sections are noted for their conservatism and considerable restrictiveness when applied to PBFTGs. Notably, the limitation on adjacent flange spacing in the current equation is expanded to encompass a broader range, extending from 12.5% to 157%. Meanwhile, the lower bound for applicability, is reduced to 0.25. 23

Aside from their enhanced accuracy and precision in predicting LLDFs, the proposed equations offer a known statistical certainty, a feature lacking in the AASHTO LRFD BDS equation. Specifically, the proposed equation is estimated based on a 95% Prediction Interval (PI) and approximately 98% Confidence Interval (CI). Consequently, it is anticipated that with a sufficient number of samples, future LLDFs for bridges sharing key bridge parameters within the range of those in the analyzed bridge sample will be accurately estimated or overestimated 95% of the time using the proposed equations (with a 98% or higher probability of overestimating the actual LLDF obtained via FEA for the average LLDF). Figure 2.15: Q-Q plot of LLDFs for Valmont U-BEAMs (Woldegabriel, 2023) presents the LLDFs for the matrix using the proposed equations against the current AASHTO prediction equations.

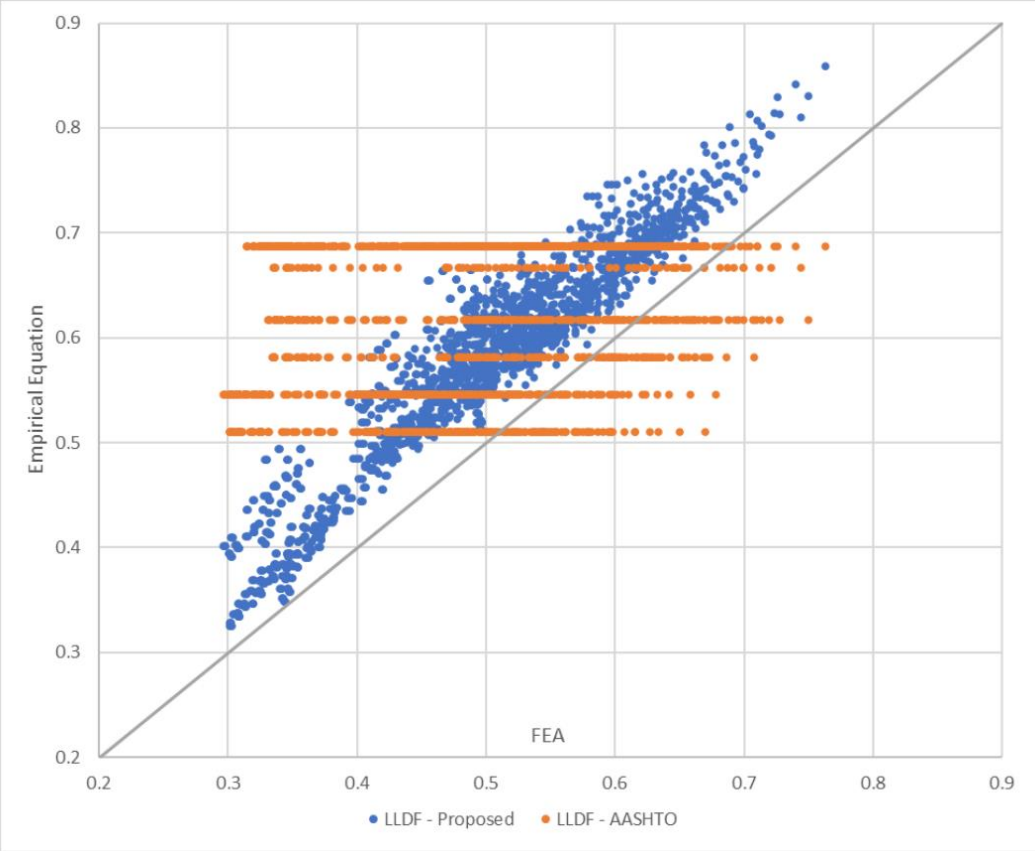

Figure 2.15: Q-Q plot of LLDFs for Valmont U-BEAMs (Woldegabriel, 2023)

Furthermore, the proposed empirical equations were assessed for their goodness-of-fit and predictive accuracy through an exploratory statistical analysis and comparison with other 24

commercially available shallow tub girder systems. Woldegabriel performed a feasibility assessment to explore of the impacts of adopting the proposed equations into AASHTO LRFD BDS, which reaffirms the significantly higher predictive accuracy of the proposed equations compared to current AASHTO prediction equations. The results of this research effort strongly suggest that the proposed equations are transferable and generalizable, accurately predicting LLDFs for bridges beyond the dataset used in their development.

In conclusion, the empirical equations Woldegabriel proposed offer a simplified design process for bridge engineers utilizing shallow steel tub girders and have the potential to substantially increase the span length applicability for these types of girder systems.

2.2.9 Rapid, Economical Bridge Replacement (Chandar et al., 2010)

In 2010, the Texas Department of Transportation (TxDOT) aimed to upgrade the sections of I-35 from a four-lane interstate highway to six-lanes. This project focuses on the FM3267 bridge located 75 miles north of Austin on one of the busiest segments of this interstate highway system (Chandar et al., 2010). This project's scope was to find a solution that created a shallower bridge superstructure with rapid constructability without jeopardizing the desired design aesthetic.

A solution involving shallow trapezoidal steel box girders was developed. Tub girders consisting of a 5-foot-wide bottom flange and a 3-foot-deep web were designed corresponding to the 2004 AASHTO LRFD BDS (as shown in Figure 2.16). Girders were checked for ultimate strength, stress, and deflection (Chandar et al., 2010). Two rows of shear studs were welded to each 18-inch-wide top flange before a concrete deck was cast in place. The completed bridge consisted of six tub girders spaced 13.2 feet apart to meet the required overall 78-foot width. Four simply supported spans of 45 feet, 100 feet, 100 feet, and 65 feet were utilized.

Unlike the press-brake-formed tub girders discussed earlier in this chapter, this solution utilized conventionally fabricated (welded) steel tub girders.

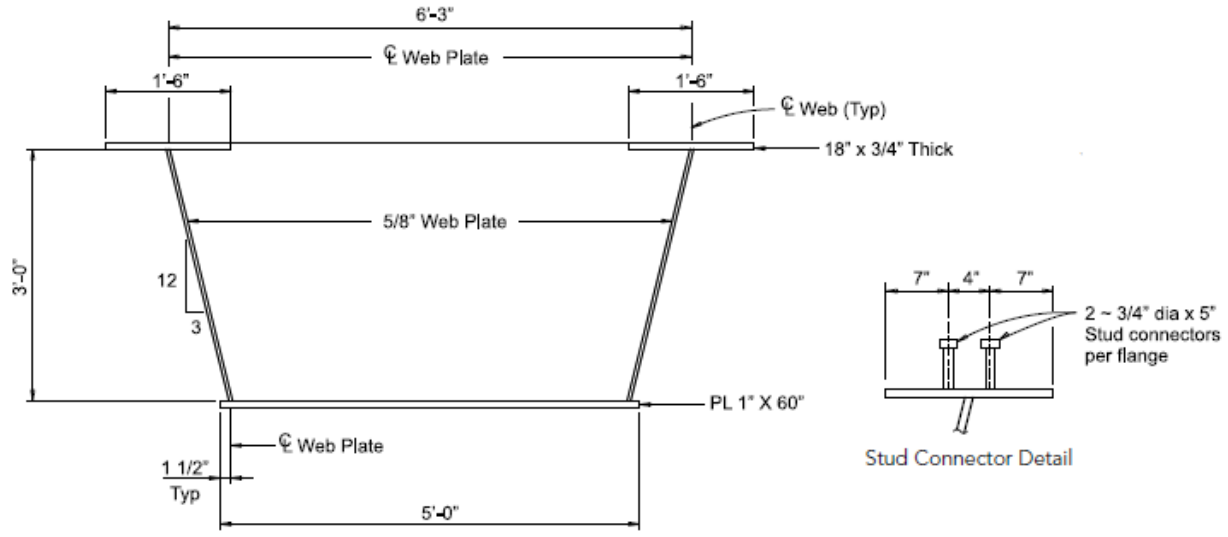

Figure 2.16: TxDOT Tub Girder for Rapid, Economical Bridge Replacement (Chandler et al., 2010)

2.3 CONCLUSION

Michaelson (2014) embarked on an extensive examination, unveiling an inventive modular design paradigm for PBFTGs strategically positioned as a substitute for conventional concrete box beams in short-span bridges spanning up to 90 feet. This pioneering approach, entailing the cold bending of standard steel plates into trapezoidal box girders, promises expedited bridge construction timelines while mitigating traffic disruptions—a testament to its composite modular unit architecture adaptable to diverse deck configurations. Conversely, Kelly (2014) delved into the nuanced structural dynamics of non-composite PBFTGs, focusing on stability nuances and torsional behaviors unveiled through empirical testing endeavors, shedding light on pivotal construction nuances associated with cast-in-place decks. Gibbs (2017) and Roh (2020) further propelled the boundary of PBFTG applications into real-world contexts, respectively studying on-field performance distinctions and refinement construction methodologies, underscoring accelerated bridge construction modes, and fostering quality assurance frameworks anchored in meticulously controlled environments. Tennant (2022) charted new horizons by expanding the applicability of PBFTGs across varied configurations, thereby promoting a complete understanding of these structural systems' potential.

CHAPTER 3: OVERVIEW OF CURRENT AASHTO LRFD SPECIFICATIONS FOR PBFTGS

3.1 INTRODUCTION

This chapter details the guidelines provided by the American Association of State Highway and Transportation Officials Load Resistance and Factor Design Bridge Design Specifications (AASHTO LRFD BDS). AASHTO LRFD BDS (2020) is the current set of governing standards for the design of highway bridges in the United States. Section 6 contains guidelines for designing steel structures, while Article 6.11 specifically relates to composite box-section (or tub girder) flexural members. Nevertheless, some of these sections may not fully align with the requirements for the analysis and capacity of cold-bent press-brake-formed tub girders. A review of this section is necessary to determine the applicability of the provisions to this system. This review will help to expand the applicability of tub girders in highway design and propose modifications to the specifications.

3.2 STRUCTURAL LOADS

Bridges face diverse loads throughout their lifespan, crucially categorized into two primary types: permanent loads and transient loads. Understanding the distinction is paramount for designing, analyzing, and ensuring the safety of bridges. Permanent loads encompass both dead loads and earth loads. Dead loads refer to the unchanging, constant loads stemming from the structure itself, including all integral and attached components. This incorporates the weight of bridge girders, decks, and other structural elements alongside permanent fixtures like utilities, wearing surfaces, and provisions for future expansions such as bridge widening. AASHTO specifications provide valuable guidelines for estimating these loads using predefined unit weights of various materials, helping the calculation of total dead load, mainly when exact component weights are unknown.

Further delving into dead loads, they are subcategorized into non-composite and composite loads, depending on the construction phase. Non-composite dead loads, designated as DCI, encompass loads during the construction phase before achieving composite action. This phase

involves elements such as the self-weight of girders, wet concrete deck, stay-in-place metal formwork, concrete haunches, and overhang tapers. Until the concrete reaches 75% of its designated compressive strength, the load is assumed to be solely supported by the girders.

Table 3.1: Unit Weights (AASHTO, 2020)

Material		Unit Weight (kcf)
Aluminum Alloys		0.175
Bituminous Wearing Surfaces		0.140
Cast Iron		0.450
Cinder Filling		0.060
Compacted Sand, Silt, or Clay		0.120
Concrete	Lightweight	0.110 to 0.135
	Normal Weight with $f'_c \leq 5.0$ ksi	0.145
	Normal Weight with $5.0 < f'_c \leq 15.0$ ksi	$0.140 + 0.001\, f'_c$
Loose Sand, Silt, or Gravel		0.100
Soft Clay		0.100
Rolled Gravel, Macadam, or Ballast		0.140
Steel		0.490
Stone Masonry		0.170
Wood	Hard	0.060
	Soft	0.050
Water	Fresh	0.0624
	Salt	0.0640
Item		Weight per Unit Length (klf)
Transit Rails, Ties, and Fastening per Track		0.200

Once the concrete sets and achieves the required compressive strength, full composite action is established between the concrete deck and the steel girder. This marks the transition to composite dead loads, categorized as DC2 and DW. DC2 includes the weight of curbs, barriers, sidewalks, and pedestrian hand railings, all working in unison with the girders and deck. DW represents anticipated future wearing surface loads due to planned enhancements or modifications.

The focus of analysis often narrows down to dead loads and live loads (vehicular traffic), integral in Strength I, Service II, and Fatigue load combinations. These combinations are pivotal for understanding and preparing for the structural demands the bridge will encounter, contributing to a more robust design.

Vehicular live loads are standardized under HL-93 (shown in Figure 3.2), according to AASHTO Specifications. This model combines a uniform lane load with specific axle loads. It includes a lane load of 0.64 kips per foot, utilized alongside a design truck or a design tandem. The design truck features a three-axle configuration: an 8-kip front axle followed by two 32-kip

rear axles. The spacing between these rear axles varies from 14 to 30 feet, chosen to stimulate demanding load scenarios.

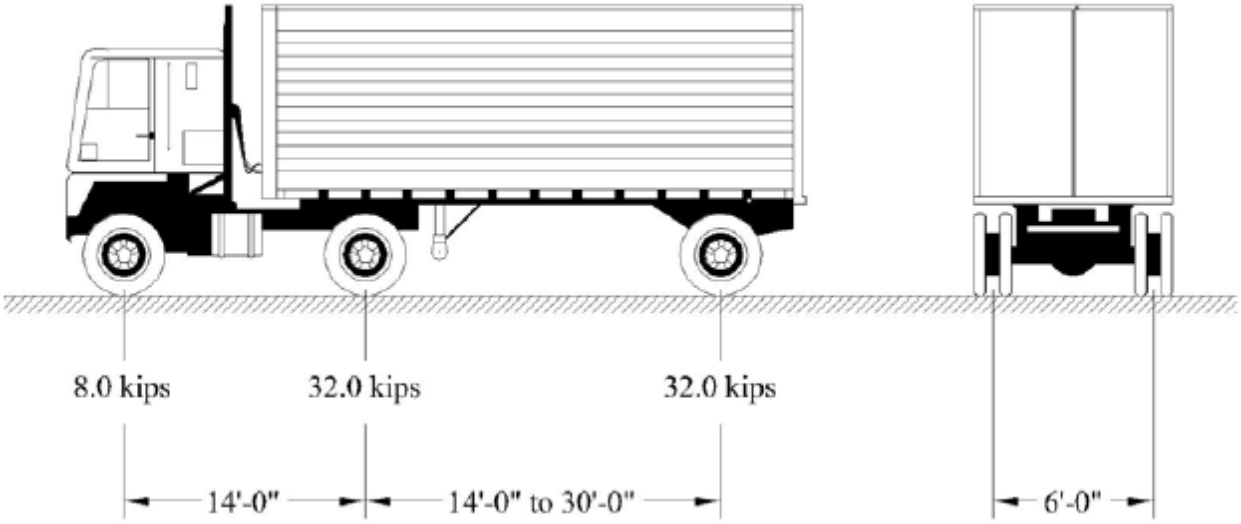

Figure 3.1: Characteristics of the Design Truck (AASHTO, 2020)

Conversely, the design tandem comprises two axles, each bearing 25 kips and spaced 4 feet apart. Careful longitudinal positioning of these loads on the structure is essential to determining the maximum live load response and ensuring the design accommodates critical loading conditions.

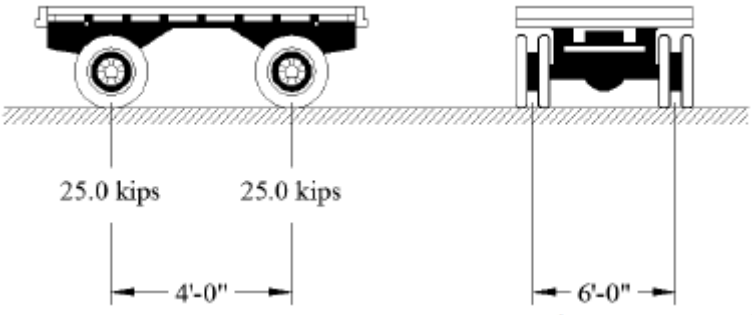

Figure 3.2: Characteristics of the Design Truck (AASHTO, 2020)

Dynamic load allowances (IM) are also considered, factoring in dynamic impacts of the design vehicle's interaction with the driving surface. These allowances enhance the effects of the design truck and design tandem, providing a more realistic approximation of live loads, considering the dynamic nature of vehicular traffic.

Moreover, beyond the completed state of the bridge, loads applied during construction necessitate thorough evaluation. These construction loads encompass various elements, demanding a strategic approach to ensure structural integrity during and post-construction, particularly in multiple-span bridges where deck casting sequences introduce additional complexity. Typically, the deck is initially cast in positive bending regions to mitigate the risk of cracking over piers, emphasizing the need for careful planning and execution.

3.3 SERVICE LOAD LIMIT STATE

To consider the statistical likelihood of varying loads coinciding, engineers use a set of load combinations or limit states during design. These load combinations work to ensure that a given structure can withstand uncertainties. Each load combination consists of a different combination of load types, including the most basic load types (dead and live loads) and more unpredictable environmental factors (like wind, seismic, or snow loads). Dead loads are considered permanent or static loads, like the weight of the bridge itself, for instance. Environmental loads take geographical location into account when utilized. Any given structure must satisfy the following equation when using the AASHTO LRFD BDS (2017) for design:

	$\sum \eta_i \gamma_i Q_i \leq \phi R_n = R_r$	Eq. 3.1

Where:	
η_i =	load modifier: a factor relating to ductility, redundancy, and operational classification
γ_i =	load factor: a statically based multiplier applied to force effects
Q_i =	force effect
ϕ =	resistance factor: a statistically based multiplier applied to the nominal resistance

R_n =	nominal resistance
R_r =	factored resistance

The equation is structured to ensure that, under all probable loading conditions, the structure remains safe and functional. It is a crucial aspect of structural engineering design, providing a mathematical framework to evaluate and validate the safety and stability of the proposed structure under various loading scenarios. To comprehensively address the durability and safety of bridges, engineering design employs a, multifaceted approach that includes various load modifiers and limit states:

- Load Modifiers: These are applied to account for the ductility, redundancy, and operational importance of the bridge, collectively forming the η_i term.
    - Ductility Load Modifier: Ensures that visible inelastic deformations occur before structural failure, enhancing safety.
    - Redundancy Load Modifier: Increases the resilience of the bridge system, preventing total collapse in case one member fails.
    - Operational Importance Load Modifier: Assigns higher resistance to bridges that are crucial for emergency roadways or have national security implications. For most bridges, this modifier is set to one.
- Strength Limit States: These are designated to ensure the bridge's strength and stability over its lifetime, considering both local and global components and connections.
    - Strength I: Considers basic load combinations under normal vehicular use without wind.
    - Strength II: Accounts for owner-specified vehicles or, evaluation permit vehicles, or both without wind loads.
    - Strength III: Relates exposure to the design wind speed at the location of the bridge.
    - Strength IV: Emphasized ratio of dead loas to live load force effects.
    - Strength V: Considers regular vehicular use with wind velocities of 80 mph.

- Extreme Event Limit States: Cover rare, but significant loads like earthquakes and vehicles collisions.
    - Extreme Event I: Earthquake loads.
    - Extreme Event II: Ice loads, collisions, floods, and other hydraulic events.
- Service Limit States: Focused on preventing excessive stress, deformation, and cracking under regular service conditions.
    - Service I: Normal bridge use with 55 mph wind, typically for checking deflection and concrete deck cracking.
    - Service II: Controls steel yielding and slip-in connections due to vehicular live load.
    - Service III: Crack control in prestressed concrete superstructure and girder members.
    - Service IV: Crack control in prestressed concrete columns.
- Fatigue and Fracture Limit States: Aimed at limiting stress range and preventing crack growth and fracture under repetitive loads.
    - Fatigue I: For infinite load-induced fatigue life.
    - Fatigue II: Related to finite load-induced fatigue life.

Each of these limit states plays a critical role in ensuring that bridges are designed to withstand a variety of stressors over their lifetime, maintaining safety and functionality.

3.4 Cross-Section Proportion Limits

AASHTO LRFD BDS provisions in Article 6.11.2 place cross-section proportion limits on both the webs and flanges to prevent erection issues from damage to the sections caused during handling or distortion due to welding. Web slenderness limits are specified for webs with or without longitudinal stiffeners. The structural health of the web is assessed through the following:

	$\frac{D}{t_w} \leq 150$	Eq. 3.2

Webs with longitudinal stiffeners:

	$\frac{D}{t_w} \leq 300$	Eq. 3.3

Where:	
D =	depth of the web plate measured along the slope
t_w =	web thickness

Moreover, adherence to these specifications outlined in AASHTO (2020) Article 6.11.2.1.2 is imperative, specifically for the web of box girders lacking longitudinal stiffeners. These guidelines ensure the optimal proportions and configurations to maintain structural integrity, mitigating issues like buckling or excessive deformation under load.

Flange proportion limits are set for top flanges and concern tub sections in compression and tension. Equations 3.4 through 3.6 are applied to only a single top flange of a tub section. The top flange must meet the lower limit on flange thickness to ensure the flanges will not distort during welding. A lower limit for flange width ensures adequate strength and moment rotation and that flanges extend a minimum of one inch beyond the outside edge of each web to permit welding access. The top flange must meet the following requirements:

	$\frac{b_f}{t_f} \leq 12.0$	Eq. 3.4
	$b_f \geq D/6$	Eq. 3.5
	$t_f \geq 1.1 t_w$	Eq. 3.6

Where:	
b_f =	total width of the widest top flange within the considered section
t_f =	flange thickness

The constraints outlined in AASHTO LRFD BDS Article 6.11.2.3 are established from the findings of Johnston and Mattock's (1967) research, focusing on the specific cross-sections

analyzed in their study. Furthermore, the commentary accompanying Article 6.11.2.3 explains that supports should not be skewed due to the additional torsional effects induced in the box section and the subsequent alteration of lateral load distribution. As Tennant (2022) also stated, no other steel section has limited capacity due to the restrictions placed on live load analysis.

3.5 CONSTRUCTABILITY

AASHTO LRFD BDS Article 6.11.3 delves into concerns regarding box section performance, encompassing aspects like deflection, steel strength, and stability during crucial stages of construction. While comprehensively referencing AASHTO LRFD BDS Article 6.10.3, it introduces significant inconsistencies. Unlike plate girders, which may employ varying flange thicknesses across the bridge span, tub girders must maintain consistent cross-section geometry. This is achieved through the implementation of a singular structural plate. Internal or external diaphragms or cross frames are used to regulate cross-section deformations.

Equations 3.7 through 3.9 serve as criteria for tub girders under flexural loading. While originally intended for I-section flanges, these equations are also applicable to the top flanges of tubular sections, where struts between the flanges can be regarded as brace points. AASHTO LRFD BDS categorizes flanges into discretely and continuously braced types, with the latter exempting consideration of flange lateral bending. Notably, Equation 3.8 is unnecessary for sections featuring compact or noncompact webs.

For discretely braced flanges in compression:

	$f_{bu} + f_l < \phi_f R_h F_{yc}$	Eq. 3.7
	$f_{bu} + \frac{1}{3} f_l \leq \phi_f F_{nc}$	Eq. 3.8
	$f_{bu} \leq \phi_f F_{crw}$	Eq. 3.9

For discretely braced flanges in tension:

	$f_{bu} + f_l < \phi_f R_h F_{yt}$	Eq. 3.10

For continuously braced flanges in compression or tension:

	$f_{bu} < \phi_f R_h F_{yt}$	Eq. 3.11

Furthermore, in combination with the requirements outlined in AASHTO LRFD BDS Article 6.10.3.2, additional requirements are outlined in AASHTO LRFD BDS Article 6.11.3 for noncomposite box flanges during critical construction stages:

	$f_{bu} \leq \phi_f F_{nc}$	Eq. 3.12
	$f_{bu} \leq \phi_f F_{crw}$	Eq. 3.13
	$f_{bu} < \phi_f R_h F_{yf} \Delta$	Eq. 3.14
In which:		
	$\Delta = \sqrt{1 - 3\left(\frac{f_{bu}}{F_{yf}}\right)^2}$	Eq. 3.15
	$f_v = \frac{T}{2A_o t_f}$	Eq. 3.16
Where:		
f_{bu} =	flange stress calculated without consideration of flange lateral bending (ksi)	
f_l =	flange lateral bending stress (ksi)	
ϕ_f =	resistance factor for flexure specified in Article 6.5.4.2 AASHTO (2020)	
F_{nc} =	nominal flexural resistance of box flanges in compression (ksi)	
F_{crw} =	nominal bend buckling resistance for webs (ksi)	
F_{yc} =	specified minimum yield strength of the compression flange (ksi)	
F_{yt} =	specified minimum yield strength of the tension flange (ksi)	
F_{yf} =	specified minimum yield strength of the flange under consideration (ksi)	
R_h =	hybrid girder factor determined as specified in Article 6.10.1.10.1 (only needed for box-sections that utilize different materials)	
Δ =	reduction factor for the maximum stress in a box flange	

f_v =	St. Venant torsional shear stress in the flange to the factored loads at the section
T =	internal torque caused by the factored loads (kip-in.)
A_o =	enclosed area within the box section (in.^{2})
t_f =	flange thickness (in.)

Webs shall satisfy the flowing shear requirements during critical stages of construction:

	$V_u \leq \phi_v V_{cr}$	Eq. 3.17
	$V_{ui} = \frac{V_u}{\cos\theta}$	Eq. 3.18

Where:	
V_u =	vertical shear due to the factored loads on one inclined web of a box section
V_{cr} =	shear buckling resistance
V_{ui} =	shear due to the factored loads along one inclined web of a box section
ϕ_v =	resistance factor for shear
θ =	angle of inclination of the web plate to the vertical

3.6 STRUCTURAL ANALYSIS PROVISIONS

Multiple presence factors account for the probability of multiple design lanes being loaded simultaneously. The extreme live load force effect is determined by considering each possible combination of the number of lanes loaded multiplied by the corresponding multiple presence factor. It should be noted that these factors are not to be used when considering the fatigue truck; when assessing fatigue, one design truck is used, regardless of the number of design lanes. AASHTO's multiple presence factors are listed in Table 3.2.

Table 3.2: Multiple Presence Factors (AASHTO, 2020)

Number of Loaded Lanes	Multiple Presence Factors, *m*
1	1.20
2	1.00
3	0.85
>3	0.65

3.7 STRENGTH LIMIT STATE

Ensuring a bridge's resilience over its lifespan hinges on meeting the strength limit state, a pivotal guideline outlined in AASHTO (2020). This is particularly pertinent for box girders, extensively detailed in Article 6.11.6 and segmented into four key sections. These criteria ensure bridges can effectively withstand loads, factoring in material properties, structural configuration, and load distribution. They form part of comprehensive design principles, aiming to not only support current loads but also endure stress over time. The strength limit state is a critical component of bridge design, which ensures a safe, durable, and stable structure for users.

3.7.1 General Requirements

Article 6.11.6.2.2 of AASHTO LRFD BDS outlines requirements for sections in positive flexure. Sections qualify as compact if they meet the requirements of Article 6.11.2.3 and also satisfy specific steel grade, web slenderness, effective flange width, and ductility requirements are permitted to exceed the moment at first yield according to provisions of Article 6.10.7-Flexural Resistance-Composite Sections in Positive Flexure.

- The section is not horizontally curved.
- The section is straight, meaning it is without skew.
- The specified minimum yield strengths of the flanges and web do not exceed 70.0 ksi.
- The web is without longitudinal stiffeners and meets the cross-section proportion limit in AASHTO LRFD BDS Article 6.11.2.1.2.
- The section meets the special restrictions on the use of LLDFs for multiple box sections outlined in AASHTO LRFD BDS Article 6.11.2.3.
- The box flange is fully effective as specified in AASHTO LRFD BDS Article 6.11.1.1.
- The section satisfies the web slenderness limit:

	$\frac{2D_{cp}}{t_w} \leq 3.76\sqrt{\frac{E}{F_{yc}}}$	Eq. 3.19
Where:		

D_{cp} =	depth of the web in compression at the plastic moment determined as specified in Article D6.3.2 (in.)
t_w =	web thickness (in.)
E =	modulus of elasticity of steel (ksi)
F_{yc} =	specified minimum yield strength of the compression flange (ksi)

This article also states that compact sections shall satisfy the requirements of AASHTO LRFD BDS Article 6.11.7.1. Sections are considered noncompact and shall satisfy the requirements of Article 6.11.7.2.

Both compact and noncompact sections must meet the ductility requirement in Article 6.10.7.3.

	$D_p \leq 0.42D_t$	Eq. 3.20
Where:		
D_p =	distance from the top of the concrete deck to the neutral axis of the composite section at the plastic moment (in.)	
D_t =	total depth of the composite section (in.)	

3.7.2 Flexural Resistance of Composite Sections

3.7.2.1 Compact Sections

Compact sections are defined as composite sections in positive flexure satisfying specific steel grade, web slenderness, and ductility requirements that are capable of developing a nominal resistance exceeding the moment at first yield but not exceeding the plastic moment (AASHTO, 2020). Sections must fulfill specific criteria to deform under stress without fracturing. In compact sections, at the strength limit state, bending moments caused by applied loads must not exceed the product of a flexure resistance factor and the nominal flexural resistance, which are calculated differently based on beam support.

For compact sections in positive flexure at the strength limit state, the section shall satisfy the following provisions outlined in Article 6.11.7.1.1:

	$M_u \leq \phi_f M_n$	Eq. 3.21

Where:	
ϕ_f =	resistance factor for flexure specified in Article 6.5.4.2
M_n =	nominal flexural resistance of the section determined as specified in Article 6.11.7.1.2 (kip-in.)
M_u =	bending moment about the major axis of the cross-section due to the factored loads at the section under consideration (kip-in.)

The provisions in Article 6.10.7.1.2 state that the nominal flexural resistance of simply supported sections shall be computed as:

If $D_p \leq 0.1\ D_t$, then:

	$M_n = M_p$	Eq. 3.22

Otherwise:

	$M_n = M_p\left(1.07 - 0.7\frac{D_p}{D_t}\right)$	Eq. 3.23

Where:	
D_p =	distance from the top of the concrete deck to the neutral axis of the composite section at the plastic moment (in.)
D_t =	total depth of the composite section (in.)
M_n =	nominal flexural resistance of a section (kip-in.)
M_p =	plastic moment of the composite section determined in Article D6.1 (kip-in.)

The nominal flexural resistance in continuous span sections is limited by:

	$M_n \leq 1.3 R_h M_y$	Eq. 3.24

Where:	
M_n =	nominal flexural resistance of a section determined from Eq. 6.31 or 6.32, as applicable (kip-in.)
R_h =	hybrid girder factor determined as specified in Article 6.10.1.10.1
M_y =	yield moment determined as specified in Article D6.2 (kip-in.)

3.7.2.2 Noncompact Sections

Noncompact sections are composite sections in positive flexure for which the nominal resistance is not permitted to exceed the moment at first yield (AASHTO, 2020). For non-compact sections, longitudinal flange stress should not surpass the product of the resistance factor for flexure, and the nominal flexural resistance of the compression flange should be determined using specified parameters.

At the strength limit state, compression flanges shall satisfy the following:

	$f_{bu} \leq \phi_f F_{nc}$	Eq. 3.25
Where:		
ϕ_f =	resistance factor for flexure specified in Article 6.5.4.2	
f_{bu} =	flange stress calculated without consideration of flange lateral bending or longitudinal warping (ksi)	
F_{nc} =	nominal flexural resistance of the box flanges in compression as specified in Article 6.11.7.2.2 (ksi)	

It should be noted that the maximum longitudinal compressive stress in the concrete deck slab shall not exceed $0.6f'_c$. The nominal flexural resistance of the compression flanges of open tub sections is calculated by the following equation:

	$F_{nc} = R_b R_h F_{yc}$	Eq. 3.26
Where:		

F_{nc} =	nominal flexural resistance of box flanges in compression (ksi)
R_b =	web load shedding factor determined as specified in Article 6.10.1.10.2
R_h =	hybrid girder factor determined as specified in Article 6.10.1.10.1
F_{yc} =	specified minimum yield strength of the compression flange (ksi)

The nominal flexural resistance of the compression flanges of closed-box sections shall be taken as:

	$F_{nc} = R_b R_h F_{yc} \Delta$	Eq. 3.27
In which:		
	$\Delta = \sqrt{1 - 3\left(\frac{f_v}{F_{yc}}\right)^2}$	Eq. 3.28
	$f_v = \frac{T}{2A_O t_f}$	Eq. 3.29
Where:		
Δ =	reduction factor for the maximum stress in a box flange	
f_v =	St. Venant torsional shear stress in the flange due to the factored loads at the section under consideration (ksi)	
A_o =	enclosed area with the box section (in.^{2})	
T =	internal torque due to the factored loads (kip-in.)	

The tension flange, at the strength limit state, shall satisfy:

	$f_{bu} \leq \phi_f F_{nt}$	Eq. 3.30
Where:		
F_{nt} =	nominal flexural resistance of the tension flanges determined as specified in Article 6.11.7.2.2 (ksi)	

The nominal flexural resistance of the tension flange of tub and closed-box sections shall be taken as:

	$F_{nt} = R_h F_{yt} \Delta$	Eq. 3.31
In which:		
	$\Delta = \sqrt{1 - 3\left(\frac{f_v}{F_{yt}}\right)^2}$	Eq. 3.32
	$f_v = \frac{T}{2A_o t_f}$	Eq. 3.33
Where:		
F_{nt} =	nominal flexural resistance of box flanges in tension (ksi)	
F_{yt} =	specified minimum yield strength of the tension flange (ksi)	
Δ =	reduction factor for the maximum stress in a box flange	
f_v =	St. Venant torsional shear stress in the flange due to the factored loads at the section under consideration (ksi)	

3.7.3 Flexural Resistance of Noncomposite Sections

The following provisions that are outlined in Article 6.11.8 are applied to noncomposite sections:

At the strength limit state, sections in negative flexure with compression flanges shall satisfy the following Article 6.11.8.1.1 requirement for box flanges in compression:

	$f_{bu} \leq \phi_f F_{nc}$	Eq. 3.34
Where:		
ϕ_f =	resistance factor for flexure specified in Article 6.5.4.2	
f_{bu} =	longitudinal flange stress due to the factored loads at the section under consideration calculated without consideration of longitudinal warping (ksi)	

F_{nc} =	nominal flexural resistance of the flange determined as specified in Article 6.11.8.2 (ksi)

In Article 6.11.8.1.2 of the AASHTO LRFD BDS, at the strength limit state, continuously braced flanges in tension shall satisfy the following requirement:

	$f_{bu} \leq \phi_f F_{nt}$	Eq. 3.35

Where:	
ϕ_f =	resistance factor for flexure specified in Article 6.5.4.2
f_{bu} =	longitudinal flange stress at the section due to the factored loads at the section under consideration calculated without consideration of longitudinal warping (ksi)
F_{nt} =	nominal flexural resistance of the tension flange determined as specified in Article 6.11.8.3 (ksi)

The nominal flexural resistance of unstiffened compression flanges shall be determined by provisions set in Article 6.11.8.2.2:

	$F_{nc} = F_{cb}\sqrt{1 - \left(\frac{f_v}{\phi_v F_{cr}}\right)^2}$	Eq. 3.36

In which:	
F_{cb} =	nominal axial compression buckling resistance of the flange under compression alone calculated as follows (ksi)

If $\lambda_f \leq \lambda_p$, then:

	$F_{cb} = R_b R_h F_{yc} \Delta$	Eq. 3.37

If $\lambda_p < \lambda_f \leq \lambda_r$, then:

	$F_{cb} = R_b R_h F_{yc} \left[\Delta - \left(\Delta - \frac{\Delta - 0.3}{R_h}\right)\left(\frac{\lambda_f - \lambda_p}{\lambda_r - \lambda_p}\right)\right]$	Eq. 3.38

If $\lambda_f > \lambda_r$, then:

	$F_{cb} = \frac{0.9 E R_b k}{\lambda_f^2}$	Eq. 3.39

If $\lambda_f \leq 1.12\sqrt{\frac{Ek_s}{F_{yc}}}$, then:

	$F_{cv} = 0.58 F_{yc}$	Eq. 3.40

If $1.12\sqrt{\frac{Ek_s}{F_{yc}}} \leq \lambda_f \leq 1.40\sqrt{\frac{Ek_s}{F_{yc}}}$, then:

	$F_{cv} = \frac{0.65\sqrt{Ek_s}}{\lambda_f}$	Eq. 3.41

If $\lambda_f > 1.40\sqrt{\frac{Ek_s}{F_{yc}}}$, then:

	$F_{cv} = \frac{0.9 E k_s}{\lambda_f^2}$	Eq. 3.42

	$\lambda_f = \frac{b_{fc}}{t_{fc}}$	Eq. 3.43
	$\lambda_p = 0.57\sqrt{\frac{Ek}{F_{yc}\Delta}}$	Eq. 3.44

	$\lambda_r = 0.95\sqrt{\frac{Ek}{F_{yr}}}$	Eq. 3.45
	$\Delta = \sqrt{1 - 3\left(\frac{f_v}{F_{yc}}\right)^2}$	Eq. 3.46
	$f_v = \frac{T}{2A_O t_{fc}}$	Eq. 3.47
	$F_{yr} = (\Delta - 0.3)F_{yc}$	Eq. 3.48

Where:	
ϕ_v =	resistance factor for shear specified in Article 6.5.4.2
ϕ_f =	resistance factor for flexure specified in Article 6.5.4.2
F_{cv} =	nominal shear buckling resistance of the flange
λ_f =	slenderness ratio of the compression flange
λ_p =	limiting flange slenderness where the elastic buckling stress equals $R_b F_{yc}\Delta$
λ_r =	limiting flange slenderness where the elastic buckling stress equals $R_b F_{yr}$
Δ =	reduction factor for the maximum stress in a box flange
f_v =	St. Venant torsional shear stress in the flange to the factored loads at the section under consideration (ksi)
F_{yr} =	smaller of the compression flange stress at the onset of nominal yield, with consideration or residual stress effects, or the specified minimum yield strength of the web (ksi)
k =	plate-buckling coefficient for uniform normal stress = 4.0
k_s =	plate-buckling coefficient for shear stress = 5.34
b_{fc} =	compression flange width between webs (in.)
t_{fc} =	compression flange thickness (in.)

The flexural resistance of longitudinally stiffened flanges in compression is computed in a similar fashion, although the modifications are described in AASHTO LRFD BDS Article 6.11.8.2.3 and are as follows:

- *w* shall be substituted for b_{fc}
- The plate buckling coefficient for uniform stress, *k*, shall be taken as:
    - If *n* = 1, then:

	$k = \left(\frac{8I_s}{wt_{fc}^3}\right)^{\frac{1}{3}}$	Eq. 3.49

    - If *n* = 2, then:

	$k = \left(\frac{0.894I_s}{wt_{fc}^3}\right)^{\frac{1}{3}}$	Eq. 3.50
	$1.0 \leq k \leq 4.0$	

- The plate buckling coefficient for shear stress, k_s, shall be taken as:

	$k_s = \frac{5.34 + 2.84\left(\frac{I_s}{wt_{fc}^3}\right)^{\frac{1}{3}}}{(n+1)^2} \leq 5.34$	Eq. 3.51

Where:	
I_s =	moment of inertia of a single longitudinal flange stiffener about an axis parallel to the flange and taken at the base of the stiffener (in.^{4})
n =	number of equally spaced longitudinal flange stiffeners
w =	larger of the width of the flange between longitudinal flange stiffeners or the distance from a web to the nearest longitudinal flange stiffener (in.)

At the strength limit state, tension flanges shall satisfy the following:

	$f_{bu} \leq \phi_f F_{nt}$	Eq. 3.52

Where:	

ϕ_f =	resistance factor for flexure
f_{bu} =	flange stress calculated without consideration of flange lateral bending or longitudinal warping
F_{nt} =	nominal flexural resistance of box flanges in tension

The nominal flexural resistance of tub sections based on tension flange yielding, outlined in Article 6.11.8.3, shall be taken as:

	$F_{nt} = R_h F_{yt}$	Eq. 3.52
Where:		
R_h =	hybrid girder factor	
F_{yt} =	specified minimum yield strength of the tension flange	

3.8 AASHTO REFERENCES

Table 3.3: AASHTO LRFD BDS References (AASHTO, 2020) details a summary of the equations noted within this chapter. The referenced equation, table, or figure number is provided along with the corresponding page number from which the reference can be found in the 2020 9th edition of the AASHTO LRFD BDS.

Table 3.3: AASHTO LRFD BDS References (AASHTO, 2020)

Chapter 3	AASHTO LRFD BDS 9th Edition Reference	AASHTO LRFD BDS 9th Edition Page Number
Table 3.1	Table 3.5.1-1	3-21
Figure 3.1	Figure 3.6.1.2.2-1	3-25
Equation 3.1	Equation 1.3.2.1-1	1-3
Equation 3.2	Equation 6.11.2.1.2-1	6-222
Equation 3.3	Equation 6.11.2.1.3-1	6-222
Equation 3.4	Equation 6.11.2.2-1	6-222
Equation 3.5	Equation 6.11.2.2-2	6-222
Equation 3.6	Equation 6.11.2.2-3	6-222
Equation 3.7	Equation 6.10.3.2.1-1	6-160
Equation 3.8	Equation 6.10.3.2.1-2	6-160
Equation 3.9	Equation 6.10.3.2.1-3	6-160
Equation 3.10	Equation 6.10.3.2.2-1	6-162

Equation 3.11	Equation 6.10.3.2.3-1	6-162
Equation 3.12	Equation 6.11.3.2-1	6-224
Equation 3.13	Equation 6.11.3.2-2	6-224
Equation 3.14	Equation 6.11.3.2-3	6-224
Equation 3.15	Equation 6.11.3.2-4	6-224
Equation 3.16	Equation 6.11.3.2-5	6-225
Equation 3.17	Equation 6.10.3.3-1	6-163
Equation 3.18	Equation 6.11.9-1	6-238
Table 3.2	Table 3.6.1.2.2-1	3-23
Equation 3.19	Equation 6.11.6.2.2-1	6-230
Equation 3.20	Equation 6.10.7.3-1	6-182
Equation 3.21	Equation 6.11.7.1.1-1	6-231
Equation 3.22	Equation 6.10.7.1.2-1	6-179
Equation 3.23	Equation 6.10.7.1.2-2	6-179
Equation 3.24	Equation 6.10.7.1.2-3	6-179
Equation 3.25	Equation 6.11.7.2.1-1	6-231
Equation 3.26	Equation 6.11.7.2.2-2	6-232
Equation 3.27	Equation 6.11.7.2.2-3	6-232
Equation 3.28	Equation 6.11.7.2.2-4	6-232
Equation 3.29	Equation 6.11.7.2.1-2	6-232
Equation 3.30	Equation 6.11.7.2.2-5	6-233
Equation 3.31	Equation 6.11.7.2.2-6	6-233
Equation 3.32	Equation 6.11.7.2.2-7	6-233
Equation 3.33	Equation 6.11.8.1.1-1	6-233
Equation 3.34	Equation 6.11.8.1.2-4	6-234
Equation 3.35	Equation 6.11.8.2.2-1	6-235
Equation 3.36	Equation 6.11.8.2.2-2	6-235
Equation 3.37	Equation 6.11.8.2.2-3	6-235
Equation 3.38	Equation 6.11.8.2.2-4	6-235
Equation 3.39	Equation 6.11.8.2.2-5	6-235
Equation 3.40	Equation 6.11.8.2.2-6	6-236
Equation 3.41	Equation 6.11.8.2.2-7	6-236
Equation 3.42	Equation 6.11.8.2.2-8	6-236
Equation 3.43	Equation 6.11.8.2.2-9	6-236
Equation 3.44	Equation 6.11.8.2.2-10	6-236
Equation 3.45	Equation 6.11.8.2.2-11	6-236
Equation 3.46	Equation 6.11.8.2.2-12	6-236
Equation 3.47	Equation 6.11.8.2.2-13	6-236
Equation 3.48	Equation 6.11.8.2.3-1	6-237
Equation 3.49	Equation 6.11.8.2.3-2	6-237
Equation 3.50	Equation 6.11.8.2.3-3	6-237
Equation 3.51	Equation 6.11.8.1.2-4	6-234
Equation 3.52	Equation 6.11.8.3-1	6-238

3.9 CONCLUSION

This chapter summarized the applicable articles and equations from the 9th Edition of the AASHTO LRFD BDS related to PBFTGs. As PBFTGs are a relatively new system, specifications directly relating to them do not exist in the AASHTO LRFD BDS. The system was designed using the applicable articles found in AASHTO LRFD BDS Article 6.11 as they relate to large, welded box girders. However, several sections are not applicable to the design of most PBFTG bridges, such as the limit of skew on the compactness and, therefore, the ultimate capacity of PBFTGs, which is the primary focus of this research study, as it dramatically reduces the applicability of PBFTGs in skewed bridge configurations. Based on the findings of this chapter, a more enhanced analysis was performed on PBFTGs with the focus of improving the AASHTO LRFD BDS to expand the applicability and competitiveness of PBFTGs.

CHAPTER 4: BACKGROUND EXPERIMENTAL STUDY

4.1 INTRODUCTION

This chapter contains an overview of a prior laboratory experiment where five reduced-scale concrete bridge decks were fabricated and tested to assess the behavior of concrete bridge decks with varied skews and testing parameters. The overview discusses the test procedure, the specimen fabrication process, the equipment used, and the results of the testing efforts. The efforts of this study helped determine the most efficient experimental and analytical testing plan for the PBFTG. Analytical modeling techniques were employed to serve as a benchmark against the laboratory data and further verify this methodology's use in **Error! Reference source not found.**

4.2 OVERVIEW OF SKEWED DECK PANEL TESTING

Physical laboratory flexural testing was conducted at West Virginia University (WVU) in the Major Units Laboratory to assess the performance and capacity of simulated non-composite low-skew reinforced concrete bridge deck slabs. Physical testing is also used to verify the accuracy of the analytical modeling procedure and results. Flexural capacity testing was conducted on five separate simply-supported “Pinned-Pinned” concrete bridge deck slab experiments in three-point bending. The typical test setup is shown in Figure 4.1.

Figure 4.1: View of Test Setup

Steel bearing plates prefabricated with a 2-inch-diameter round bar welded to the plates were used as beam supports placed atop trapezoidal concrete abutments to simulate the simply-supported boundary conditions. Flexural testing was conducted inside a steel structural reaction testing frame bolted into the laboratory's strong floor.

4.3 SPECIMEN DESCRIPTIONS

Five specimens were fabricated and tested in the Major Units Laboratory at West Virginia University for this research effort:

- Experiment 1 consisted of a rectangular reinforced concrete bridge slab with zero degrees of skew.

- The specimens tested in Experiments 2 and 3 were reinforced concrete bridge slabs with 10 degrees of skew. Specimen 2 was tested with the load applied perpendicular to the longitudinal reinforcement. Specimen 3 was tested with the load applied in the direction of skew.
- Experiments 4 and 5 tested a reinforced concrete bridge slab specimen with 20 degrees of skew. As stated above, the same loading pattern was followed for Experiments 4 and 5.

4.3.1 Specimen Dimensions and Reinforcement Design

Each specimen was a 30” × 8” × 78” slab with the varied skews listed above. Standard #4 and #5 reinforcement bars were used in each specimen. The reinforcement pattern of each experiment was designed according to AASHTO LRFD BDS Article 9.7 (AASHTO, 2017). Article 9.7.1.3 of the code on skewed concrete deck slabs states:

> If the skew angle of the deck does not exceed 25 degrees, the primary reinforcement may be placed in the direction of the skew; it shall be placed perpendicular to the main supporting components (AASHTO, 2017).

Primary reinforcement or transverse reinforcement (detailed in Figure 4.2) is said to be placed parallel to the skew only at low skews to prevent extensive cracking of the deck caused by the lack of reinforcement acting in the direction of principal flexural stresses due to significantly skewed reinforcement (AASHTO, 2017).

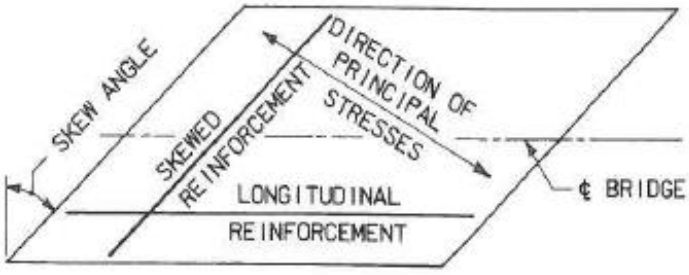

Figure 4.2: Skewed Decks Reinforcement Layout (AASHTO, 2017)

The transverse reinforcement bars were intermittently sized, between bars with 1-inch cover and bars extending outside the deck by 2 inches on either side. This design was intended to place the reinforcement bars accurately while mainly allowing wired connection access to uniaxial gauges housed inside the concrete slabs on the longitudinal reinforcement bars. Detailed cross-sectional and plan view reinforcement patterns are shown in

Figure 4.3, Figure 4.4, Figure 4.5, and Figure 4.6. Skews with multiple experimental specimens (Experiments 2 and 3) and (Experiments 4 and 5) have the same reinforcement patterns.

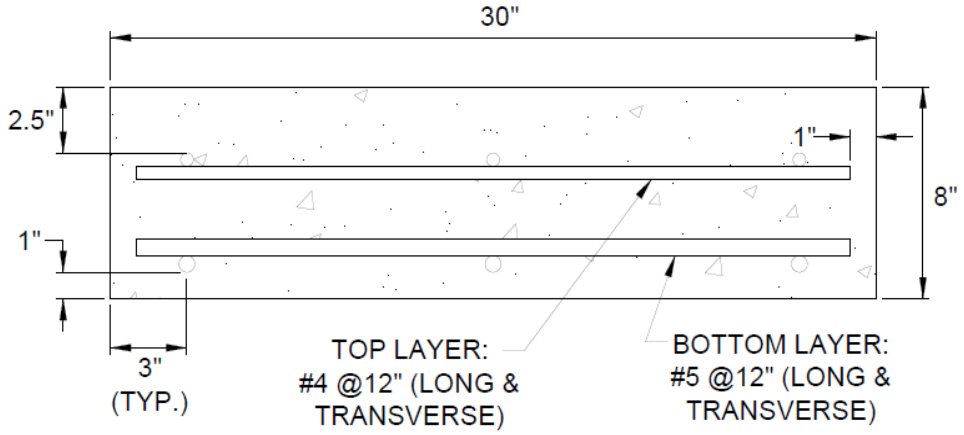

Figure 4.3: Cross-Sectional View of Typical Deck Reinforcement Pattern

Figure 4.4: Plan View of 0-Degree Deck Reinforcement Pattern

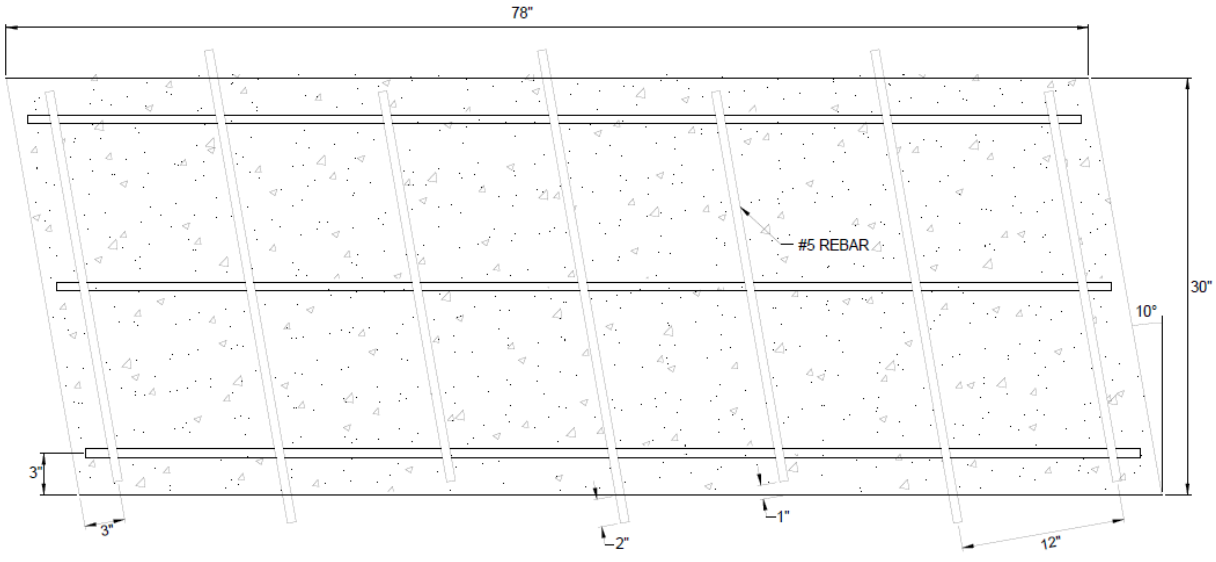

Figure 4.5: Plan View of 10º Deck Reinforcement Pattern

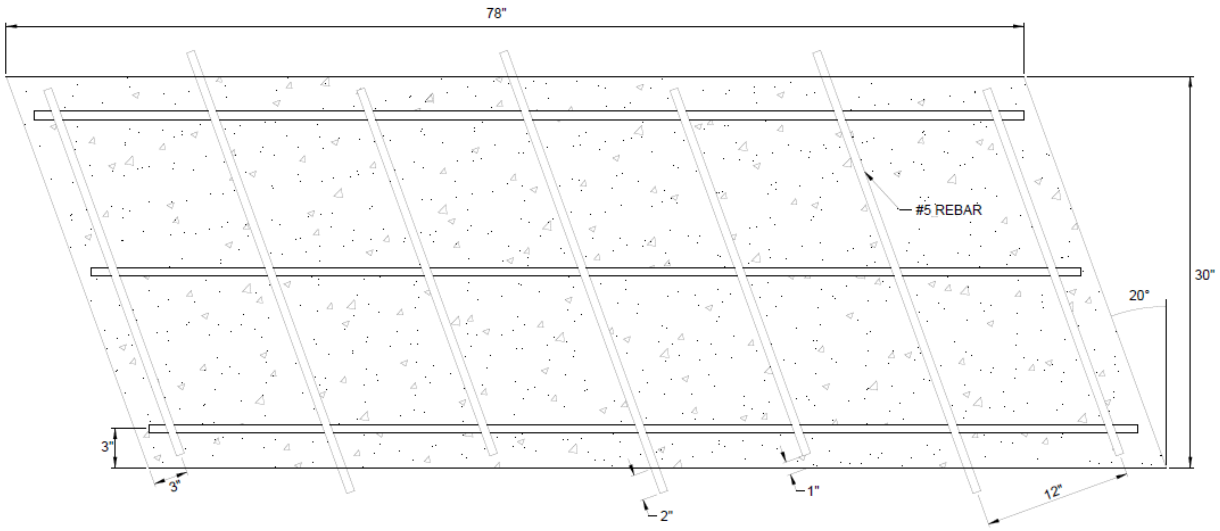

Figure 4.6: Plan View of 20º Deck Reinforcement Pattern

4.4 Deck Specimen Assembly and Casting

After the design of the specimens was determined, physical assembly started with the construction of the five-deck forms. This section describes constructing the forms, preparing them for casting, and the concrete pour.

4.4.1 Exterior Formwork

The deck slabs were constructed using a combination of OSB plywood and 2" × 4" wood board. 9/16" and 11/16" diameter holes were drilled into the longitudinal sides of the forms to allow the necessary reinforcement bars and gauging wires to extend outside each deck. Waterproof caulk and spray foam insulation was used to seal any minor gaps in the formwork.

4.4.2 Reinforcement

Reinforcement bars were installed at the necessary locations using rebar ties. The intermittent extended rebar assisted in ensuring accurate placement of the bar as they could rest in the holes and act as a guide for the rest of the bar. Having longer reinforcement bars that could rest

in the form at the particular design placement meant rebar chairs were not needed for this endeavor. The bars could be tied together and held up by the extended bars. Additional “hooks” were made with #4 rebar using a rebar bender and installed to serve as a lifting connection, which allowed the decks to be transported and installed into the testing frame using the laboratory’s overhead crane.

4.4.3 Specimen Concrete Casting

Before testing, hydraulic oil was applied only to the wood parts of the formwork to act as a form release to ease demolding efforts. West Virginia Division of Highways (WVDOH) Class K/7 6.5 ksi concrete was used to fabricate the test deck slabs. The concrete slabs were cast in place (see Figure 4.7) at the Major Units Lab according to the conditions outlined in Article 9.7.2.4 of AASHTO LRFD BDS (AASHTO, 2020). A concrete vibrator was used to remove air voids from the concrete before finishing tools leveled the top surface of the specimens. The deck slabs were allowed to water-cure with the help of burlap sheets for 28 days before flexural testing.

Figure 4.7: Process of Pouring Concrete Specimens

4.5 INSTRUMENTATION

This section discusses the instruments used to collect data during flexural testing.

4.5.1 Instruments

The load was applied and determined using an MTS Model 243.40 110-kip servo-hydraulic actuator. The servo-hydraulic actuator is equipped with a load cell that measures the magnitude of loading and a linear variable displacement transducer (LVDT) housed within that measures the vertical deflection of the specimen at the point of loading ± 6 inches. Additional data was collected from Micro-Measurements foil-resistor uniaxial strain gauges installed on the longitudinal reinforcement bars and cast within each specimen. The strain gauges were wire-connected to a Micro-Measurements Model 5100 Scanner operating StrainSmart Version 4.72 software to record strain and displacement values.

4.5.2 Instrumentation Plan

A total of six strain gauges per specimen were employed during capacity testing to collect strain and displacement data. Strain gauges were installed 18 inches from either end of the bottom longitudinal reinforcement bars and encased in the concrete. The gauges were soldered with wire that extended outside the specimen through holes in the forms for transverse reinforcement bars to extend. The typical gauging pattern can be seen in

Figure 4.8 below.

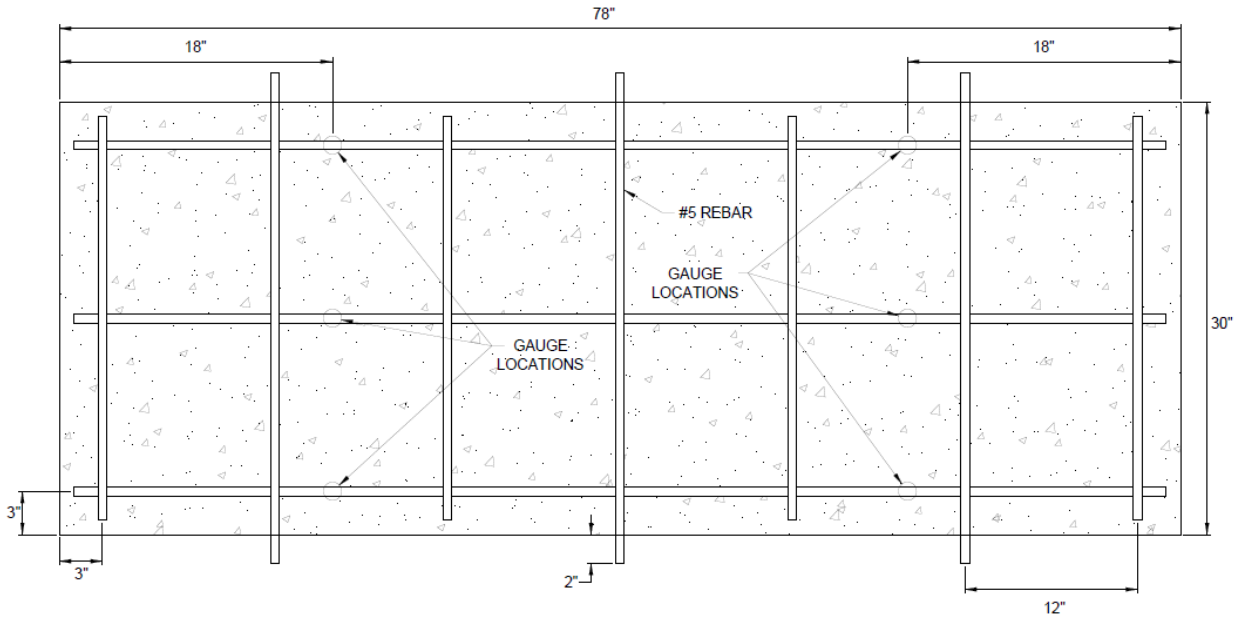

Figure 4.8: Typical Strain Gauge Layout

Since the strain gauges were to be encased and exposed to concrete, Micro-Measurements M-Coat JA-1 Polysulfide Coating was generously applied to the surrounding area of the strain gauges to provide additional protection. All strain gauges were tested for accuracy multiple times before connection using a multimeter to verify that each gauge had a grid resistance of 350 ± 0.5% ohms as per the Micro-Measurements instrumentation specifications (Micro-Measurements, 2023).

4.6 Material Testing

Concrete samples were tested to determine the material properties of the delivered concrete to be applied during the three-dimensional finite element modeling to ensure accuracy during comparison.

Twelve concrete cylinders were cast simultaneously as the five-deck slab castings. The cylinders were demolded from the plastic molds 48 hours after casting and wet-cured for 28 days before undergoing compressive strength testing. Each cylinder was weighed on a digital scale before compressive testing to determine the weight in pounds. Cylinders were compressed until failure using a compressive concrete testing machine, which records the strength of each specimen. The compressive strengths obtained from each were averaged together to obtain an average compressive strength of 6.5 ksi, which was then used when producing the analytical model of each deck slab specimen.

4.7 Flexural Testing

Once the supports were configured at the correct skew and the 110-kip servo-hydraulic actuator was installed, each specimen was placed into the testing frame individually. Strain gauges were wired to record measurements as each specimen was loaded until failure was reached. Readings from the load cell and LVDT within the servo-hydraulic actuator and from the strain gauges were recorded during the entire testing period.

4.7.1 Testing Procedure

As previously stated, the load was applied at midspan by an MTS Model 243.40 110-kip servo-hydraulic actuator that was mounted to a steel structural reaction frame. The actuator utilizes MTS TestStar™ Version 3.4B 1459 software, which controls the load and displacement applied. The load was applied to each specimen through a steel spreader beam on top of an elastomeric pad to reduce the bearing effects. The direction of load was varied at each skew by the placement of the spreader beam. Experiments 1, 2, and 4 were loaded with the spreader beam placed perpendicularly to the longitudinal reinforcement bars. Experiments 3 and 5 were tested with the spreader beam placed in the direction of the skew to allow the load to be applied parallel to the transverse reinforcement bars.

The testing procedure used for this research effort is modeled closely after the procedure used for previous laboratory flexural testing performed at WVU (Michaelson, 2014). Each specimen was loaded in the stroke control to collect accurate data safely. Pseudo-static step loading was utilized by loading the specimen in 0.10-inch increments. The load was allowed to stabilize and distribute through the spreader beam for 2 minutes before the displacement, load, and five strain gauge readings were recorded. After measurements were documented, the next load step was applied, and the process was repeated. The displacement step increment was increased to 0.20 inches as the load vs. deflection graph stabilized. This process was followed until each specimen reached failure. Failure is determined after the load consistently declines after continuous increases in displacement.

4.8 RESULTS

This section analyzes the effect loading direction and skew have on the flexural capacity of each test specimen. An overview of the verification between the laboratory and analytical testing results is provided to display the accuracy of testing and modeling techniques.

The following results include only data collected during experimental testing. It should be noted that the actuator used during testing was not calibrated accurately at the time of testing. Furthermore, a vertical deflection calibration was performed using the actuator LVDT and a BDI LVDT to compare the data collected. Further calibration options are currently being explored to

address this issue. The results presented below are intended to present only a compassion of load/deflection curve shape.

4.8.1 0° Skew

Experiment 1 was tested with the load applied perpendicular to the longitudinal reinforcement bars. Figure 4.9 shows the midspan load-deflection results for the test specimen with a design with zero skew degrees.

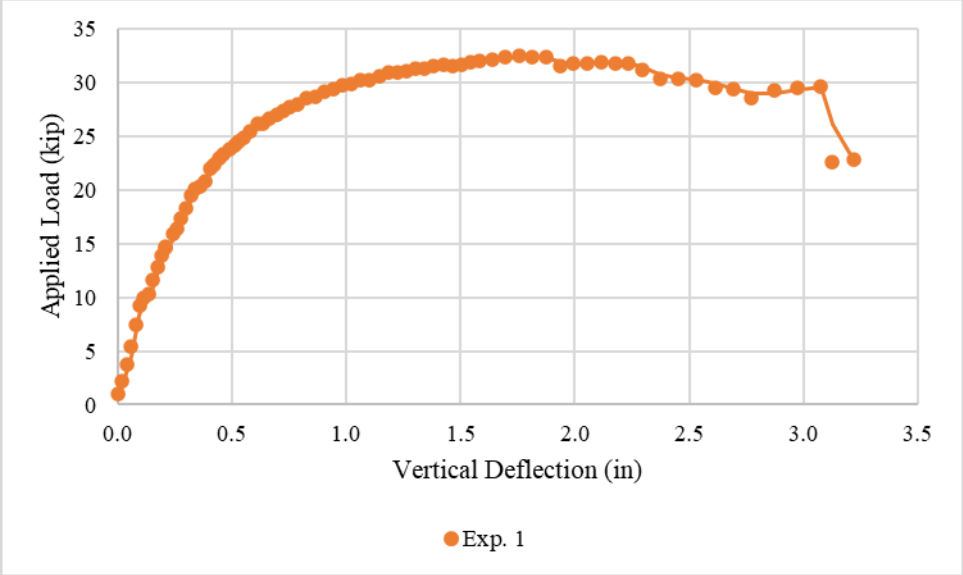

Figure 4.9: Load-Deflection Data from Flexural Testing of Specimens Skewed 0°

4.8.2 10° Skew

Experiments 2 and 3 were designed with 10 degrees of skew. Experiment 2 was tested with the load applied perpendicular to the longitudinal reinforcement bars, while Experiment 3 had the load applied parallel to the skew direction. Figure 4.10 shows the midspan load-deflection results for each test specimen.

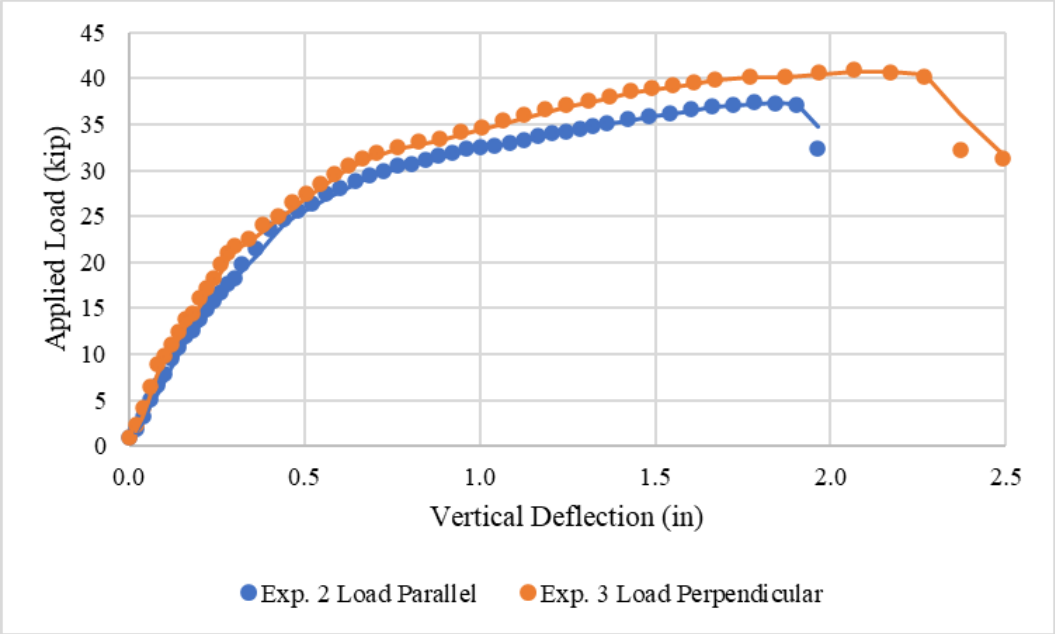

Figure 4.10: Load-Deflection Data from Flexural Testing of Specimens Skewed 10°

Both specimens displayed similarly shaped load-displacement curves, although flexural resistance appears to be slightly more significant when the load is applied perpendicular to the longitudinal centerline. However, the difference in capacity is minimal, so it was assumed that the difference in flexural capacity is negligible.

4.8.3 20° Skew

The test deck slab specimens with 20 degrees of skew were tested in the same manner as the two 10-degree skew specimens. Experiment 4 was tested with the load applied perpendicular to the longitudinal reinforcement bars, while the load was applied parallel to the skew direction in Experiment 5. Figure 4.11 shows the midspan load-deflection results for each test specimen.

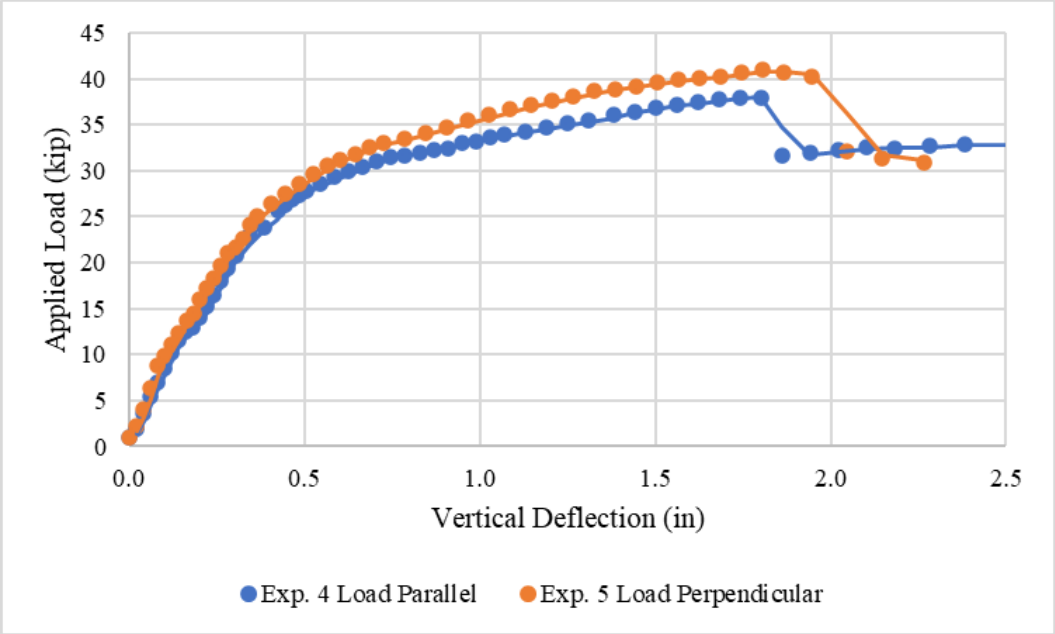

Figure 4.11: Load-Deflection Data from Flexural Testing of Specimens Skewed 20°

The test specimens displayed similarly shaped load-displacement curves that behaved similarly to the specimens that were skewed 10 degrees. Experiments 2 through 5 show to have a capacity greater than that of the straight deck slab.

4.9 Conclusion

The load-deflection plots show negligible differences in the ultimate capacity between 10 and degree specimens. Since all plots have similarly shaped load-deflection curves and the skewed specimens show to be behaving with greater flexural capacities, it can be assumed that there is no reduction in ultimate capacity due to skewness. Since there is a known calibration error, these results can only be taken as assumptions until further investigation is concluded.

CHAPTER 5: EXPERIMENTAL STUDY TECHNIQUES

5.1 INTRODUCTION

This chapter contains an overview of the physical laboratory methodologies used to complete testing on two composite 15º Valmont® U-BEAM™ shallow steel tub girders to evaluate the flexural capacity. A brief discussion of the composite test specimens and an overview of the background experiments that helped determine the assembly methodologies, instrumentation, and flexural testing procedure are provided.

5.2 OVERVIEW OF TESTING PROGRAM

Physical laboratory flexural testing was conducted in the Major Units Laboratory at WVU to verify the performance and capacity of two low-skewed PBFTGs. Physical testing will be used to verify the accuracy of the analytical modeling procedure and results. Flexural capacity testing was conducted on two specimens, both simply-supported composite PBFTGs provided by Valmont Industries, Inc., in three-point bending, similar to what is shown in Figure 5.1 and Figure 5.2.

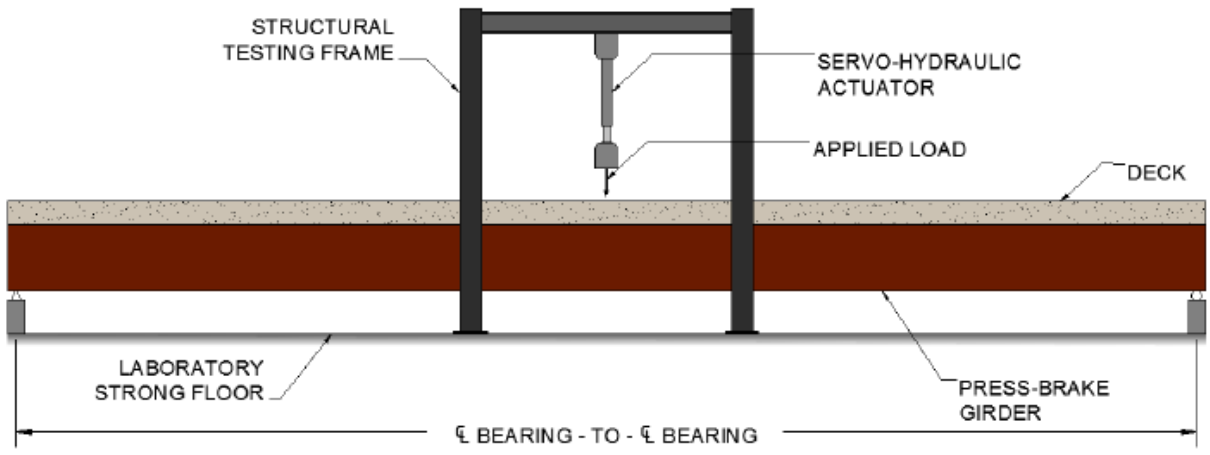

Figure 5.1: Typical Test Setup Schematic (Michaelson, 2014)

Figure 5.2: Isometric View of Definite Test Setup

To simulate the simply supported boundary conditions, prefabricated bearing plates with a 2-inch-diameter round bar were used as beam supports. The fabricated supports were placed directly under each bearing stiffener. This testing setup has been used for similar testing performed at WVU, such as (Michaelson, 2014) and (Tennant, 2022). As noted in Figure 5.1, the tub girder was supported by simulated “pinned” and “roller” boundary conditions. The “pinned” support was simulated using a bearing plate that was fabricated with the round bar welded to the center of the bearing plate, whereas the “roller” boundary condition was simulated by a bearing plate fabricated with a minor groove, allowing the round bar to rotate freely, and a thin metal plate longitudinally welded to either edge, as a measure of safety to prevent the round bar from displacing off the bearing plate (shown in Figure 5.3).

(a) ***(b)***

Figure 5.3: View of the Fabricated Supports, (a) "Pinned," (b) "Roller."

5.3 SPECIMEN DESCRIPTIONS

Two specimens were tested for this research experiment. Michaelson (2014) proposed a set of standardized cross-section geometries for standard mill plate thicknesses and widths and has since contributed to the use and evolution of PBFTGs. Valmont Industries, Inc. has since built a manufacturing facility in Fleetwood, Tennessee, dedicated to fabricating shallow steel press-break-formed tub girders (their trademarked "UBEAM™"). Valmont uses a 60-foot-long single length press brake to cold-bend a single M270 Grade 50 plate into the desired UBEAM™ shape. AASHTO LRFD 11.4.3.3.2 requires a minimum 5t bend radius, which prevents fracturing the plate and allows for Category A fatigue detail.

The next step in the manufacturing process is welding stiffeners, such as angle braces and diaphragms. Shear studs are also used to ensure composite action between the tub girder and the concrete deck slab. Furthermore, the test specimens used in this experiment have a similar design and dimensions, including five angle braces welded 6-feet from the center of the girder, perpendicular to the length. Bearing stiffener diaphragms were welded, parallel to the skew and 3-inches from the girder edge, at either end of the specimen. Typical cross sections are detailed in Figure 5.4.

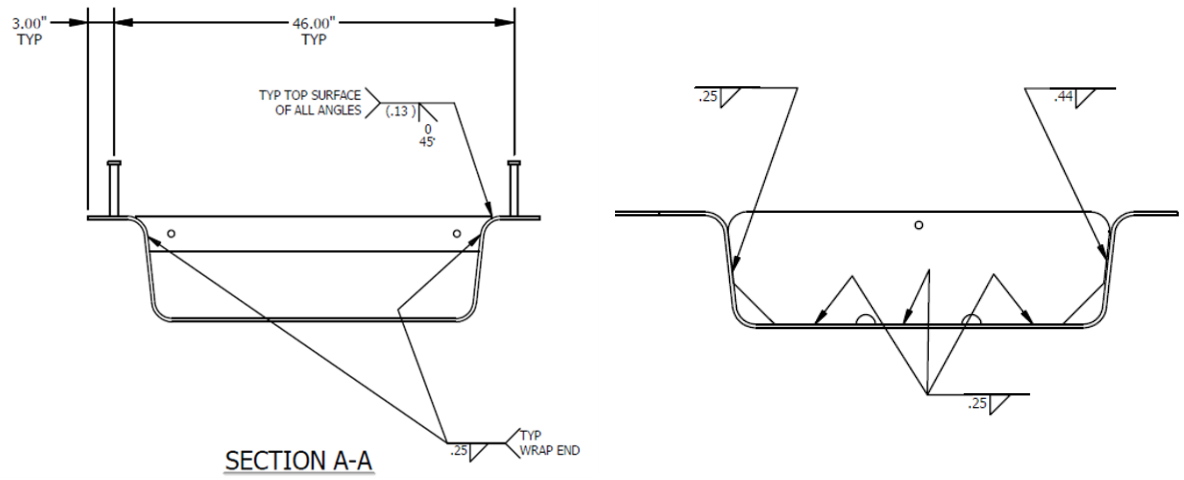

(a) ***(b)***

Figure 5.4: Typical Cross-Sections, (a) Angle Bracing, (b) Bearing Diaphragm (Valmont, 2024a)

Shear studs were welded using a programmed mechanical welder, Valmont's "Stud Gun" (seen in Figure 5.5), which allows excellent accuracy in the spacing and plumbness of the shear studs. Shear studs are essential in composite tub sections as they ensure there is composite action between the concrete deck and the tub girder. One row of shear studs was used on both the U12 and U18 specimen. Figure 5.6 dimensions the studs used in more detail. It should also be noted that the shear studs were spaced 6-inches apart center to center longitudinally on the top flanges for both girders to satisfy requirements of the AASHTO/AWS D1.5M/D1.5 Bridge Welding Code. (Valmont, 2023).

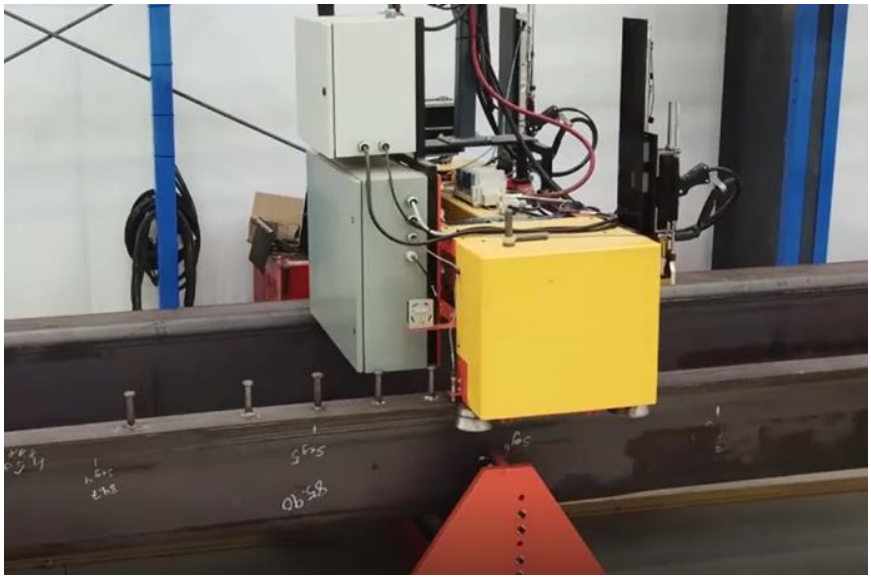

Figure 5.5: Valmont "Stud Gun" Automated Welding Machine (O'Riorden, 2023)

Note. The figure was provided by the manufacturer. Reprinted with permission.

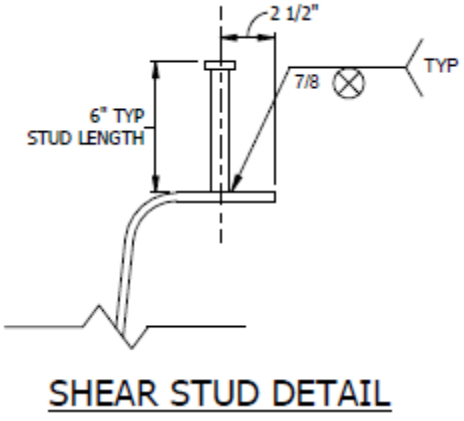

Figure 5.6: Typical Shear Stud Detailed Dimensions (Valmont, 2023)

Lastly, Valmont's girder can be galvanized or made of weathering steel. A galvanizing bath is used to hot dip the UBEAMS at once, which contributes to their efficient and fast manufacturing process. In this study, the first specimen tested was a 30-foot centerline hot-dipped galvanized Valmont "U18" tub girder, while the second specimen was a 28-foot centerline Valmont "U12" tub girder made of weathering steel.

5.3.1 U18 Specimen

The first PBFTG tested in this experiment was a Valmont “U18” tub girder. Valmont denotes their U-BEAM™ by depth, meaning a U18 girder has a total height of 18-inches. This girder was fabricated from an 80 3/4” × 3/8” × 373 15/16” steel plate. A dimensioned cross-sectional view of a typical Valmont “U18” tub girder is shown in Figure 5.7. Typical section properties and plate information for a common U18 are described in

Table 5.1 and Table 5.2.

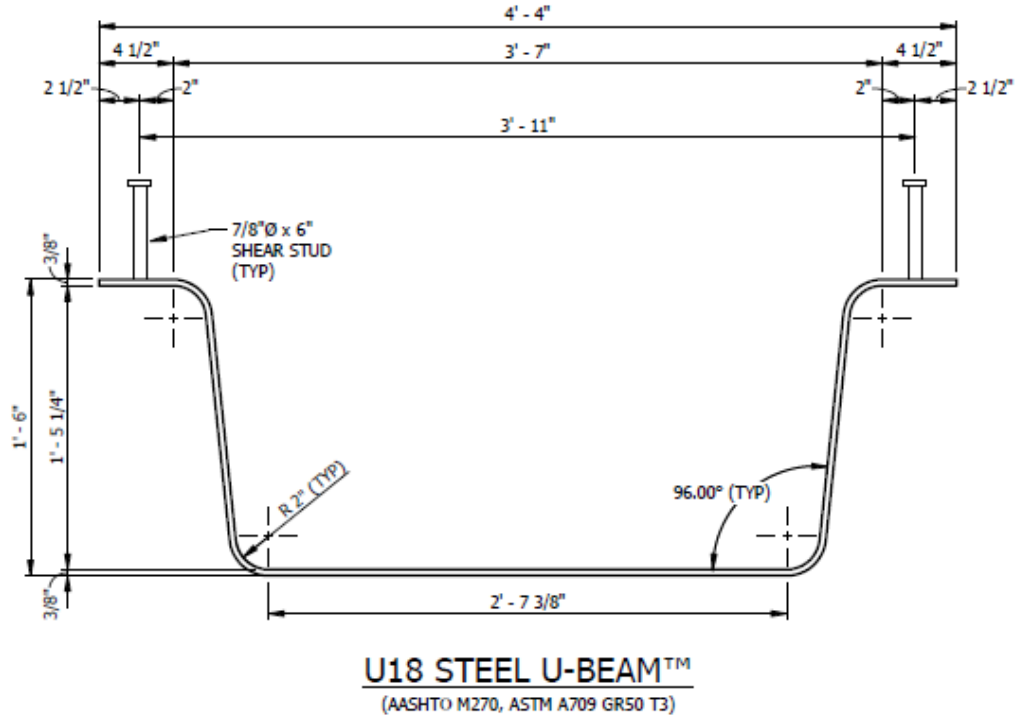

Figure 5.7: Typical Non-Composite "U18" Cross-Section Dimensions (Valmont, 2023)

Table 5.1: Typical "U18" Non-Composite Section Properties (Valmont, 2023)

U18			
NON-COMPOSITE SECTION PROPERTIES			
I_{steel}	S_{steel_top}	S_{steel_bottom}	J
in^4	in^3	in^2	in^4
1475.69	-128.98	224.99	1.70

Table 5.2: Typical "U18" Plate Information (Valmont, 2023)

PLATE INFORMATION			
t_{steel}	L_{steel}	A_{steel}	ω_{steel}
in	in	in^2	plf
3/8	80 3/4	30.29	104

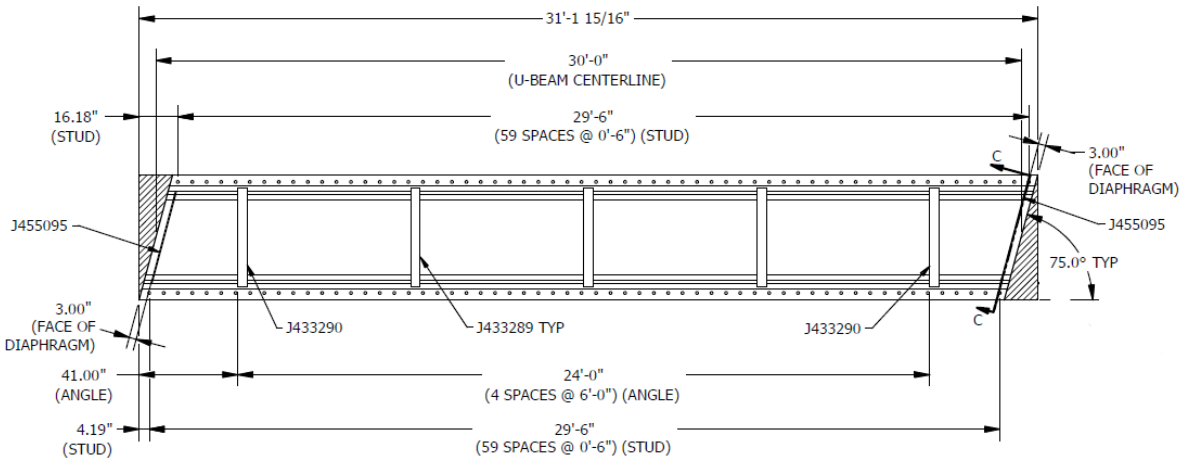

Figure 5.8: Isometric Plan View of the U18 Test Specimen

Note. The figure was provided by the manufacturer. Reprinted with permission.

5.3.2 U12 Specimen

A 15-degree Valmont "U12" tub girder underwent destructive testing second. A dimensioned cross-sectional view of a typical Valmont "U12" tub girder is shown in Figure 5.9. Valmont's U12 and U18 beams are the exact dimensions in width, although the angle of the bends and the slope dimensions change as the height is increased between UBEAMs™. This PBFTG was fabricated from a 70" × 3/8" × 349 15/16" steel plate as detailed in Table 5.4. Typical section properties of a non-composite U12 PBFTG are listed in Table 5.3. Complete dimensions of the 28-foot U12 are shown in Figure 5.10.

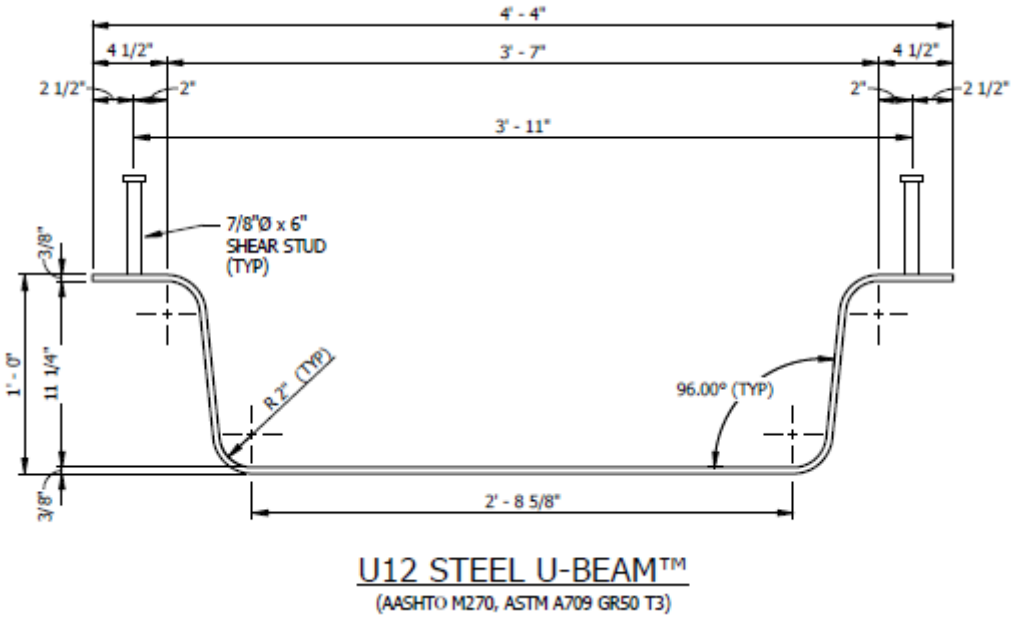

Figure 5.9: Typical Non-Composite "U12" Cross-Section Dimensions (Valmont, 2023)

Table 5.3: Typical "U12" Non-Composite Section Properties (Valmont, 2023)

U12			
NON-COMPOSITE SECTION PROPERTIES			
I_{steel}	S_{steel_top}	S_{steel_bottom}	J
in^4	in^3	in^2	in^4
582.74	-73.18	144.35	1.34

Table 5.4: Typical "U12" Plate Information (Valmont, 2023)

PLATE INFORMATION			
t_{steel}	L_{steel}	A_{steel}	ω_{steel}
in	in	in^2	plf
3/8	70	26.23	90

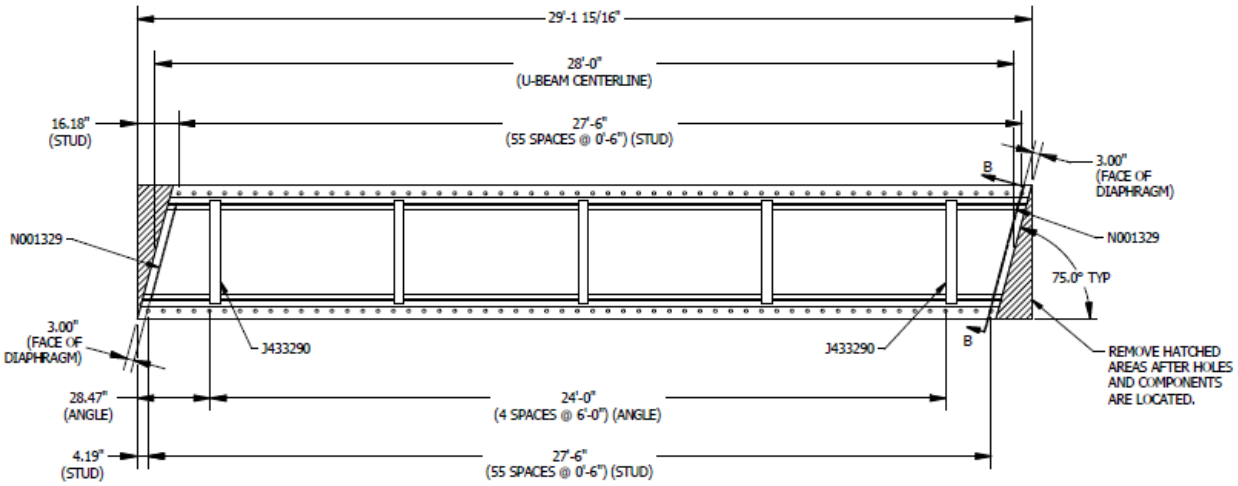

Figure 5.10: Isometric Plan View of the U12 Test Specimen

Note. The figure was provided by the manufacturer. Reprinted with permission.

5.4 Test Specimen Assembly

This section provides a chronological overview of the assembly techniques and processes for installing the composite units, casting the deck slab, and preparing the specimen for flexural testing.

5.4.1 SIP Metal Formwork

Stay-in-place (SIP) corrugated metal formwork was utilized between the top flanges of the tub girder (as shown in Figure 5.11). The SIP metal deck panels utilized in this research effort

covered the length of the beam from bearing to bearing and were 45" wide by 2" tall. Each SIP panel was secured to the specimen using self-tapping screws to safeguard composite action between the concrete deck and steel components occurred. The decking panels fit securely in between the 7/8-inch diameter shear studs on either flange, ensuring the 1-inch minimum cover was met on all supports (Valmont, 2023).

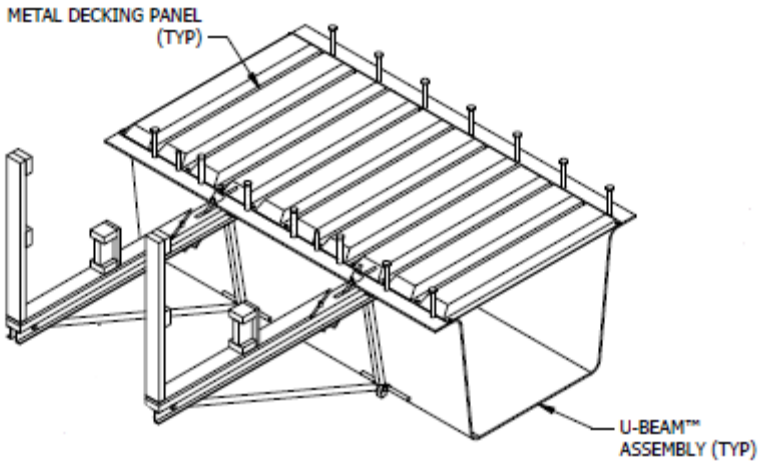

Figure 5.11: Isometric View of Typical SIP and Overhang Bracket Configuration (Valmont, 2023)

5.4.2 Exterior Formwork

The exterior formwork could be installed once the SIP formwork was mounted on the specimen. The exterior formwork used for this research effort consisted of two components: the wood formwork, which was used to cast the deck, and overhang brackets, which were used to form the deck from the air while in place. This methodology is a commonly used practice in bridge construction when casting a deck in the field.

The exterior formwork was constructed similarly to the formwork used for the deck tests discussed in Chapter 4: . The formwork was designed with efficiency and optimism in mind. The wooden sides were designed to consist of four 8-foot sections that are spliced together using two 2” × 4” × 2’ pieces that fit tight inside the formwork, as seen in Figure 5.12. This allows the forms to be used for future use on various length test specimens, with the ability to extend or shorten the formwork if a specimen is longer or shorter than 32 feet. The multi-section sides were also

designed for easy installation and removal. All sides were formed into a frame made of 2” × 4” sections with 5” vertical pieces spaced 1’ to 2’ apart. Sheets of 23/32” plywood were cut down into 8” × 8’ strips to be used for the side backs and 8 ¼” × 8’ strips used to cast the underside of the deck and support the weight of the concrete while the deck was hardening. The 8-inch-wide plywood strips were screwed to the face of the frames before they were then connected to the base. The end forms were constructed using the same methods and were skewed to fit the proper dimensions, as shown in Figure 5.13.

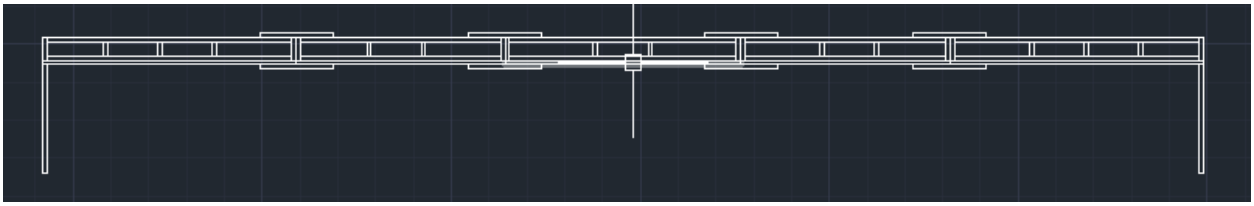

Figure 5.12: Longitudinal Wooden Formwork Design

Figure 5.13: Skewed Wooden Formwork Design

The first step in assembling the exterior formwork was welding the half hangers to the test specimen. The half hangers consist of a 0.45-inch diameter steel bar welded to each specimen using 5/16” tack welds performed by West Virginia University’s Lane Innovation Hub. The end of the half hangers were positioned 4 inches from the edge of the flanges, according to Figure 5.14.

Half hangers were spaced 1.5 feet on either side of the specimen's longitudinal centerline and then spaced every 3 feet until the length of the tub girder was achieved (Figure 5.15). Half hangers that would cause their overhang bracket to interfere with the structural testing frame were repositioned (up to 6 inches away from the initially planned placement) to the center of the adjacent shear studs where the overhang bracket would be clear of obstructions.

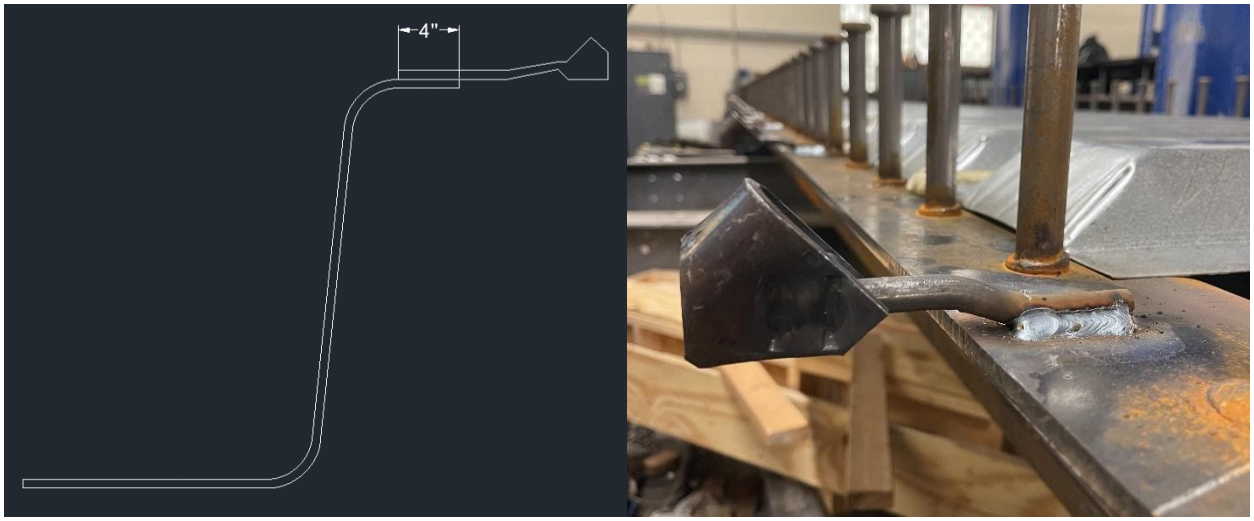

Figure 5.14: Half Hanger Transverse Welding Layout

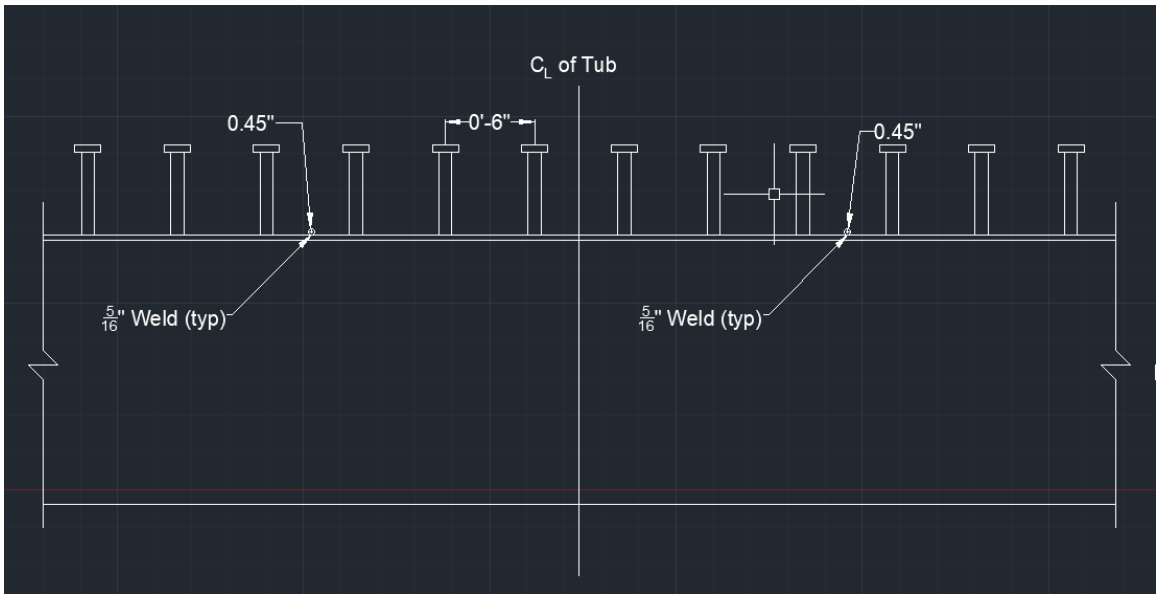

Figure 5.15: Half Hanger Longitudinal Welding Layout

Following the construction of the wooden formwork and the welding of the half hangers, the deck formwork could be assembled using the overhang brackets. Holes were marked and drilled in the base of the wooden forms for the threaded rod to extend through the exterior formwork and the half hanger (shown in more detail in Figure 5.16). The overhang brackets were adjusted to fit the test specimen before the hangers were tightened and leveled. Figure 5.17 shows overhang brackets after installation.

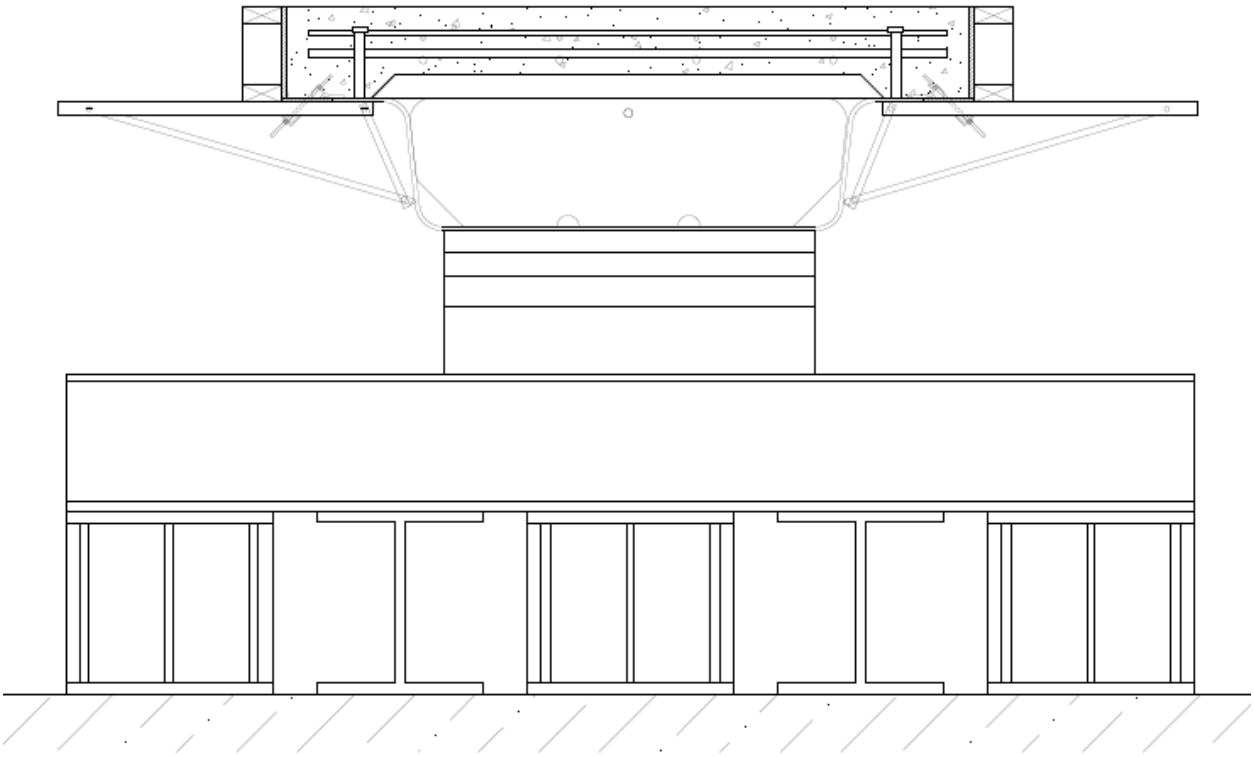

Figure 5.16: Cross-Sectional view of the Half-Hanger and Overhang Bracket Installation

Figure 5.17: Half hanger and Overhang Bracket after Installation

Spray foam and waterproof silicone caulk were used to fill any minor gaps in the formwork, ensuring a tight seal between the wooden formwork and the tub girder.

5.4.3 Reinforcement

Following the installation of the exterior formwork, reinforcement bars could be placed. The reinforcement pattern (Figure 5.18) was designed to resemble Michaelson's (2014) reinforcement pattern to ensure consistency and accuracy for comparison. Reinforcement was determined following the empirical deck design method detailed in Article 9.7.2 of AASHTO LRFD BDS (AASHTO, 2017). The concrete deck was designed to be 8-inches thick and 60 inches wide, which extended 4-inches from either top flange. The deck had a 2-inch haunch created by the SIP metal formwork, with two layers of transverse rebar placed on top of the longitudinal rebar. The bottom layer of reinforcement consisted of standard #5 rebar. Three bars were used for the longitudinal reinforcement, two 20-foot bars and one center 82-inch-long bar to achieve the length needed for the beam, with a development length of 24-inches designed according to AASHTO LRFD BDS. The longitudinal rebar was designed to have 2-inches of clear cover and was spaced

12 inches on center. 1-inch rebar chairs were used to obtain the necessary clear cover. The bottom layer of transverse reinforcement was 58-inches in length and skewed 15 degrees (according to Article 9.7.1.3 of AASHTO LRFD BDS as previously discussed in 4.3.1). Transverse rebar was spaced 12 inches apart and placed directly on top of the bottom longitudinal rebar.

The top layer of reinforcement utilized #4 rebar for the transverse and longitudinal reinforcement. The exact spacing and dimensions as the bottom layer reinforcement layer were used. The top #4 transverse reinforcement bar had a top cover of 2 inches, so the #4 longitudinal rebar were placed on 3-inch rebar chairs. Styrofoam inserts were placed in the corrugations of the SIP metal formwork before the rebar was installed as specified in Valmont's UBEAM™ Specification Guide (2024). Figure 5.19 and Figure 5.20 show views of the reinforcement bar after installation was completed.

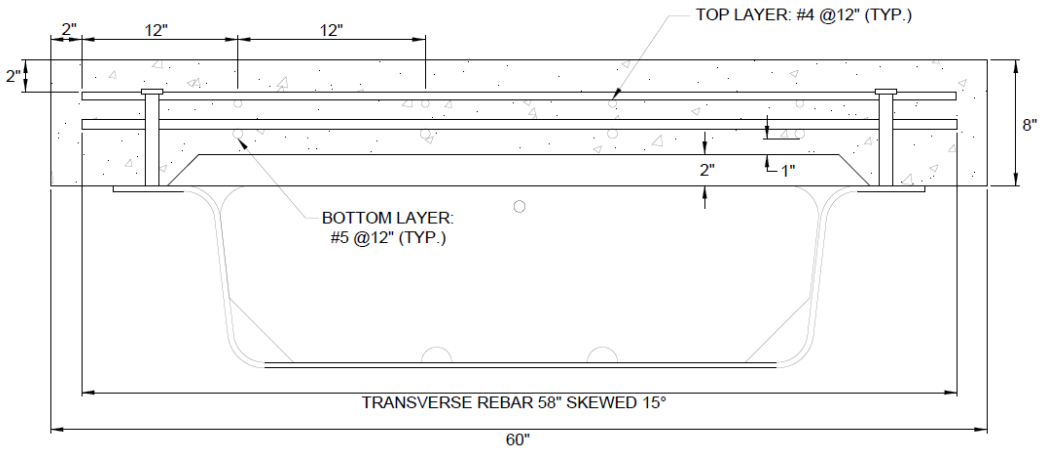

Figure 5.18: Cross-Section view of Deck Reinforcement Pattern

Figure 5.19: Detailed view of Installed Deck Reinforcement

Figure 5.20: Isometric view of Completed Deck Reinforcement

5.4.4 Concrete Pour

On the day of casting, the wooden forms were coated with a generous layer of used hydraulic oil, which acted as a form release for demolding purposes. Form release was used to prevent any damage to the concrete deck when removing the forms and allow them to be repurposed for additional research testing. A concrete bucket was used to transport 3/4-yard of concrete at a time through the laboratory using the overhead crane, shown in Figure 5.21. The deck's surface was water-cured using burlap, which was rehydrated daily. After one week of curing, the half hangers and wooden forms were removed from the deck. The overhang bracket system for forming allows only one nut per hanger/bracket to be lost within the deck. The bolt rod can be unscrewed from the deck slab and reused. Minimal localized damage was seen as the forms broke easily away from the deck slab during demolding. The concrete was allowed to cure for 28 days before flexural testing.

Figure 5.21: Concrete Bucket Used to Transport 3/4 Yard of Concrete

5.5 INSTRUMENTATION

This section discusses the instruments used to collect data during flexural testing.

5.5.1 Instruments

Like the concrete deck slab experiment discussed in Chapter 4: the load was applied to the specimen and measured using an MTS Model 243.70T 330-kip servo-hydraulic actuator. The servo-hydraulic actuator is equipped with instruments such as a load cell and a linear variable displacement transducer (LVDT) that measures the magnitude of loading and the vertical deflection of the specimen at the point of loading ± 10 inches. Two BDI STS LVDTs operating the BDI STS Wi-Fi Data Acquisition System were used during the testing of the U12 specimen to determine the actual deflection of the girder. LVDTs were placed under the top flange on either side of the girder at midspan. Data collected from the LVDTs was averaged to obtain the deflection of the specimen at the loading position and to account for the girder's skew. A Honeywell Model 43 precision low profile 300-kip load cell was used during flexural testing of the U12 specimen.

The load cell was wire-connected using a MS3106A-14S-6S connector to a Micro-Measurements Model 5100 Scanner operating StrainSmart Version 4.72 software to record loading values.

5.6 MATERIAL TESTING

Steel and Concrete samples were tested to determine the material properties to apply to a three-dimensional finite element model to ensure accuracy of the flexural capacity results collected in this experimental study.

5.6.1 Concrete Material Properties

Six concrete samples were cast and tested at WVU to determine the material properties of the concrete deck slab. Concrete cylinders were cast simultaneously as the deck slab. The cylinders were demolded from the plastic molds 48 hours after casting and wet-cured for 28 days before testing for compressive strength. Each cylinder was weighed on a digital scale before compressive testing to determine the weight in pounds. Cylinders were compressed until failure. The average compressive strength was determined to be 3.45 ksi for the U18 deck slab and 5.38 ksi for the U12 deck slab. This value was applied to the analytical model to ensure consistent parameters were used during experimental validation.

5.7 FLEXURAL TESTING

Once the supports were configured at the correct skew, specimens were installed into the testing frame, and the composite concrete deck had cured for 28 days, testing could begin. During destructive testing, readings from the load cell and LVDT within the servo-hydraulic actuator were recorded.

5.7.1 Testing Procedure

The MTS Model 243.70T 330-kip servo-hydraulic actuator applied the load at the midspan of each specimen. The load was applied to a steel spreader beam placed atop an elastomeric pad to reduce the bearing effects and localized concrete crushing.

The testing procedure used for this research effort is similar to that of Chapter 4 and identical to the procedure developed by Michaelson (2014). Each specimen was loaded in stroke control to ensure the safety and accuracy of data collection while flexural testing was in progress. Pseudo-static step loading, which involves loading the specimen in small increments and allowing the load to displace for a specific period, was practiced.

For this experiment, load was applied through displacement starting in 0.10-inch increments. Load and displacement were recorded after the applied load stabilized for 5 minutes. The following load step was then applied. As the behavior of the specimen reached the end of the elastic phase, steps were reduced to 0.05-inch increments to increase the data collected until failure.

5.8 RESULTS

This section presents the data collected and discusses the behaviors observed during flexural testing. Preliminary results and conclusions are drawn in this section.

5.8.1 Testing Results of 15-Degree Skewed Specimens

Figure 5.22 shows the failure mode for a typical U18 specimen. As Michaelson (2014) stated the section's ductility governs the failure mode. The failure can first be seen through the crushing of the concrete deck.

Figure 5.22: Typical Failure Mode for Skewed Composite Specimens

Figure 5.23 shows the load-deflection data collected during flexural testing of the U18 specimen. The U18 specimen was taken to its failure. Buckling in the girder's webs was not present at the time of failure. The girder was further displaced after reaching its ultimate capacity to visually observe the effects of web buckling. It should be noted that there was a calibration issue present within the instruments used at the time of testing and the numerical values shown on the graph do not accurately represent the ultimate capacity. Actions have since been taken with MTS to resolve this issue. The data collected should be analyzed for the shape of the plot, as numbers are not accurate due to this issue. The shape of the graph demonstrates the flexural behavior of the girder with the yielding moment seen well before failure. The yield moment is calculated as 219.38 kips when transformed into a point load. Destructive testing showed web buckling was not present at the time of failure, but occurred after the plastic moment was reached when continued displacement was applied, meaning the girder not behave under noncompact conditions.

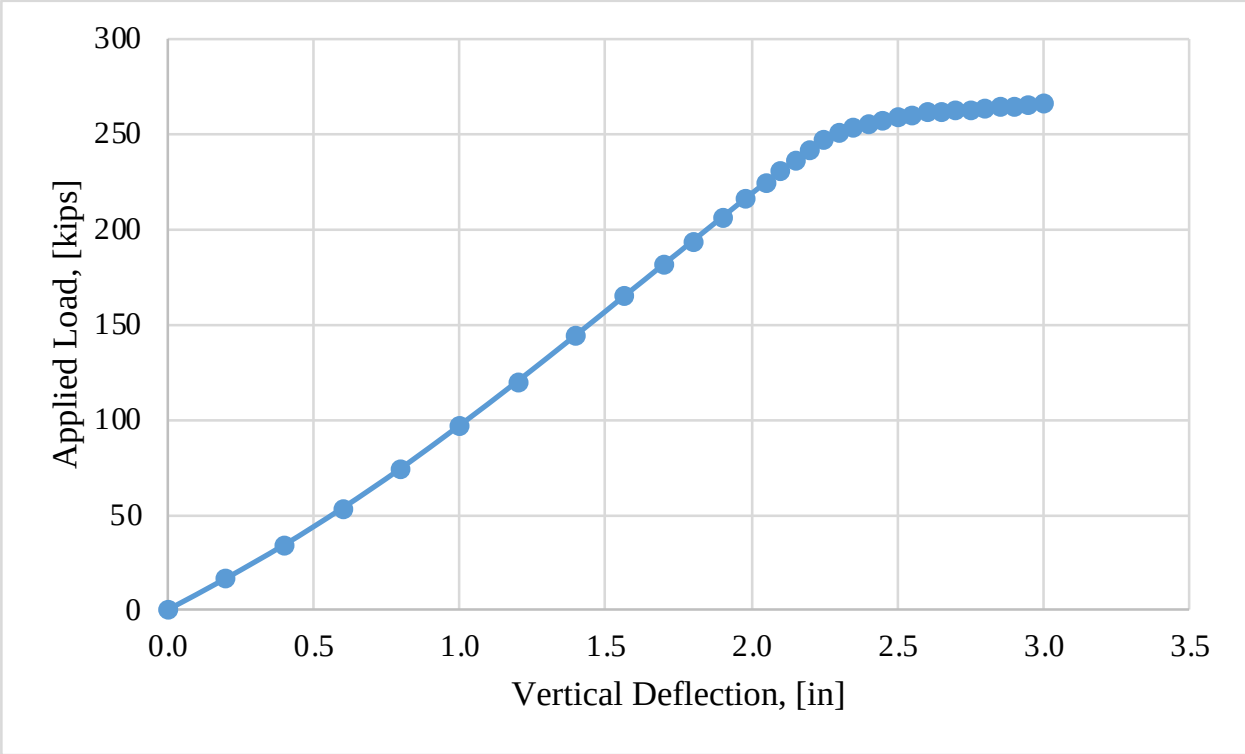

Figure 5.23: Load-Deflection Data from Flexural Testing of Composite U18 with 15-Degrees of Skew

5.8.2 U12 Specimen

Figure 5.24 shows the load-deflection data collected during flexural testing of the U12 specimen. The 'calculated' data is obtained from the maximum deflection equation as follows:

$$\delta_{max} = \frac{PL^3}{48EI} \qquad \text{Eq. 5.1}$$

Where:

P = applied load (kips)

L = bearing-to-bearing span length (inches)

E = modulus of elasticity

I = moment of inertia

The "MTS" line represents the load and deflection data collected from the MTS Model 243.70T 330-kip servo-hydraulic actuator. The "LVDT" plotted line represents the deflection data obtained from the BDI STS LVDTs and load data from the MTS actuator, whereas the "External

Experiment" line depicts the BDI STS LVDT obtained deflection data versus the Honeywell Model 43 300-kip load cell data. This short experiment was performed to determine if the girder's actual deflection compared to the MTS obtained deflection and confirm calibration issues were present within the actuator at the time of testing. Loading was terminated when the load cell measured 106.47 kips to not apply the calculated 201.43 kips needed for the girder to reach it's yielding moment. At an applied load of 106.47 kips, the girder demonstrated no signs of local buckling or yielding, as verified by the linear elastic range displayed, and cracks had yet to form in the concrete deck. Actions have since been taken with MTS to resolve this calibration issue, although the issue was not able to be resolved prior to the completion of this report. The reason for the "External Experiment" plot falling below the "Calculated" or anticipated line is currently unknown.

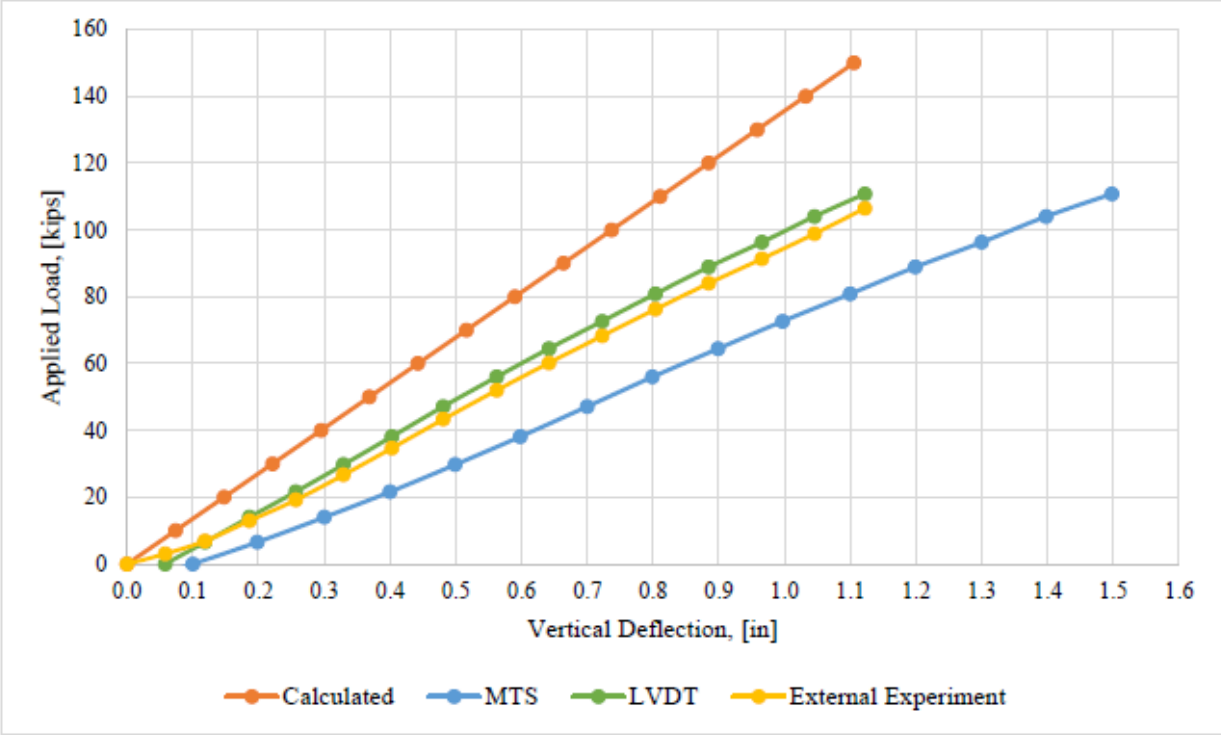

Figure 5.24: Load-Deflection Data from Flexural Testing of Composite U12 with 15-Degrees of Skew

5.9 CONCLUSION

It is essential to the verification of this study and the continuation of this research installment to calibrate the instrumentation used for testing PBFTGs in a laboratory setting. The collected data does demonstrate. The following chapter discusses analytical studies performed on representative PBFTG specimens. The material properties determined in this chapter will be used to model the systems, while flexure data will validate the modeling techniques.

CHAPTER 6: ANALYTICAL MODELING TECHNIQUES

6.1 INTRODUCTION

This chapter discusses the analytical modeling tools and techniques used in this research study, covering aspects like element selection, material definition, and boundary conditions. FEA methods were developed to accurately model and demonstrate the flexural behavior and ultimate capacity of skewed PBFTGs.

Several previous researchers (Barth, 1996; Yang, 2004; Roberts, 2005; Righman, 2005) have proven that S4R elements are sufficiently accurate to model the behavior of plate girder bridges. Since the installment of the research effort on the press-brake-formed system at WVU in 2011, multiple researchers (Michaelson, 2014; Kelly, 2014; Gibbs, 2017; Tennant, 2018; Roh, 2020; Tennant, 2022) have successfully used similar three-dimensional finite element modeling techniques to accurately assess the capacity, fatigue, and live-load distribution behavior of PBFTGs.

6.2 FINITE ELEMENT MODELING TECHNIQUES

The commercial software package Abaqus/CAE (Dassault Systems, 2020) was utilized for finite element analysis in this research effort. This chapter presents the specific provisions employed for project analyses and discusses the applied loads and loading methods.

6.2.1 Element Section

Abaqus stands as a robust commercial finite element software package, boasting a vast library of elements tailored for three-dimensional stress analysis. Prior to diving into problem-solving, it is crucial to assess the appropriateness of a chosen element type. As previously mentioned, extensive research has highlighted the efficacy of S4R shell elements in accurately modeling the physical behavior of both noncomposite and composite steel plate girders.

The S4R element, a 4-node general-purpose shell element, is engineered to furnish reliable and precise solutions for shells of varying thicknesses. Utilizing classical (Kirchhoff) shell theory

for relatively thin shells and thick (Mindlin) shell theory for thicker ones, these elements accommodate finite membrane strains and shell rotations, making them ideal for analyzing large-strain scenarios involving material inelasticity. Moreover, they facilitate adjustments in shell thickness relative to membrane strain and account for transverse shear deformation.

Employing "reduced" integration schemes, S4R elements optimize computational efficiency. By utilizing just one Gauss integration point for a four-noded element, this approach offers advantages over traditional methods. It ensures accurate strain and stress computations at critical locations, enhancing result precision, particularly when elements are not subjected to in-plane bending or disturbance. Furthermore, fewer integration points translate to reduced computing time and storage needs, benefiting users.

However, the reduced integration technique is not without its drawbacks. It may lead to the development of deformation modes that do not induce strain at integration points, potentially resulting in inaccuracies, a phenomenon known as hourglassing. To mitigate this risk, users can introduce a minor artificial stiffness associated with zero-energy deformation modes using the "*SECTION CONTROLS" command within an Abaqus input file.

6.2.2 Material Model

In the study, specific material properties were used for reinforced concrete and steel, in line with the provisions of the AASHTO LRFD. These material properties were integral in ensuring that the modeling and analysis were conducted in compliance with recognized engineering standards and reflected realistic behavior under applied loads. Specific material properties were applied using prior material testing and the provisions outlined in the AASHTO LRFD BDS for steel and reinforced concrete are discussed as follows:

6.2.2.1 Structural Steel

The steel elements in this study were represented using an elastic-plastic constitutive law incorporating strain hardening effects. Specifically, the steel material was characterized using the "*PLASTIC" command within the Abaqus input file, defining it with a standard von Mises yield surface, an associated plastic flow rule (Chen & Han, 1988), and isotropic work hardening. This

modeling approach has been deemed suitable for capturing the rate-independent behavior of metals under relatively monotonic loading conditions where creep effects are negligible (Barth, 1996; Yang, 2004).

Steel tensile samples were extracted from suitable locations during the fabrication of the noncomposite specimens and underwent testing at Turner-Fairbank's Highway Research Center. These noncomposite specimens had previously undergone nondestructive testing conducted by Michaelson (2014), with additional details on the material testing available in his dissertation. Figure 6.1 displays the results of the coupon tests from Turner-Fairbanks' tensile testing.

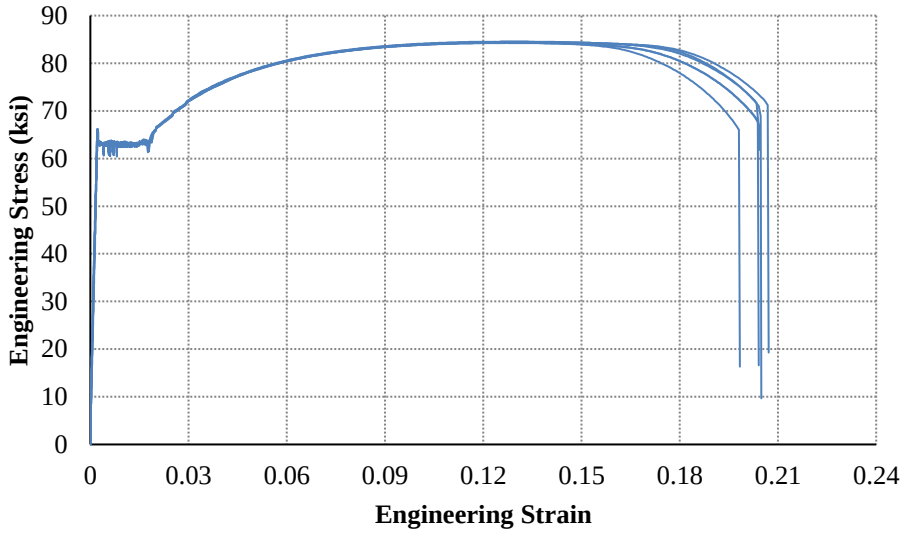

Figure 6.1: Results from Tensile Testing of Steel Coupons (Michaelson, 2014)

To capture the stress-strain characteristics, a multilinear relationship (Galindez, 2009) was employed, as depicted in Figure 6.1. Critical points in the nonlinear region of the curve were determined based on coupon testing of samples, as previously mentioned, and are outlined in Table 6.1. Subsequently, the stress-strain relationship was transformed into true stress and true plastic strain terms (Chen & Han, 1988), as necessitated for inclusion in the Abaqus input file.

Table 6.1: Average Steel Plate Properties (Michaelson, 2014)

Property	Average Value
Modulus of Elasticity, E (ksi)	29559
Static Yield Stress, σ_y (ksi)	60.962
Offset Yield Stress, $\sigma_{0.2\%}$ (ksi)	63.05
Strain at the Onset on Strain Hardening, ε_{st} (%)	1.7883
Strain Hardening Modulus, E_{st} (ksi)	1033.5
Tensile Stress, σ_u (ksi)	84.382
Strain at the Tensile Stress, ε_u (%)	13.165

The following properties were used to model structural steel in the models:

Yield Strength: Taken as 60.96204 per stress/strain material testing curve from (Michaelson, 2014) (see Figure 6.1 and To capture the stress-strain characteristics, a multilinear relationship (Galindez, 2009) was employed, as depicted in Figure 6.1. Critical points in the nonlinear region of the curve were determined based on coupon testing of samples, as previously mentioned, and are outlined in Table 6.1. Subsequently, the stress-strain relationship was transformed into true stress and true plastic strain terms (Chen & Han, 1988), as necessitated for inclusion in the Abaqus input file.

- Table 6.1)
- Modulus of Elasticity: Taken as 29,000 ksi
- Poisson's Ratio: Taken as 0.3

6.2.2.2 Reinforced Concrete

In Tennant's (2022) study, he discovered that shell elements were inadequate in accurately modeling the behavior of the concrete deck when bearing skew was introduced to the analytical model. His original models exhibited premature failure at loads nearing the steel's yield point and concrete's cracking threshold. Cracks in the bottom face would propagate across the entire thickness of the deck too quickly, resulting in inaccurate representations. To address this, continuum (brick) elements replaced shell elements in the concrete deck. This alteration allowed for multiple elements throughout the deck thickness, enabling crack propagation through some elements without causing overall failure. Figure 6.2 depicts a cross-section of the composite PBFTG with multiple continuum elements spanning the deck thickness (Tennant, 2022).

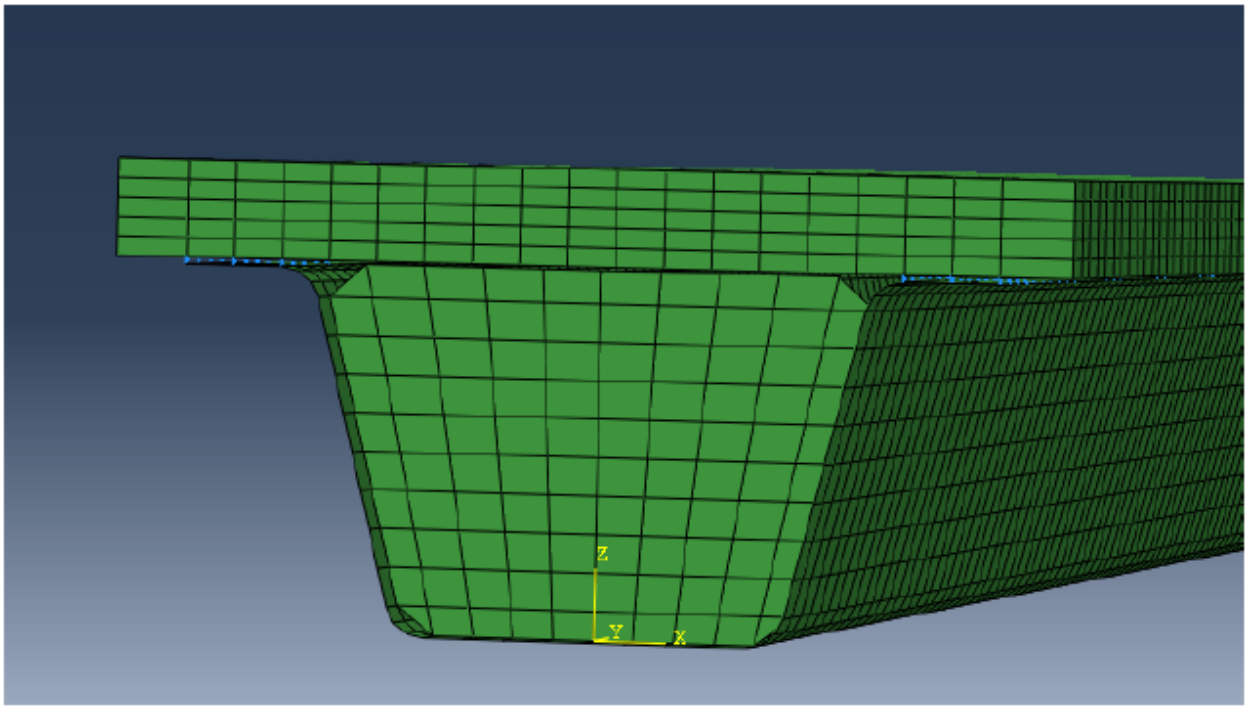

Figure 6.2: Cross-section of PBFTG with Brick Elements in the Deck (Tennant, 2022)

In this study, elements representing reinforced concrete employ a brick-element concrete model along with reinforcement definitions tailored to specific elements. To delineate, the concrete is characterized using the "*CONCRETE" and "*TENSION STIFFENING" commands within the Abaqus input file. Previous research successfully utilized a smeared crack model, which does not track individual "macro" cracks but conducts constitutive calculations independently at each integration point of the finite element model (Michaelson, 2014). Crack presence influences these calculations by modifying stress and material stiffness at the integration point. Once detected, cracks persist for the duration of the calculation, albeit they may undergo opening and closing cycles. Subsequently, the presence of cracks alters calculations as a damaged elasticity model is utilized (Dassault Systèmes, 2010).

In Tennant's (2022) behavioral study, the integration of continuum elements improved the model, but it did not completely resolve all issues with the concrete material model. The analytical models continued to experience premature failure before reaching significant loading levels. Errors emerged consistently, with divergence occurring at skew angles as low as 5°. It was observed that failure occurred when the bottom face of the concrete deck, directly under the load, reached the 92

tensile rupture stress of the concrete (Tennant, 2022). To address this issue in modeling, the reinforcement bar within the deck was considered.

Concrete element modeling incorporated provisions for the steel reinforcement within the deck. Specifically, the reinforcement is accounted for using the "*REBAR" option in the Abaqus input file, expressed as linear reinforcement positioned at user-defined locations within the concrete deck, as opposed to a smeared layer. This is done to consider for the skewed transversely placed rebar placed within the concrete deck. As discussed in Section 4.3.1, rebar elements are placed parallel to the direction of skew in girders with skews up to 25° to prevent cracking due to the lack of reinforcement in the direction of principal stress.

Properties to accurately model the reinforced concrete are listed as:

- Compressive Strength:
    - U18 Experimental Test: 3.45 ksi per material compressive testing
    - U12 Experimental Test: 5.38 ksi per material compressive testing

    - Behavioral Study: 4.0 ksi per AASHTO LRFD BDS Section 5.4.2.4
- Modulus of Elasticity: Determined to be 3,640 ksi, using 1,820 × √fc’
- Poisson’s Ratio: Taken as 0.2 per AASHTO LRFD BDS Section 5.4.2.5

6.2.3 Boundary Conditions and Multi-Point Constraints

In all models within the presented studies, the boundary conditions are set as pin-roller conditions, as that is the most commonly used support condition in bridge construction. Conditions restricted lateral displacements to reflect real-world scenarios most accurately. In ensuring composite action between the reinforced concrete deck and the steel girder, beam-type multi-point constraints (MPCs) are utilized in the finite element modeling. These constraints create a rigid beam between two nodes, constraining displacement and rotation at the first node to that at the second node. To establish MPC elements, the mesh of the concrete slab is arranged with nodes vertically aligned above those in the middle of the top flange. Specifically, the “*MPC” option is employed to rigidly connect nodes in the center of the top flange, at the web-flange conjunction, to the node directly above the junction in the concrete deck. An image of one of the finite element models from the sensitivity study described in (Woldegabriel, 2023) is displayed in Figure 6.2, depicting boundary conditions in orange and mesh discretization. Though MPC labels are removed from the display for clarity, connections between the concrete deck and the top flanges of the PBFTGs are visible.

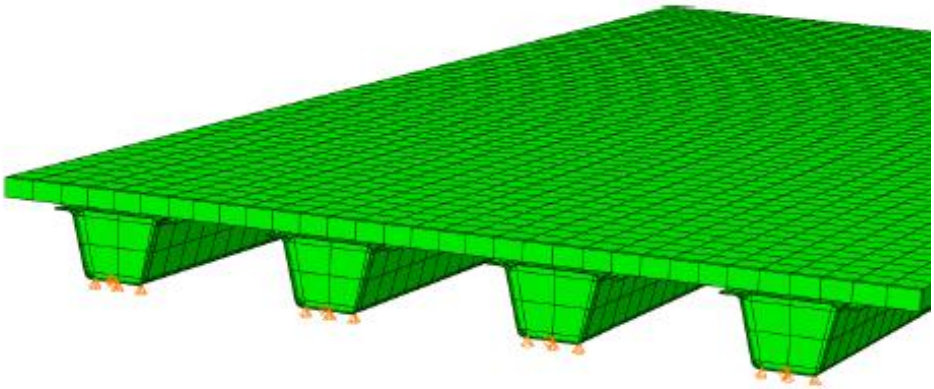

Figure 6.2: Abaqus model of the Flat Run Bridge (Woldegabriel, 2023)

6.3 CONCLUSION

This chapter presented an explanation of the analytical modeling techniques used for assessing the behavior of PBFTGs. Verification is taken from FEA modeling performed by Michaelson (2014) and Tennant (2022), which can be reviewed in more detail in Chapter 2: and their respective dissertations. These tools will be used further in the following chapter to discuss a behavioral study that will assess the capacity and compactness of a matrix of PBFTG bridges.

CHAPTER 7: ASSESSMENT OF SKEW ON THE FLEXURAL CAPACITY OF PBFTGS SENSTIVITY STUDY

7.1 INTRODUCTION

The purpose of this chapter is to present a study focused on assessing the flexural behavior of low-skewed PBFTG bridges. The goal of this study is to determine the applicability of the strength limit state provisions set forth in the AASHTO LRFD BDS. PBFTGs with skews up to 20° can be classified as compact sections. Specifically, a matrix of low-skewed PBFTGs were analytically modeled to assess how the ultimate capacity of the system is affected by skew angles ranging between 0° – 20°. A comprehensive comparison between the analytically obtained and the calculated ultimate moment capacities from empirical equations outlined in the AASHTO LRFD BDS is also presented.

7.2 SENSITIVITY STUDY

This chapter will review the constant and varied parameters employed in the FEA modeling and explore how bearing line skew impacts the flexural strength of PBFTGs. This will be done through exploratory correlation analysis. This study specifically aims to determine if PBFTGs with skews up to 20° can be classified as compact sections.

This sensitivity study presents a matrix of PBFTGs that were analytically modeled using three-dimensional FEA techniques, which will be used to assess the behavior and impact skewness further has on the flexural resistance of PBFTGs. Michaelson (2014) and Tennant (2022) presented data in their respective dissertations that suggests that PBFTGs outperform the ultimate capacity limit states set forth by AASHTO LRFD BDS Article 6.11.2, discussed in further detail in Sections 3.4 and 3.7, and can be classified as compact sections. The compactness classification provisions set forth by Johnston and Mattock's (1967) are exceptionally outdated and are derived from a limited understanding of the system's behavior at the time.

7.2.1 Background and Contributions of Previous Testing

Ebeido and Kennedy (1996a and 1996b) conducted parametric investigations on over 600 prototype continuous skew composite bridges using Finite Element Analysis (FEA). The validity of the analytical modeling was confirmed through experimental tests conducted on three continuous and six simple span composite bridges with concrete decks on steel beams. They derived empirical equations for main span moment, interior support moment, reaction, and shear distribution factors. Findings from the study indicate that as skew angle increases, the main span and interior support moments decrease while reactions and shear in the obtuse corner increase. Furthermore, the impact of skew on shear and moment distribution factors becomes significantly pronounced for skew angles exceeding 30°.

A behavioral study performed by Tennant (2022) presented preliminary results showing a collection of low-skewed PBFTGs that followed the same curve on a load-deflection plot as the composite 0° specimens that Michaelson (2014) performed destructive testing. Results of this study indicated girders that possessed 20° or less bearing line skew follow a load-deflection curve similar to that of a girder with a 0° (or straight) bearing line, while girders with a bearing line skew angle larger than 20° abruptly terminate at earlier vertical deflections. From Tennant's (2022) behavioral study, it can be assumed that girders under 20° of skew behave like a PBFTG with 0° of skew and excide capacity limits, the stiffness of PBFTGs increases as skew increases, girders terminate earlier at higher skews, with 45° skewed girders performing just above the nominal flexural resistance calculated using the AASHTO LRFD BDS.

7.2.2 Data Description

The data set for this research effort consists of 3,509 analytical composite PBFTGs that were modeled using three-dimensional finite element analysis tools and techniques. All girders in the data set specifically use Valmont U-BEAM tub girders properties and parameters.

7.2.2.1 Constant Parameters

The following parameters remained constant in this sensitivity study:

- The deck thickness was taken to be 8 inches for all modeled girders.

- Specific material properties were applied using the provisions outlined in the AASHTO LRFD BDS for steel and reinforced concrete:
    - Steel:
        - Yield Strength: Taken as 60.96204 per stress/strain material testing curve from (Michaelson, 2014)
        - Modulus of Elasticity: Taken as 29,000 ksi
        - Poisson's Ratio: Taken as 0.3
    - Reinforced concrete:
        - Compressive Strength: 4.0 ksi per AASHTO LRFD BDS Section 5.4.2.4
        - Modulus of Elasticity: Determined to be 3,640 ksi, using $1{,}820 \times \sqrt{fc'}$
        - Poisson's Ratio: 0.2 per AASHTO LRFD BDS Section 5.4.2.5
- Normal weight concrete was used in accordance with AASHTO LRFD BDS Table 3.5.1-1
    - Steel unit weight: 0.150 kcf
    - Reinforced concrete unit weight: 0.490 kcf
- Valmont® U-BEAM™ standard cross-section dimensions were used for all tub girders in the matrix.

7.2.2.2 Varied Parameters

The following parameters varied in the analytical matrix before undergoing statistical analysis to determine their correlation and impact on the ultimate flexural capacity:

- Five standard Valmont U-BEAM™ shapes: U12, U18, U24, U30, and U33 (see Figure 7.1 and Table 7.1).
- Span lengths are modeled ±5 feet outside of each U-BEAM shape's applicable range detailed in Valmont's "U-BEAM™ Depth Selection Chart - Compact Design" under loading group A in 5-foot increments (see Table 7.2 and Figure 7.2).
- Eleven skew angles in units of degrees: 0° to 20° in 2° increments.
- Eleven deck width configurations where the width of the deck is equal to $\sqrt{w(1+a)}$ (see Figure 7.3).

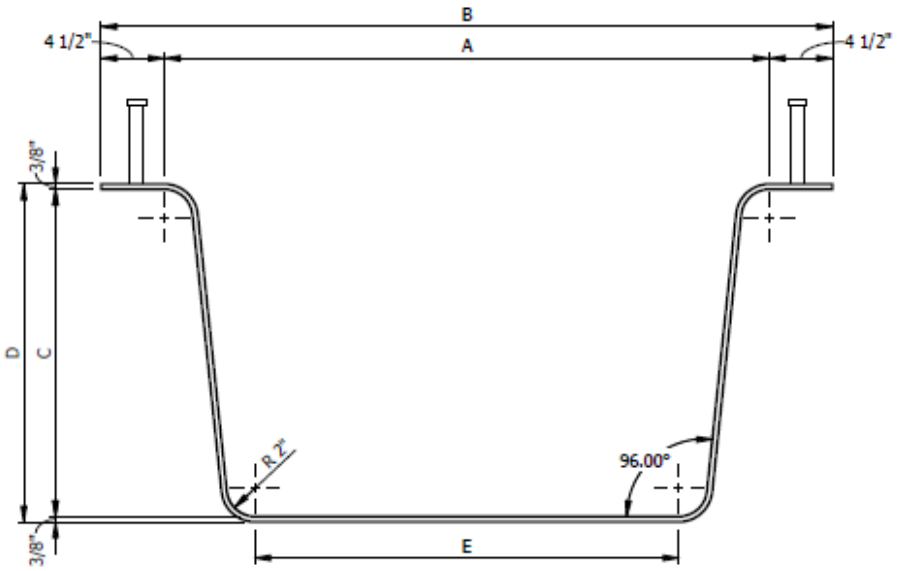

Figure 7.1: Typical Valmont® U-BEAM™ Cross-Section

Table 7.1: Corresponding Typical U-BEAM™ Cross-Section Dimensions

DESIGNATION	A	B	C	D	E
U12	43"	52"	11 1/4"	12"	32 5/8"
U18	43"	52"	17 1/4"	18"	31 3/8"
U24	43"	52"	23 1/4"	24"	30 1/8"
U30	43"	52"	29 1/4"	30"	28 7/8"
U33	45"	54"	32 1/4"	33"	30 1/4"

Table 7.2: Applicable U-BEAM™ Span Ranges

Property	Valmont® U-BEAM™ Designation				
	U12	U18	U24	U30	U33
L_{min} [ft]	20	35	50	60	65
L_{max} [ft]	45	60	75	80	90

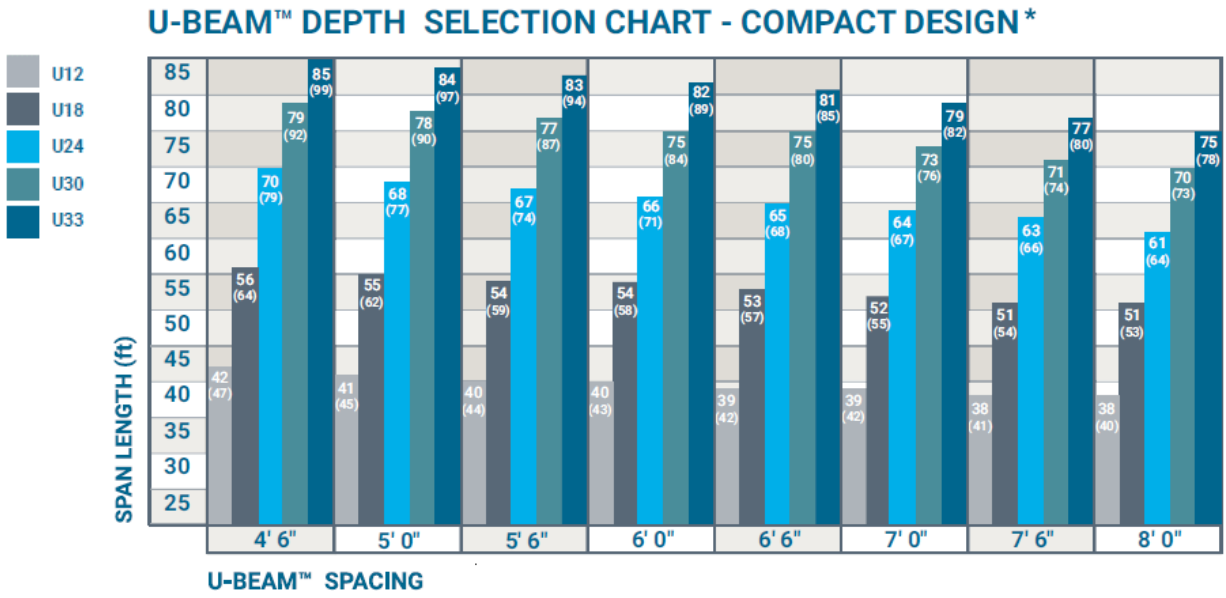

Figure 7.2: U-BEAM™ Depth Selection Chart - Compact Design for Loading Group A (Valmont, 2024)

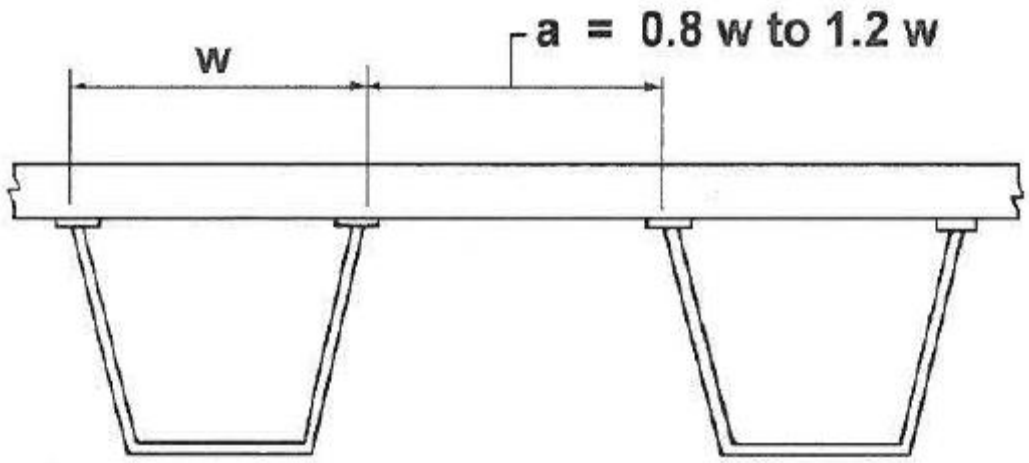

Figure 7.3: Center-to-Center Flange Distance (AASHTO, 2020)

7.3 Results of the Sensitivity Study

General statistical results of the sensitivity study will be presented herein. Overall results of the parametric study will be displayed as well as a comprehension comparison with current AASHTO LRFD specifications will be in the following chapter.

Fit models show there is little to no correlation between skewness and ultimate capacity computed from FEA and AASHTO equations. Noncompact behavior is not present among the majority of the matrix's girders.

7.3.1 Comparison to Current AASHTO Specifications

From AASHTO LRFD BDS Article 6.11.2.3, if a composite box section qualifies as compact, the nominal flexural resistance of the section is determined using Equation 7.1 or Equation 7.2:

If $D_p \leq 0.1\ D_t$, then:

	$M_n \leq M_p$	Eq. 7.1

If $0.1D_t < D_p \leq 0.42D_t$,

	$M_n = M_p \left(1.07 - 0.7\frac{D_p}{D_t}\right)$	Eq. 7.2

Where:	
D_p =	distance from the top of the concrete deck to the neutral axis of composite section at the plastic moment
D_t =	total depth of the composite section
M_n =	nominal flexural resistance of a section
M_p =	plastic moment of the composite section

Using Equations 7.1 and 7.2 from the AASHTO LRFD BDS (2020) to represent the compactness limit state through the orange line plotted, Figure 7.4 illustrates the comparison of compactness for the entire matrix of PBFTGs. The FEA capacity ratios are displayed in the figure for each Valmont® U-BEAM™ size. Compact capacity (Mn/Mp) ratios were determined and then a reduction factor, which limits the capacity ratio to 1.0, was applied to each girder before they were plotted against their respective Dp/Dt values. Forty-two girders fell below the AASHTO line

of compactness when AASHTO LRFD BDS compact section flexural resistance equations. Thus, the flexural capacity of 3467, or 98.8% of the girders in the matrix are underpredicted for capacity, exceeding compact section requirements set by AASHTO LRFD.

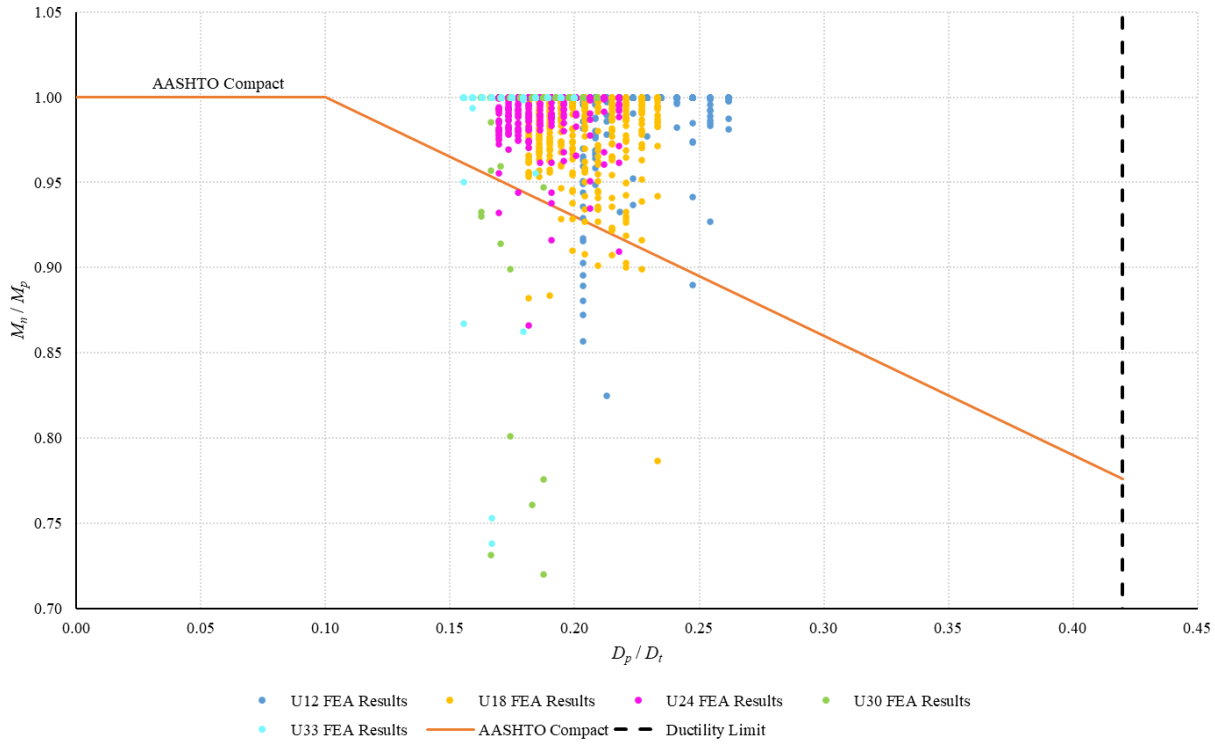

Figure 7.4: Evaluation of AASHTO Compact Capacity Specifications by UBEAM™ Shape

While the modeling matrix of PBFTG bridges is majorly compact, variations in girder parameters may classify a composite box girder as noncompact according to AASHTO Specifications. If this is the case, the capacity of the girder is limited to the yield moment, M_y. This is determined by the following equations, which were applied directly to this scenario. The derivation is as follows:

	$F_{nc} = R_b R_h F_{yc}$	Eq. 7.3
Where:		
F_{nc} =	nominal flexural resistance of box flanges in compression	
R_b =	web load shedding factor = 1.0 since the section is composite and satisfies D/t_w	

R_h =	hybrid girder factor = 1.0 as the girders are formed using a single plate
F_{yc} =	specified minimum yield strength of the compression flange

	$F_{nt} = R_h F_{yt} \Delta$	Eq. 7.4
In which:		
	$\Delta = \sqrt{1 - 3\left(\frac{f_v}{F_{yt}}\right)^2}$	Eq. 7.5
	$f_v = \frac{T}{2A_O t_f}$	Eq. 7.6

Where:	
F_{nt} =	nominal flexural resistance of box flanges in tension
F_{yt} =	specified minimum yield strength of the tension flange
R_h =	hybrid girder factor = 1.0 as the girders are formed using a single plate
Δ =	reduction factor for the maximum stress in a box flange = neglected due to the unlikely presence of torsion in the proposed system of short-span structures
f_v =	St. Venant torsional shear stress in the flange due to the factored loads at the section under consideration (ksi)

The yield moment of the composite section in positive flexure is calculated following a procedure specified in AASHTO LRFD BDS Section D6.2. Symbolically, the procedure is shown by solving Equations 7.7 and then 7.8. Additionally, the yield moment of the section shall be taken as the lesser value calculated for the compression flange or the tension flange.

Solve for M_{AD} from the equation:

	$F_{yf} = \frac{M_{D1}}{S_{NC}} + \frac{M_{D2}}{S_{LT}} + \frac{M_{AD}}{S_{ST}}$	Eq. 7.7

The yield moment can then be calculated by:

	$M_y = M_{D1} + M_{D2} + M_{AD}$	Eq. 7.8

Where:	
F_{yf} =	yield strength of the flange under consideration
M_{D1} =	moment due to the noncomposite dead loads
M_{D2} =	moment due to the composite dead loads
M_{AD} =	moment due to the additional applied loads
S_{NC} =	noncomposite elastic section modulus
S_{ST} =	short-term elastic section modulus
S_{LT} =	long-term elastic section modulus
M_y =	yield moment

As the concrete deck is shored during construction and no additional composite dead loads are applied during testing, Equations 7.7 and 7.8 can be combined and simplified to form Equation 7.9.

	$M_y = \min(F_{yc}S_{fc}, F_{yt}S_{ft})$	Eq. 7.9

Where:	
M_y =	yield moment
F_{yc} =	yield strength of the compression flange
F_{yc} =	yield strength of the compression flange
S_{fc} =	short-term composite compression flange elastic section modulus
S_{ft} =	short-term composite tension flange elastic section modulus

7.3.2 Influence of Skewness

The effect of skew angle on the flexural resistance of PBFTGs is represented in Figure 7.5. It should be noted that the results are presented in two separate graphs to not confuse the two due to the comparison between ratios. The ratio Mn/My is greater than Mn/Mp due to the smaller yield moment over the plastic moment occurring in the denominator. Figure 7.5 depicts the FEA obtained nominal flexural resistance and plastic resistance ratio versus each skew angle modeled in the matrix.

Under compact conditions, most girder sizes demonstrate little to no difference in capacity between girders with 0º – 20º of support skew. Figure 7.6a demonstrates that compact behavior exists at all skew angles and girder sizes, with the exception of U18 girders with 0º – 10º skews experiencing a 2% reduction in their ultimate capacity. These girders still demonstrate a capacity well above their respective yielding moments. U12, U30, and U33s shows an increase in ultimate capacity with an increase of bearing line skew.

Figure 7.6b depicts the shape factor for each girder shape versus each skew angle modeled in the matrix. It can be noted that all girders possess a nominal flexural moment that exceeds their respective yielding moments, by a minimum of 30%. U12 girders demonstrate a 34% to 37% greater capacity at all skew angles modeled than M_y. Each girder shape continues to show a slight increase in capacity with each additional influence of skew for all girder shapes. U33 girders behave with a nominal capacity 55% greater than their yield moments and increase to almost a 65% greater nominal moment at 20º skew angles. The nominal flexile resistance demonstrates a greater capacity at girder shapes with larger girder depths. A 3 – 9% increase in the nominal flexural moment when compared to yield moment is present with the model.

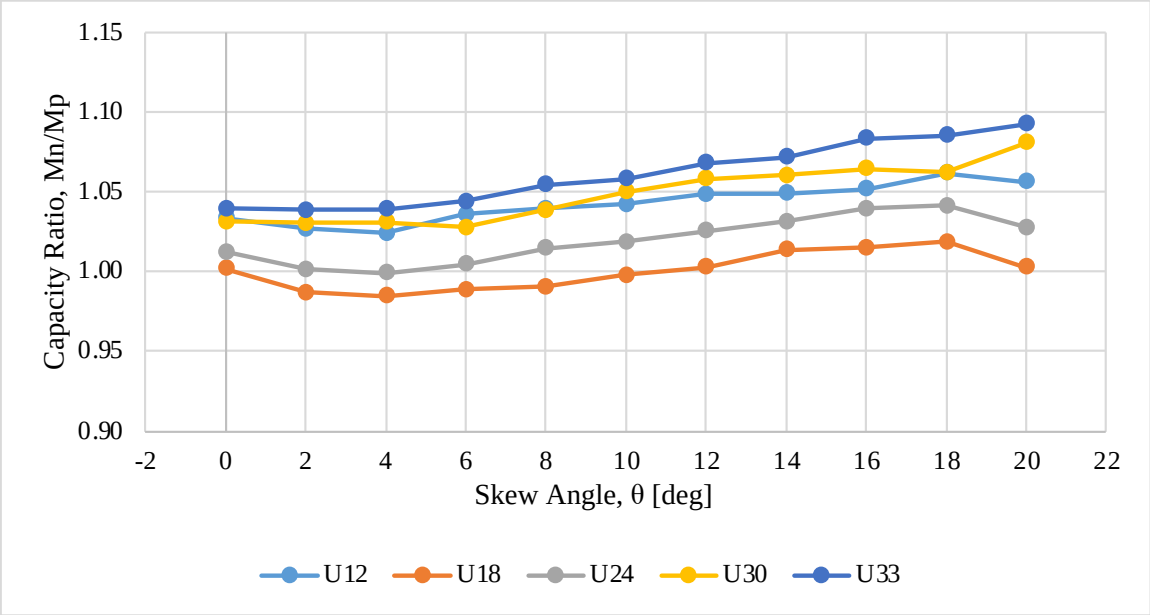

(a)

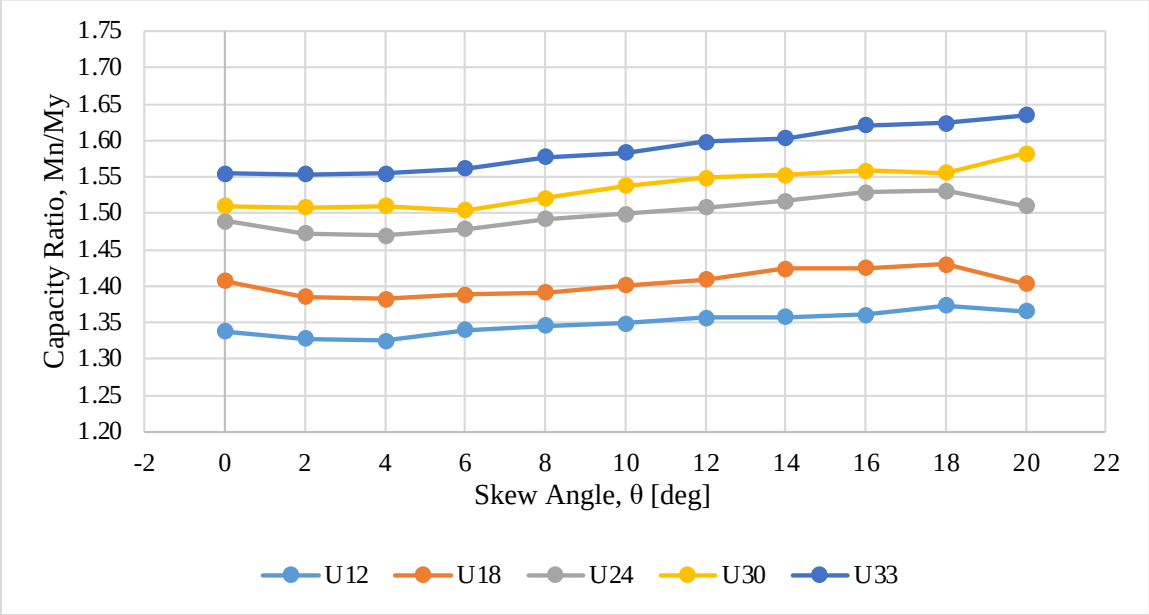

(b)

Figure 7.5: Comparison of the Influence of Skew Angle on the Capacity (a) (M_n/M_p), (b) (M_n/M_y)

7.3.3 Influence of Span Length

Figure 7.6 illustrates a comparison of the span length on the compact capacity ratio (M_n/M_p) and the shape factor (M_n/M_y) denoted by U-BEAM™ girder size. Figure 7.6a show girders experience similar compact capacities at all variations of span length across all girder shapes. All girder shapes, excluding a slight decrease in U18s around 60 feet, are equal to or greater than $M_n/M_p = 1.0$, where the AASHTO underpredicts capacity. Almost all girders in the model experience a 0 – 6% increase in capacity compared to the plastic moment which is well beyond the yield limitation that is currently in place. Span length is demonstrated to have zero impact on the plastic and nominal flexural moments for all PBFTGs in the model under compact conditions.

The shape factor graph displayed in Figure 7.6b expresses span length in terms of Mn/My at each girder size. In this instance, all girders experience at least a 25% increase in capacity compared to the yielding moment. Girders with greater depths experience greater ultimate capacities, as well as greater capacities at greater span lengths. Span length has zero effect on the nominal flex capacity of PBFTGs with skews up to 20°, although it is clear that length is an important factor when determining the yield moment of a section. U12s have ultimate capacities 25 – 50% greater than their yielding moment, depending on span length. It is seen that U33s experience a 50% greater ultimate capacity than their respective yield moment at 65 feet and a 67.5% increase in capacity at 90-foot spans. This confirms that current AASHTO provisions reduce the ultimate capacity of PBFTGs by up to 67.5% by classifying PBFTGs as noncompact sections under skew.

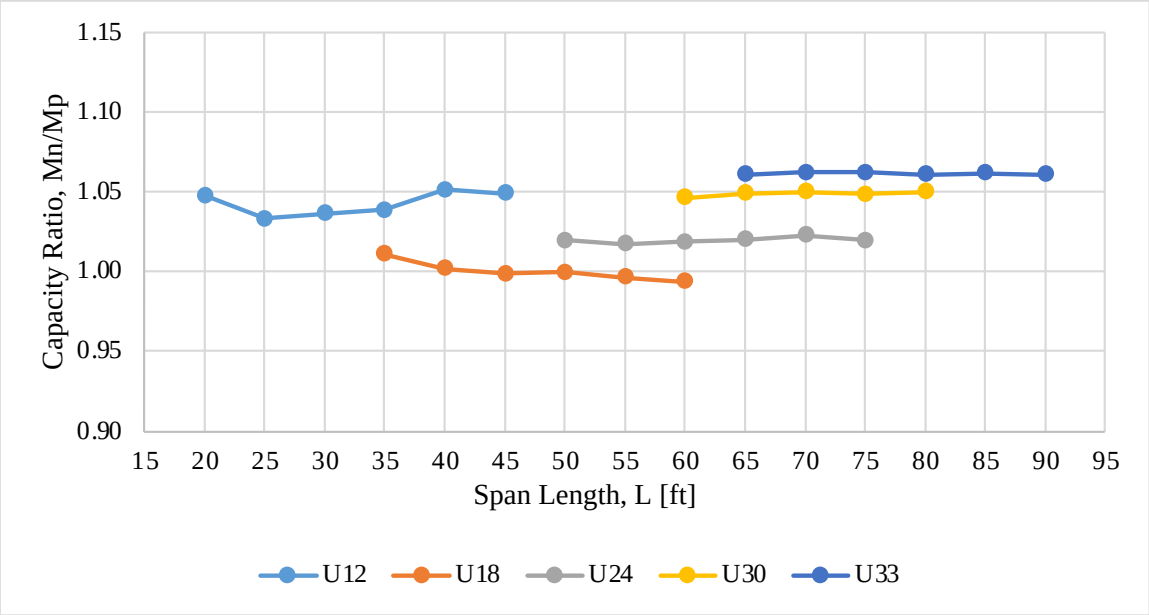

(a)

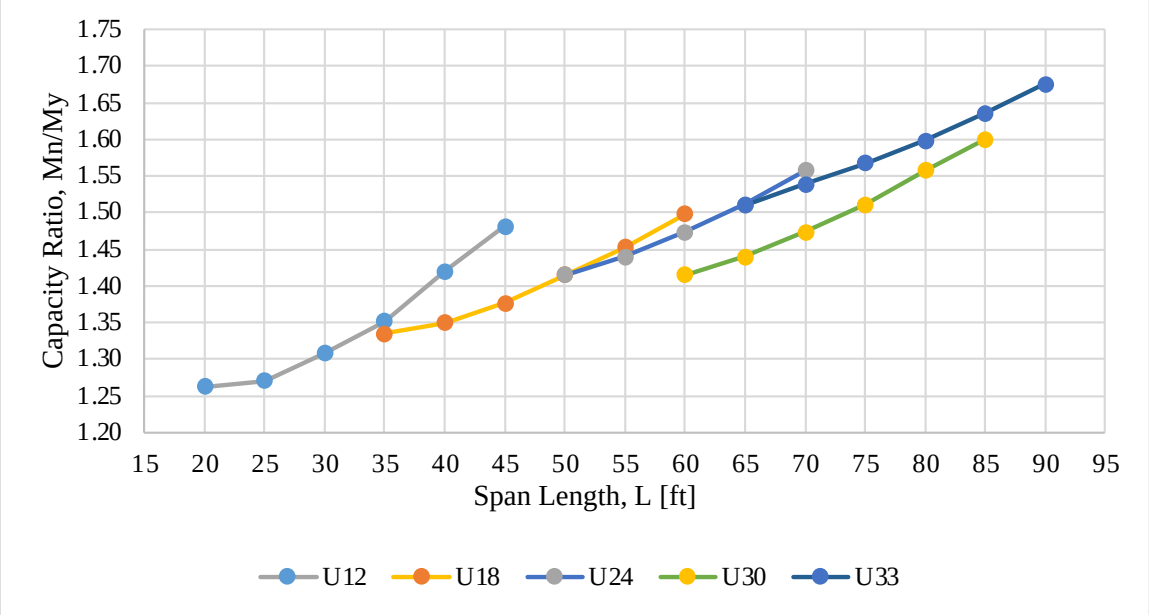

(b)

Figure 7.6: Comparison of the Influence of Span Length on the Capacity (a) (M_n/M_p), (b) (M_n/M_y)

7.3.4 Influence of Deck Size

Figure 7.7 presents a comparison of the deck configuration on capacity ratios. As previously mentioned, requirements of Article 6.11.6.2.2 were employed to compute the corresponding deck widths, which state that, for a composite box girder to be considered compact, the distance center-to-center of flanges of adjacent boxes, *"a*," shall neither be greater than 120 percent nor less than 80 percent of the distance center-to-center of the flanges of each adjacent box, *w* (ASSHTO, 2020 and Michaelson, 2014). To ensure the entire matrix of applicability was accounted for, "*a*" was modeled from 0.75 to 1.25 in 0.05*w* increments. The figures show greater compact capacities with smaller UBEAM™ sizes, although U12 girders are outperformed by their adjacent counterparts. It should also be noted that the compact capacity decreases as the deck width or center-to-center flange distance increases, although the difference can be assumed negligible.

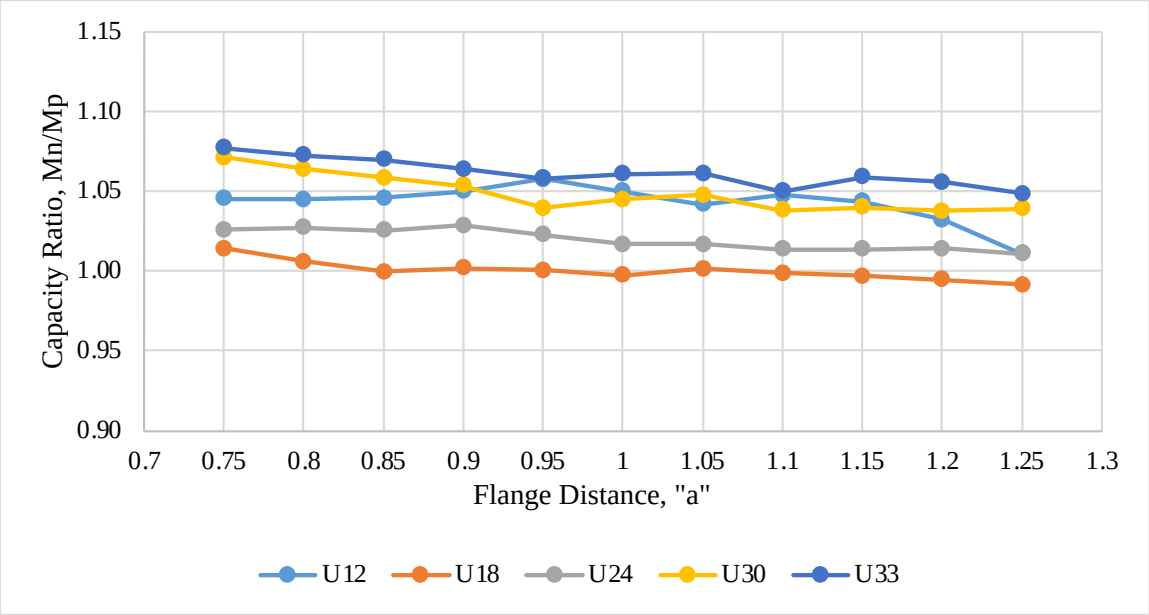

(a)

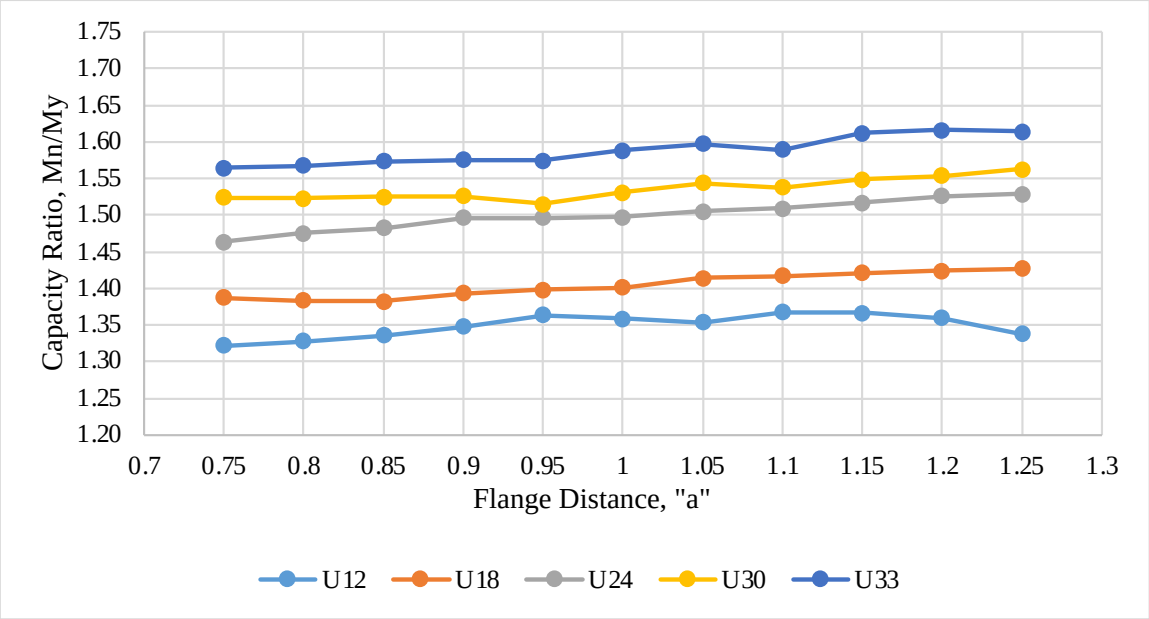

(b)

Figure 7.7: Comparison of the Influence of Flange Distance on the Capacity (a) (M_n/M_p), (b) (M_n/M_y)

7.4 CONCLUSION

The sensitivity study results show that all girder types that possess skews between 0° and 20° behave with capacities that exceed the yielding moment and noncompact behavior is not present within the matrix of bridges that were modeled. PBFTGs with skew angles less than 20 degrees can be considered compact sections, as these skew angles display no effect on flexural resistance. The flexural capacity of PBFTGs is also not affected by span length or deck width.

CHAPTER 8: SUMMARY AND CONCLUDING REMARKS

8.1 PROJECT SUMMARY

The scope of this research study was to observe the ultimate flexural capacity of PBFTGs with skews up to 20º to demonstrate that low-skewed PBFTGs can be classified as compact sections and have broader applicability when designing the system using current AASHTO LRFD Specifications. This was done through the following tasks:

- Reviewing current literature relating to PBFTGs and their behavior.
    - Over a decade of successful research has been done at WVU on the PBFTG system to assess behavior through laboratory experiments, analytical FEA modeling, and field-testing analysis.
- Understanding the specifications and limitations on PBFTGs that are set forth by the current AASHTO LRFD BDS.
    - Current governing specifications classify all skewed PBFTGs as noncompact sections, which limits the flexural capacity of these girders to their moment at first yield.
    - The compactness classification for PBFTGs is derived from analytical studies that were performed in the 1960s. Specifications for the system are outdated and significantly limit the applicability of this system in bridge designs. These studies lacked a thorough understanding of the system and were not scientifically derived as a result. With an increase in knowledge and technology, today's studies have since been able to gain a deeper understanding of their physical behavior.
- Performing experimental flexural testing to observe how low-skewed PBFTGs behave to draw comparisons to straight PBFTGs and capacity limitations on the system due to their noncompact classification in AAHSTO LRFD Specifications.
    - Preliminary results of the skewed reinforced concrete deck slab study show that specimens with 10° and 20° of skew have a higher capacity than those with no skew.
    -

    - While flexural testing was not able to be completed for both 15° skewed PBFTGs, as it is known that a calibration error is present within the testing instrumentation, the shape of the data collection load versus the deflection plot shows similarities between previous research performed on nonskewed or straight PBFTGs.
- Developing analytical three-dimensional finite-element modeling techniques to depict the capacity of skewed composite PBFTGs accurately.
    - This was done through the use of linear material properties to determine the behavior of PBFTGs when loaded to ultimate capacity.
    - A series of brick elements and linear embedded rebar was used to model the reinforced concrete deck and skewed reinforcement bar within the deck. These modeling techniques were developed from previous testing done in Tennant's 2022 research effort, and further verification will be provided once accurate calibration of testing instruments is completed.
- Conducting a behavioral study to assess the impact skew has on the ultimate capacity of PBFTGS and determined compactness classification.
    - A sensitivity study with four varied parameters was performed using a matrix of three-dimensional FEA-modeled bridges to determine ultimate capacity, including girder size, skew angle, span length, and deck width.
    - An analysis was performed to determine the impact each parameter had on the yield, nominal, and plastic moments of each girder in the matrix.
    - Results show that all girder types that possess skews between 0° and 20° behave with capacities that exceed the yielding moment. The models actually show an increase in capacity with an increase in skew.
    - Non-compact behavior is not present within the matrix of bridges modeled in the sensitivity study.
    - The flexural capacity of PBFTGs is not affected by span length or deck width.

8.2 CONTINUED RESEARCH AND RECOMMENDATIONS

The author recommends the following efforts for future research and expansions of this project:

- Resolve current calibration issues with the current MTS system to restore accuracy to data collected during destructive testing using internal instruments.
- Complete FEA modeling and verify the modeling techniques against the experimental results obtained from the FEA once the instrumentation has been calibrated.
- Perform sensitivity and parametric studies to determine the effects of additional varied bridge parameters on the ultimate capacity for low- and high-skewed PBFTGs.
- Investigate the flexural behavior of PBFTG bridges with skew angles greater than 20 degrees through both experimental testing and analytical modeling.

REFERENCES

AASHTO - AASHTO Innovation Initiative - Steel Press-Brake-Formed Tub Girder. (2021). Aii.transportation.org. https://aii.transportation.org/Pages/Steel_PBFTG.aspx

AASHTO - AASHTO Innovation Initiative - About AII: Background. (n.d.). Aii.transportation.org. Retrieved April 15, 2024, from https://aii.transportation.org/Pages/AIIBackground.aspx

American Association of State Highway and Transportation Officials. (2020). AASHTO LRFD Bridge Design Specifications, Ninth Edition. Washington, DC.

American Association of State Highway Officials. (2017). AASHO Standard Specifications for Highway Bridges, Eighth Edition. Washington, DC.

American Institute of Steel Construction. (2017). *Steel Construction Manual* (15th ed). Chicago, IL.

Barth, K. E. (1996). Moment-rotation characteristics for inelastic design of steel bridge beams and girders (Doctoral dissertation, Purdue University).

Barth, K. E., & Wu, H. (2006). Efficient nonlinear finite element modeling of slab on steel stringer bridges. Finite Elements in Analysis and Design 42(14), 10.

Chandar, G., Hyzak, M. D., & Wolf, L. M. (2010). Rapid, economical bridge replacement. *Modern Steel Construction*.

Chong, J. M. J. (2012). *Construction engineering of steel tub-girder bridge systems for skew effects* (Doctoral dissertation, Georgia Institute of Technology). Available from ProQuest.

Dassault Systèmes. (2020). Abaqus/CAE Version 6.20. Dassault Systèmes Simulia Corp., Providence, RI.

Development of Improved Equations for Live Load Moment ... - ResearchGate, https://www.researchgate.net/publication/373888413_Development_of_Improved_Equations_for_Live_Load_Moment_Distribution_in_Interior_Girders_of_Shallow_Steel_Tub_Girder_Bridges.

Ebeido, T., & Kennedy, J. B. (1996). Girder moments in continuous skew composite bridges. Journal of Bridge Engineering, 1(1), 37-45.

Ebeido, T., & Kennedy, J. B. (1996). Shear and reaction distributions in continuous skew composite bridges. Journal of Bridge Engineering, 1(4), 155-165.

Gibbs, C. L. (2017). Field performance assessment of press-brake-formed steel tub girder superstructures (Master's thesis, West Virginia University). Available from ProQuest.

Johnston, S. B., & Mattock, A. H. (1967). Lateral distribution of load in composite box girder bridges. Highway Research Record: Bridges and Structures, pp. 167, 25–33.

Kassimali, A. (2015). *Structural Analysis* (5th ed). Stamford, CT: Cengage Learning.

Kelly, L. T. (2014). Experimental evaluation of non-composite shallow press-brake-formed steel tub girders (Master's thesis, West Virginia University). Available from ProQuest.

Kozhokin, P. (2016). Evaluation of modular press-brake-formed tub girders with UHPC joints (Master's thesis, West Virginia University). Available from ProQuest.

The Mathworks, Inc. (2021). MATLAB. Natick, MA, The Mathworks, Inc.

Michaelson, G. K. (2010). Live load distribution factors for exterior girders in steel I-girder bridges (Master's thesis, West Virginia University). Available from ProQuest.

Michaelson, G. K. (2014). Development and feasibility assessment of shallow press-brake-formed steel tub girders for short-span bridge applications (Doctoral dissertation, West Virginia University). Available from ProQuest.

Micro-Measurements, I. (2010). StrainSmart [Data Collection]. Raleigh, North Carolina: Micro-Measurements, Inc.

Nakamura, S. (2002). Bending behavior of composite girders with cold-formed steel U section. ASCE Journal of Structural Engineering, 128(9), 1169–1176. doi: 10.1061-(ASCE)0733-9455(2002)128:9(1169)

Powell, G., & Simons, J. (1981). Improved iteration strategy for nonlinear structures. International Journal for Numerical Methods in Engineering, 17(10), 1455–1467.

Ramm, E. (1981). Strategies for tracing the nonlinear response near limit points. In E. Wunderlich, E. Stein, & K. J. Bathe (Eds), Nonlinear Finite Element Analysis in Structural Mechanics (pp. 63–89). Berlin: Springer-Verlag.

Righman, J. (2005). Rotation compatibility approach to moment redistribution for design and rating of steel I-girders (Doctoral dissertation, West Virginia University). Available from ProQuest.

Roberts, N. (2005). Evaluation of the ductility of composite steel I-girders in positive bending (Master's thesis, West Virginia University). Available from ProQuest.

Roh, A. D. (2020). Field evaluation of a modular press-brake-formed steel tub girder in an application that includes skew and superelevation (Master's thesis, West Virginia University). Available from ProQuest.

Sanchez, T. A. S. (2011). Influence of bracing systems on the behavior of curved and skewed steel I-girder bridges during construction (Doctoral dissertation, Georgia Institute of Technology). Available from ProQuest.

Short Span Steel Bridge Alliance. (2020). *Steel press-brake formed tub girder system selected for 2021 AASHTO Innovation Initiative focus technology*. SSSBA, Washington, DC.

Press Brake & Folded Plate - Short Span Steel Bridges, https://www.shortspansteelbridges.org/products/press-brake-folded-plate/.

Tarhini, K. M., & Frederick, G. R. (1992). Wheel load distribution in I-girder highway bridges. Journal of Structural Engineering, 118(5), 1285–1294.

Tennant, R. M. (2018). Fatigue performance of uncoated and galvanized composite press-brake-formed tub girders (Master's thesis, West Virginia University). Available from ProQuest.

Tennant, R. M. (2022). Expanding the Applicability of Press-Brake-Formed Tub Girders Through the Extension of the Maximum Span Length and the Evaluation of Pier Continuity. https://core.ac.uk/download/539495221.pdf

Underwood, N. M. H. (2019). Field performance and rating evaluation of a modular press-brake-formed steel tub girder with a steel sandwich plate deck (Master's thesis, West Virginia University). Available from ProQuest.

Valmont Structures. (2022). *Product details*. https://bridge.constructbridge.com/ProductDetails

White, D. (2022). Chapter 4: Strength behavior and design of steel. *Steel Bridge Design Handbook* (pp. 1–291). Chicago, IL: American Institute of Steel Construction.

White, D. W., & Kamath. A. (2020). Straight steel I-girder bridges with skew index approaching 0.3 (Report No. FDOT BE535). Tallahassee, Florida: Florida Department of Transportation.

White, D. W., Coletti, D., Chavel, B. W., Sanchez, A., Ozgur, G., Chong, J. M. J.,…Kowatch, G. T. (2012). *Guidelines for analysis methods and construction engineering of curved and skewed steel girder bridges* (NCHRP Report No. 725). Washington, DC: The National Academies Press. doi: 10.17226/22729

Yang, L. (2004). Evaluation of moment redistribution for hybrid HPS 70W bridge girders (Master's thesis, West Virginia University). Available from ProQuest.

Zokaie, T., Osterkamp, T. A., & Imbsen, R. A. (1991). Distribution of wheel loads on highway bridges. National Cooperative Highway Research Program Transportation Research Board National Research Council, 12-26/1, pp. 1–710.